

UNIVERSITY OF GENOA AND DAHER-SOCATA

DEVELOPMENT OF AN AUTOMATIC SHAPE OPTIMIZATION PLATFORM FOR A LAMINAR PROFILE



MASTER DEGREE DISSERTATION IN MECHANICAL, AERONAUTICAL ENGINEERING

Supervisors

Prof. Ing. Jan Pralits

Ing. Thomas Michon

Student

Marcello Benvenuto

20 Marzo 2014

... be the change you wish to see in the world ...

Development of an automatic shape optimization platform for a laminar profile.

Marcello Benvenuto

Department of Civil, Chemical and Environmental Engineering
University of Genoa
Italy.

Abstract

The work described herein concerns shape optimization, i.e. optimization allowing to find the best shape for defined Objective Functions. The shape analyzed in this report is an airfoil and the Objective Function is the drag in defined flight conditions. The viscous drag of a generic body immersed in a fluid is strictly linked to the features of the very small region called boundary layer, where the viscous forces have a large importance. As all the streams, the boundary layer can become turbulent because of irregular fluctuations, increasing the viscous drag. For this reason, the transition position was included in the Objective Function and the aim was to maximize its distance with respect to the leading edge.

In a collaboration between the Fluid dynamics group at the Department of Civil, Chemical and Environmental Engineering at the University of Genoa and the aeronautical company Daher Socata, it was developed a completely automatic optimization process of the root profile of the aircraft TBM 850.

A parameterization technique was used to represent the geometry of the airfoil using the software Catia V 5. This technique allows to consider the whole geometry with simple curves instead of the discrete points used for the fluid solver to define the profile. In this way we were able to change the profile with a very small number of parameters.

The Ansys software was used to create the fluid domain and to discretize

it (Meshing).

Further the software Fluent was used to perform CFD simulation with Reynolds Average Navier-Stokes Equations.

The laminar boundary layer was obtained by solving the boundary layer equations using an infinite swept wing assumption and its stability investigated with the linear stability theory, using the code NOLOT, based on the Parabolized Stability Equations (PSE). A semi-empirical method, e^N , was used to predict the transition location, according with the Mack's law. All these steps were assembled inside the software modeFRONTIER. This software is a powerful integration platform for multi-objective and multi-disciplinary optimization.

With a process of 30 minutes for each shape, starting with the root profile of the TBM 850 in cruise conditions, we have achieved a profile with 18% less drag than the TBM, of which 14% viscous drag and 4% pressure drag, maintaining nearly the same lift and momentum coefficient (difference of 0,1%).

The TBM's profile was also optimized in two different flight conditions at the same time (cruise conditions and take-off conditions) adding to the objective function to maximize also the lift coefficient at low speed. The results found showed values similar to the previous optimization for the transition. The lift coefficient at take-off condition did not increase much (1.66%). We also noticed that the shapes optimizing the lift coefficient were very different compared to the shapes maximizing the transition. The same optimization has been done also for the tip profile.

In the end, the root and tip optimal profile have been used to build a wing with the same parameters of the wing of the TBM 850. A CFD simulation at cruise condition has been done for this wing to evaluate its aerodynamic coefficients. The results have been compared with the wing of the TBM 850. Contrary to the results for a 2D analysis, the new wing had larger viscous drag (2.2% higher).

Acknowledgement

I would like to thank sincerely Prof. Ing. Jan Pralits for his support and for all the time he spent for me. I also want to thank Prof. Ing. Alessandro Bottaro and Daher Socata for giving me the opportunity to do this internship.

I am very grateful to Ing. Thomas Michon for his patience, support and for assisting me in CFD simulations.

I am grateful to Christophe Favre for supporting me in the first months of the internship.

I want also to thank Nicolas Bernardin for the funny video of Chloe and the training in Hapkido and Taekwondo.

My sincere thanks also to Guillaume Lehmann for picking up me in the rainy days and for Bouldering.

Un sentito "grazie" a Giovanni e Marco per avermi accompagnato a Tarbes. Quando mai ricapita di immergersi nelle piscine di Lourdes?

Grazie a Volpa e Alberto per la loro disponibilità a imprestarmi il loro materiale didattico una volta ritornato dalla Francia.

Grazie a Simo per il manuale di francese e per i piccoli festeggiamenti post esami.

Grazie a Roberta per la ricetta dei PlumCake; il cuoco forse non era tra i migliori.

Grazie a Dano, Tuz e Nico. E' anche ragionando con loro che ho deciso di passare alla specialistica di Meccanica.

Grazie a Don Mario, per avermi aiutato a contattare l'alloggio a Tarbes e per avermi fatto conoscere una delle migliori birrerie di Lourdes.

Grazie a Erica, compagna di esperienze, emozioni e sentimenti. Ai giorni passati insieme a Tarbes e al supporto negli ultimi mesi di studio.

Grazie a Olivia, Roberto e Flavia per essere stati di compagnia in videochiamata durante alcune serate francesi.

Grazie a Carlotta e Marco per aver spostato la data del matrimonio. Perdonatemi il meteo.

Grazie ai miei genitori per avermi sempre appoggiato nelle mie scelte. A loro è dedicato questo lavoro come coronamento di tutto il mio percorso di studi. Non è facile ammetterlo, ma sicuramente senza i "forza e coraggio" di mio padre e i "magari se studiassi invece di uscire" di mia madre, nulla sarebbe andato così come è stato vissuto.

Contents

Abstract	ii
Acknowledgement	iv
Chapter 1. Overview Daher Socata	1
Chapter 2. Introduction	3
Chapter 3. Physical Phenomenon	5
1. Boundary layer and friction drag	5
2. Laminar-Turbulent boundary layer	5
3. Transition	6
4. Pressure drag	7
5. Control of the boundary layer	8
Chapter 4. Numerical model	9
1. Parameterization	9
2. Flow Solver	11
3. Laminar Boundary Layer Solver	12
4. Transition Prediction Model	13
Chapter 5. Optimization Process	16
1. Optimization: general speaking	16
2. Shape optimization	17
3. Design Of Experiment	17
4. Optimization algorithms	18
5. Flow chart	19

Chapter 6. Parameterization: Catia V 5 profile	22
Chapter 7. Pre-processing: Domain, Meshing and CFD	27
1. Convergence and computational time	28
2. New domain	34
3. Viscous grid	38
4. Validation on TBM profile	40
Chapter 8. Platform Mode Frontier	43
1. Catia node	43
2. Design Modeler and Mesh nodes	45
3. Fluent node	45
4. bl3d and NOLOT nodes	46
Chapter 9. Viscous Optimization Cruise Conditions	51
1. Search DOE	51
2. Optimization Algorithms	54
3. Drag Evaluation	64
4. Conclusions	66
Chapter 10. Viscous Optimization High and Low speed	68
1. Take-off/Landing conditions	68
2. Changes in the modeFRONTIER platform	70
3. Root optimization	70
4. Tip optimization	74
Chapter 11. Validation 3D: Wing	78
1. Trailing Vortex	78
2. 3D effects	78
3. TBM wing	79
4. Catia V 5	80
5. Mesh	82
6. CFD simulation	82
7. Results	83

8. Discussion	83
Chapter 12. Conclusions and Future Works	87
1. Conclusions	87
2. Future Works	88
Appendices	90
Appendix A. Linear boundary layer 2 D	91
1. Prandtl's Boundary Layer Equations	91
2. Falkner-Skan	94
Appendix B. Linear boundary layer 2,5 D	103
1. Prandtl's Boundary Layer Equations	103
2. Falkner-Skan-Cooke	105
Appendix C. Thickness of the boundary layer	111
1. Displacement and Momentum thickness	111
2. Von Karman's integral equation	113
Appendix D. Linear stability theory of laminar boundary layers	116
1. Orr Sommerfeld and Squire equations	116
2. Parabolized Stability Equations (PSE)	120
Appendix E. Stability analysis of laminar boundary layer	123
1. Local stability analysis	123
2. Local stability analysis for 2,5 D	132
Bibliography	138

CHAPTER 1

Overview Daher Socata

Daher Socata is a French aeronautic company based in Tarbes. Its origins belong to the year 1911 with the birth of Morane-Saulnier. In 1966 Morane-Saulnier was purchased by Sud Aviation and was renamed to SOCATA. In 2000, Socata was bought by EADS, who sold 70% of the company to Daher in 2008.

Since Socata was born, it has created a range of products and services which combine its expertise in aircraft and aerostructures manufacturing. Today the business turbo prop TBM 850 is the only aircraft that the company makes (Figure 1.1).



FIGURE 1.1. TBM 850

With cruise speed up to 320 KTAS at flight level 260, the TBM 850 offers travel time typical of light jets but with the efficiency of a single-engine turbo prop.

CHAPTER 2

Introduction

Daher Socata, as all companies in the world of business jets, tries every day to improve the performance of its aircraft to keep up the technological progress.

Most of the studies to improve the efficiency of the aircraft concern fluid mechanics and they involve the study of the small viscous region close to the surface called boundary layer. This region is the principal cause of viscous drag and its magnitude depends a lot on the shape of the body. For this reason, the design of the shape in order to reduce dissipation and friction drag is a priority in all the aircraft companies.

To reduce the design cost and time, it has become necessary to use Shape Optimization, searching the better shape by minimizing a defined cost function. Shape optimization is just one of the several classes of problems. The introduction of optimization tools has completely changed the approach to solve the problems of many companies, representing a tool as powerful as versatile for different engineering practices. The optimization approach has allowed to save time during the design process by automatically running multiple repetitive simulations and, even more important, to reduce their cost by executing concurrent evaluations. Therefore, the improvement and the optimization of the industrial design processes are increasingly important for many companies.

Several optimization softwares have been developed by various companies; one of them is the optimization and design environment modeFRONTIER

that was developed by ESTECO SpA in 1999, to couple CAD tools and CFD software. Daher Socata bought the license of modeFRONTIER in December 2012 to build various optimization platforms for problems concerning fluid mechanics.

The work made during this internship uses modeFRONTIER to perform a shape optimization in 2D. The objective of the optimization is to find the best wing root airfoil of the TBM 850 for one flight condition, to minimize its drag coefficient and have a value of the lift coefficient as close as possible to a defined value to avoid changes in the global wing loading. The choice to analyze the flow around a part of the wing is because of the propeller located at the front. Although the presence of the frontal propeller allows to produce thrust more economically than a jet engine, it involves also large masses of air becoming turbulent downstream the blades. This effect generates a big turbulent stream shrouding all the fuselage. A turbulent flow is chaotic and unpredictable and this doesn't allow to study it in accurate way. Another surface that we could have considered is the surface of the tail, but the effects on Lift and Drag are small compared to the wing.

CHAPTER 3

Physical Phenomenon

1. Boundary layer and friction drag

When a generic body immersed in a fluid is accelerated, a very small region forms close to the surface of the body. In fact, by the relative motion between the body and the fluid, some particles of the flow very close to it, adhere to the surface because of the viscosity of the flow and generate a thin layer that is called boundary layer.¹ The boundary layer is the region where the viscous forces have a great importance and is therefore responsible of the friction drag.

2. Laminar-Turbulent boundary layer

We can make a distinction between two different types of boundary layers: laminar boundary layer and turbulent boundary layer. Their nature is linked to the viscosity, the velocity and the shape of the wing. The principal difference between them is the thickness: it is larger for the turbulent case, see Figure 3.1.

The irregular fluctuations (mixing) that characterize a turbulent stream are responsible for the large resistance compared to a laminar stream[1]. For this reason, if we want a low friction drag it will be favorable to have a laminar boundary layer extended as much as possible along the streamwise direction.

¹Considering an aircraft, the surface where the boundary layer is most important is the wing

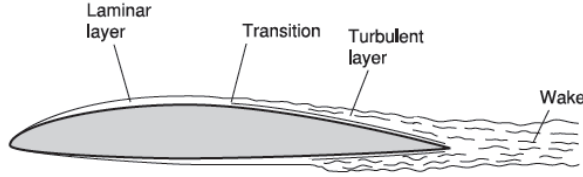


FIGURE 3.1. Transition between laminar and turbulent boundary layer on an airfoil. To note the different thickness that lead to different drag.

3. Transition

The region in which we have a change of the laminar boundary layer into turbulent boundary layer is called transition. The laminar boundary layer, like all the flows, can become unstable if affected by disturbances of the free stream or surface roughness and generate turbulent flow on the wing surface. Free-stream turbulence or acoustic disturbances represent such external disturbances. These disturbances can enter the boundary layer and generate unsteady fluctuations. These fluctuations can decrease and vanish or increase and lead to transition. Therefore, the theory that describes the stability of the laminar boundary layer², considers small wave disturbances and analyzes their growth in time and space.[2]

Several instability mechanisms have been identified, depending on the geometry that we consider. In fact, in the case of a 2D geometry, the only instabilities that can lead to transition are called Tollmien-Schlichting waves (TS). Their direction of propagation is aligned with the streamline direction.(Figure 3.2)

In 3D flows, the dominant instabilities are called CrossFlow disturbances. The name comes from the fact that they appear due to the inflection

²Linear Stability Theory, Appendix D

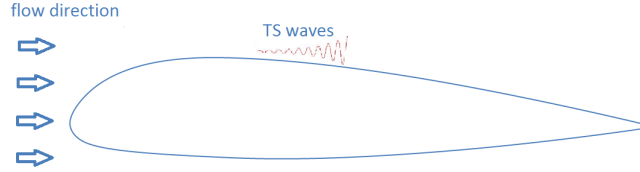


FIGURE 3.2. TS wave in a 2D geometry

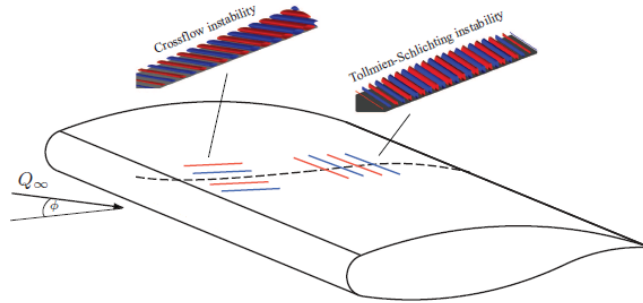


FIGURE 3.3. Cross flow and TS instabilities in a three-dimensional wing boundary layer. (Red: positive velocities, Blue: negative velocities)

point in the cross-flow component of the laminar flow. In these flows the TS instabilities also exist and they are sometimes called streamwise instabilities. (Figure 3.3)[3]

4. Pressure drag

In the global drag of a wing, there is another important component to add to the friction drag, called pressure drag, and it is mainly linked to the shape. The pressure drag is evaluated as a closed surface integral projected in the desired direction. Any pressure difference along the surface, can therefore add a component to the pressure drag. This is of course linked to the pressure gradient on the wing. Both a favorable and an adverse pressure gradient can influence the drag. Moreover before changing from

laminar to turbulent, the boundary layer can separate from the surface because of a great adverse pressure gradient. This phenomenon increases a lot the pressure drag.

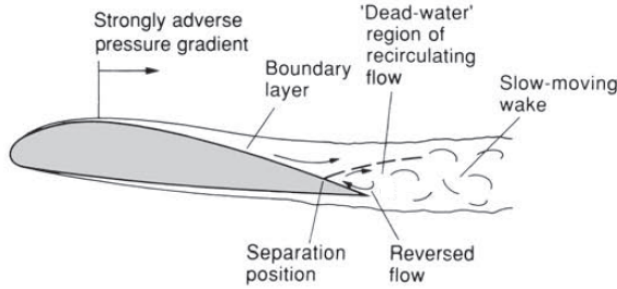


FIGURE 3.4. Separation on trailing edge due to an adverse pressure gradient. Note that the separation creates a region of reversed flow that increases the drag.

5. Control of the boundary layer

On an aircraft there are two different ways to reduce the friction drag on a wing[5]. The first deals with designing an airfoil to have a laminar flow on the largest region as possible on the wing (NLF - Natural Laminar Flow). The second uses different technologies to maintain the flow laminar on the wing, for example suction, blowing, wall cooling (LFC - Laminar Flow Control)[6].

The work made in this thesis is focused on the first method. It is important to keep in mind that all these phenomena involving fluid mechanics always require numerical simulations.

CHAPTER 4

Numerical model

The optimization created during the internship is based on a numerical study to locate the transition position of the boundary layer on a 2D geometry. This type of problem requires tools capable of solving numerically the Navier-Stokes's equations that describe the motion of fluid flow. Coupling these tools with a method to parameterize the geometry, it has been possible to create the platform for a shape design optimization. The process has been broken into 4 key parts: a parameterization of the airfoil, the flow solver, the solver of the boundary-layer equations and the solver of the stability equations of the boundary layer.

1. Parameterization

A generic parameterization technique allows to describe a shape with a small set of inputs. In an optimization process it is very important and desirable to limit the number of the geometric design variables. Different strategies have been implemented to do this. One of them considers a geometric shape function where all the airfoil is described by analytic well behaved and simple mathematical functions: CST, see Figure 4.1. CST build the airfoil by summing the individual contribution of its basis function constructed by Bernstein polynomials[7].

This method allows to control the shape with general characteristics such as the maximum thickness. Another technique requires to use a CAD software, to create the profile with a few number of polynomial approximations curves (splines). The spline is a smooth polynomial function piece-wise

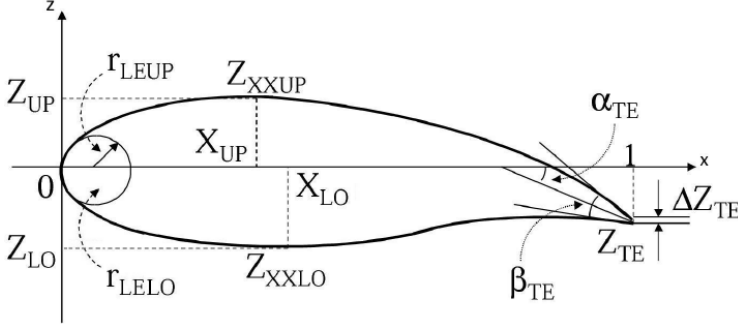


FIGURE 4.1. CST parameterization.

defined and possesses an high degree of smoothness at the place where the polynomial pieces connect (which are known as Nodes). A link between these points and the splines is imposed to control the shape of the body (Figure 4.2.)



FIGURE 4.2. Effects of different tensions of a spline near to two fixed control points.

This second method allows to have a better parameterization if the shape has to respect constraints regarding the thickness. Therefore, as explained in the Chapter 8, we preferred this method instead of a CST parameterization.

2. Flow Solver

A numerical simulation is often required to solve and analyze problems involved in fluid mechanics. In fact the Navier-Stokes's equations can only be solved analytically in very simple cases.

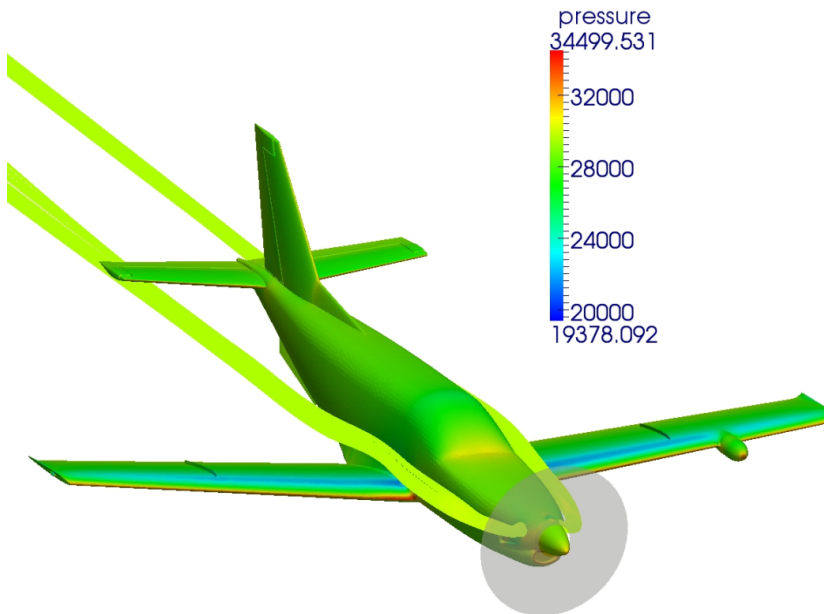


FIGURE 4.3. Pressure distribution on the TBM 850 and streamlines coming out from the exhaust stubs. Altitude 26.000 feet; Velocity 320 knots; Mach Number 0.51. Computational fluid dynamics.

The branch that uses numerical methods to solve the N-S equations is called CFD (Computational Fluid Dynamics) and many different industrial softwares exist to solve them. We can see an example of results by CFD on an aircraft in the Figure 4.3. In this figure the pressure distribution on the aircraft is investigated. The basic methodology to simulate

the interaction of a general fluid with surfaces requires to define the geometry of the domain, to discretize the volume occupied by the fluid, to choose the physical model, to set the boundary conditions and perform the simulation. In this thesis, the platform Ansys was used to discretize the domain (Mesh) and to solve the Navier-Stokes's equations (Fluent). One of the most critical steps when studying a turbulent flow, is the choice of the most suitable physical model. A very expensive strategy, in terms of time, to solve the Navier-Stokes's equations, is the DNS (Direct Numerical Simulation). This technique considers all the temporal and spatial scales belonging to the turbulent structure. To solve a problem with this technique is not simple because of the chaotic aspect of the turbulence and because of all the big scale influence on the smallest ones, following the theory of turbulent energy cascade[8]. A faster technique, that considers only the mean motion of the turbulent scale is called RANS (Reynolds Average Navier-Stokes)[9]. This strategy can be used if coupled with turbulent models to consider the effects of the turbulent structures. A software like Fluent provides several physical models capable of solving the Navier-Stokes's equations. From the solution we can extract all the characteristics of the flow around a general a body, like aerodynamics coefficients, velocity and pressure distribution.

3. Laminar Boundary Layer Solver

In this thesis the software bl3D is used to obtain the viscous laminar boundary layer. Starting from a pressure or velocity distributions on the profile, the code allows to calculate the most principal parameters of the boundary layer such as thickness, shape factor and velocity distribution. This software allows to investigate the laminar boundary layer for incompressible/compressible and two/quasi-three dimensional flow.(Figure 4.4)¹

¹More details are given in Appendices A, B and C

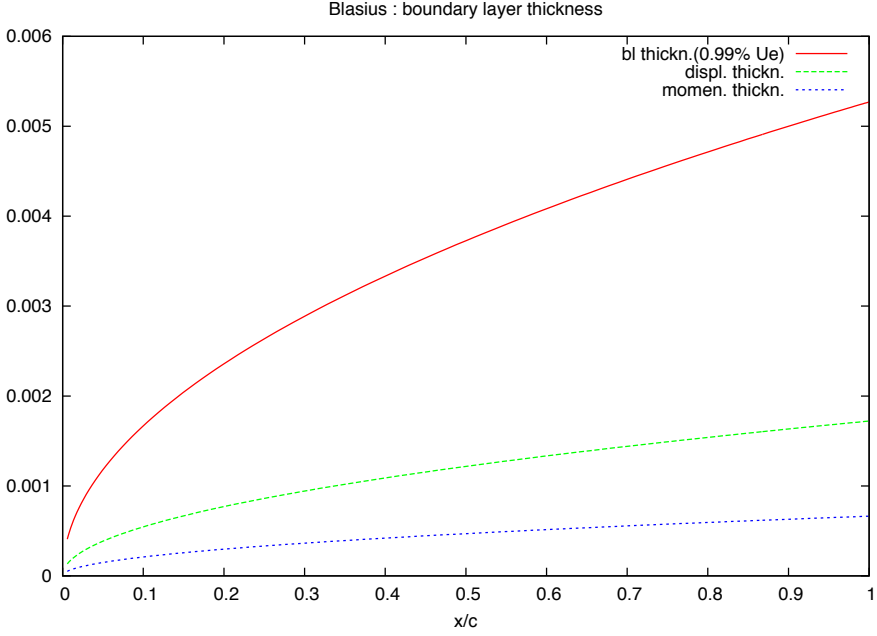


FIGURE 4.4. Distribution of three boundary layer thicknesses (δ_{99} , displacement thickness and momentum thickness) on a flat plate as a function of the streamwise coordinate. Two-dimensional, steady and incompressible flow.

4. Transition Prediction Model

Theoretically, the transition is investigated by studying the equations of mass, momentum and energy conservation. The solutions of these equations can not generally be found analytically[10]. Therefore, codes that simplifies the equations with assumptions about the behavior of disturbances are required. In this thesis, the stability code named NOLOT is used, based on nonlocal, nonparallel stability equations of parabolic type(PSE). The NOLOT code was developed in 1993 at the Department of Mechanics of the Royal Institute of Technology (Stockholm) as a collaboration between different research institutes. The numerical model

is based on the linear stability analysis, considering that in general the laminar-turbulent transition on a body is often due to the amplification of small disturbances which amplify along the wing profile. Initially their evolution is well described by linear theory.² This theory concerns the evolution of perturbations with infinitesimal amplitude superimposed on a laminar flow. The flow is decomposed in mean flow and non-steady disturbance:

$$u = U + u^I$$

The goal is to determinate if the disturbances amplify or not in space (spatial stability). A single oscillation of the disturbance is represented by a stream function Ψ :

$$\Psi(x, y, z, t) = \Phi(y)e^{i(\alpha x + \beta z - \omega t)}$$

where α and β are the wavelength number of the disturbance respectively on x - and z -directions. ω is the frequency of the oscillation. In a spatial stability we consider α as a complex number ($\alpha = \alpha_r + i\alpha_i$) and the stability will hold for the imaginary part of the wave-number, being positive. $-\alpha_i$ is called growth rate of the disturbance and its integral along the chord is called N factor (Figure 4.5):

$$N = \int_{x_0}^x (-\alpha_i) dx$$

The method that uses the N factor to study the stability is the semi-empirical e^N method. Coupling the PSE, the e^N method and the Mack's

²Linear stability theory is presented in Appendix D

Law, the transition is supposed to occur at an empirical value of the N factor defined as:

$$N = -8.43 - 2.4 \ln(Tu)$$

where Tu is the turbulent intensity of the main flow:

$0.0007 < Tu < 0.0298$. Generally, in a calm atmosphere the turbulent intensity is quite 0.1%. With this value the transition occurs at a value of N near 8.

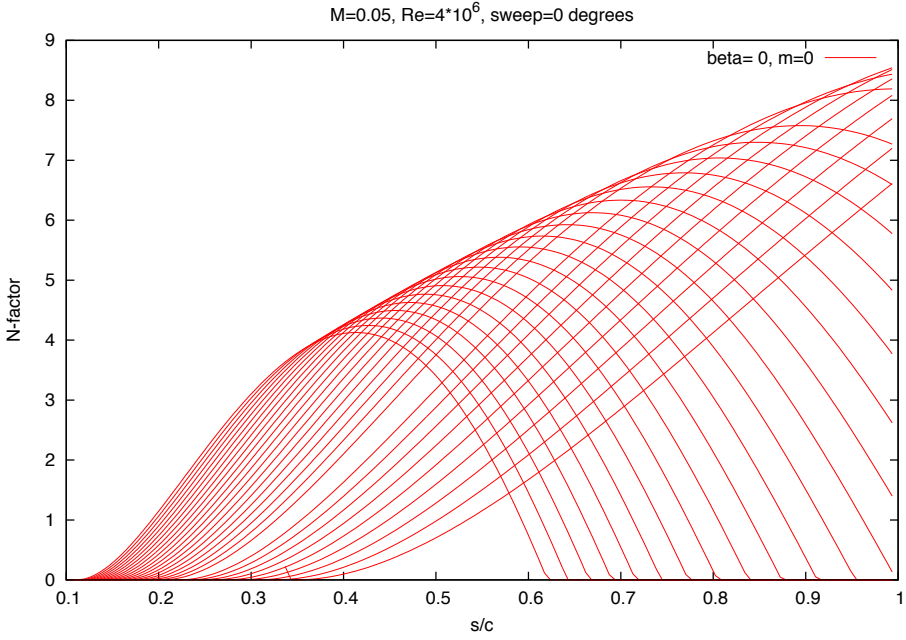


FIGURE 4.5. N factor on a flat-plate for $R_e = 4 \cdot 10^6$; $M = 0.05$; $m = 0$; $\beta = 0$. The figure shows the development of N factor for different frequencies of the disturbances. The transition is supposed to occur at the position corresponding to a value of 8 of the N factor.

CHAPTER 5

Optimization Process

This chapter presents an introduction on general optimization problems with an attention to the Shape optimization. The principal algorithms for DOE (Design of Experiment) and for the optimization will be presented. After that, the process created with the platform modeFRONTIER will be explained focusing on each step created.

1. Optimization: general speaking

In general we can consider an optimization composed by three elements:

- (1) **Optimization parameters:** model parameters to be optimized.
- (2) **An objective function:** mathematical expression describing the quantity one desires to maximize or minimize.
- (3) **Constraints of the system:** conditions defining a range for an optimization parameter.

Hence the optimization can be viewed as a search for the parameters that result in a maximum or a minimum of the objective function, respecting the constraints. If we have only one objective function (single-objective-function), the final results will represent the optimal of the problem. Otherwise, if we have more than one objective function (multi-objective-functions), we will have a set of solutions that represents a compromise between all objective functions. All the results will be on what is called the Pareto Front and it will be necessary to make a choice to consider only one solution.

2. Shape optimization

Shape optimization is a particular problem of optimization. In an abstract way, one can think the problem expressed like that:

$$(1) \quad F(W) = \text{opt} f(w)$$

with $w \in \Omega$; W is the optimal shape among all shapes w inside an admissible domain Ω . The opt can represent a min or a max of a quantity such as the drag (to minimize the drag if we want less friction) or a transition position (to maximize the position if we want a laminar boundary layer extending further downstream). Therefore, the goal of this type of optimization is to find the optimal shape for which the objective function is minimized or maximized and the constraints are satisfied. For these particular problems, the shape is represented with a parameterization technique. Therefore the control parameters of the parameterization will be the control parameters of the optimization.

3. Design Of Experiment

The methodology to find the optimal shape can be generally divided in two parts: a first part where several shapes are found, exploring all the domain of the design parameters (DOE, Design of experiment)[12], and the second one in which these shapes are used as starting points to find the optimal final shape. The final shape is the best answer for the objective functions and for the constraints. The DOE is essential to explore the domain and to define the behavior of the objective functions. The goal is to obtain as much information as possible starting with a limited number of experiment. Several algorithms can be used for the DOE. The principal difference between the algorithms is the way in which the domain is explored which can be random or uniform.

4. Optimization algorithms

After exploring the domain, optimization algorithms are used to find the best solution. This second part is in general more expensive than the DOE because of the big number of existing solutions. It is important to remember that the quality of the search depends on the robustness and precision of the algorithm. These two properties are not in general inside the same algorithm and hence it is better matching global research (robustness) with a local one (precision). Depending on the study (goal, single or multi objective functions, number of control parameters, presence or not of constraints) there are different algorithms that can be used and most of them are based on the fundamental principles of the nature like natural selection, population development, genetic mutation or even on the game theory[13]:

- **Multi objective game theory:** This technique transforms the optimization problem into game strategic problem and uses adaptable game evolution process to obtain the optimized strategy.
- **Genetic Algorithm:** It is a Heuristic algorithm inspired by natural evolution theorized by Charles Darwin. The evolution usually starts from a population of randomly generated individuals and at each iteration (usually called Generation) the objective function is calculated. After some generation, only the good solutions are kept, to generate a new population and converge to a possible best solution.
- **Gradient Based:** This algorithm is based on a direction of the descent

$$(2) \quad dk = -\nabla f(X_k)$$

dk is the opposite direction of the gradient of function f in X_k . Starting from a point in the space, its gradient is calculated to know where the function goes to its minimum value. Following this way, a new gradient of a new point is calculated until arriving to the local minimum. This refinement method works well with

only one local minimum, and for this reason it is often used after other algorithms like the genetic one.

5. Flow chart

After presenting the main characteristics of an optimization problem, we can present an overview of the steps to be performed for our shape optimization, focusing the attention on the objective functions.

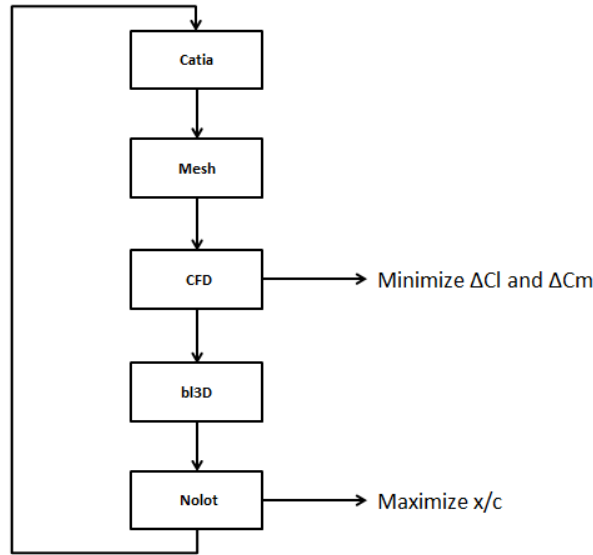


FIGURE 5.1. On the left side one can see the steps of the automatic optimization process. On the right side there are the objective functions considered in this problem: minimize the value of Lift and Momentum coefficients relatives to the value of the original profile; maximize the transition position on the upper side of the airfoil.

The tools presented in Chapter 4 have been used to create all the process. The CAD software Catia V 5 has been used to parameterize the airfoil.

After, a discretization of the domain around the airfoil has been made to study the flow with the flow solver Fluent. bl3D and NOLOT have been used to study the transition phenomenon.

To close the cycle of optimization we have to set the objective functions. For this type of problem we have chosen four different objective functions. Thanks to the Multi Objective Function of the optimization platform modeFRONTIER, we can consider more than one objective function at the same time. As we can see from the flow chart (Figure 5.1), we have chosen to maximize the position of the transition, according with the phenomenon explained in Chapter 3 and to minimize the value of C_l and C_m relative to the value of the original profile. In fact, if we change the shape to reduce the drag coefficient, we also change lift and momentum coefficients. These changes can lead to a different repartition of the global lift on the wings, generating stability and stalling problems, see Figure 5.2.

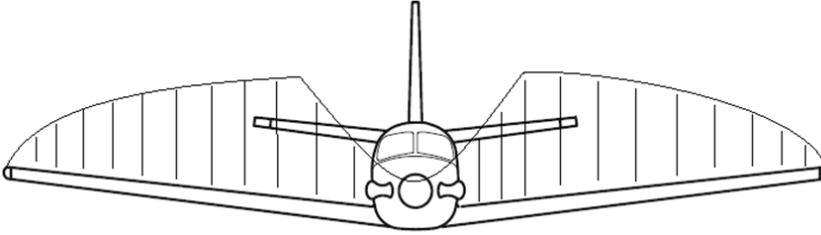


FIGURE 5.2. Global lift repartition on the wings of the TBM 850.

Therefore, an airfoil for which the value of C_l and C_m are close to the value of the root airfoil of the TBM 850, guarantees that we do not have changes in the global wing loading. Besides, we have considered C_l and C_m as Objective functions instead of constraints, to not limit too much the shape variations, in favor of the transition delay.

Each step has required a challenging work to be performed for all the automatic optimization process. Therefore, before looking at the results and the conclusion of the optimization, we are going to present how each step has been created and how the process has been built inside modeFRONTIER.

CHAPTER 6

Parameterization: Catia V 5 profile

The starting point for our optimization is the root profile of the TBM 850.

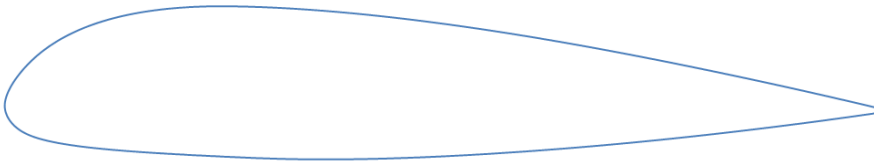


FIGURE 6.1. Root profile of the TBM 850.

As introduced in the Chapter 4, the technique used to parameterize the airfoil is made with curve splines. This parameterization allows us to change the shape of the profile with a small number of control points. The choice of this parameterization has been done due to the presence of the constraints explained below.

- (1) the chord is fixed at 1 meter
- (2) the thickness at the 25% and 75% of the chord is constant

All the airfoil has been created with the 9 points, see on Figure 6.2. A link between the points and the edges has been created to build the shape. At each point the edges are controlled with a value of tension. How different values of tension control the shape of the splines, can be seen in Figure 6.3 :



FIGURE 6.2. The profile of the TBM created with Catia software.

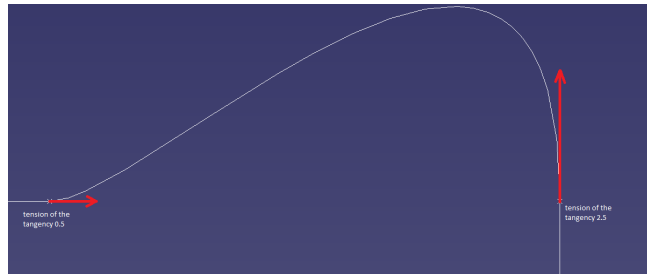


FIGURE 6.3. Example of different values of tension of the spline near two fixed control points.

To respect the constraints and to allow the shape to change, only some points have been taken as control points. The lines that follow explain the procedure used.

To maintain the thickness at 25% and 75% of the chord we have fixed the position of the points 3,4,7,8 as can be seen in Figure 6.4. This assumption is realistic if we consider that the structure in this region is very important and that we have also a volume to respect for a minimal fuel.

The area where the shape has a strong influence on the flow is the leading edge, where we have the greatest variations of the shape. We have decided to control the curvature of the radius of a circle inscribed in the airfoil. The minimal value of the radius is thought to respect requirements for the manufactory.

We have imposed both the upper and the back side of the leading ledge to be tangent to the circle.

The thickness of the trailing edge is controlled with a single variable. No control of the shape near the trailing edge was imposed since it was considered of less importance in relation to the boundary layer transition. This part will remain equal to the shape of original profile.

To allow the shape to change near the points 2,3,8,9 we control the tension of the splines.

Moreover, points 2 and 9 of Figure 6.4 are free to move inside a square, considering reasonable shape.

All the control parameters above explained are plotted in the Figure 6.4:

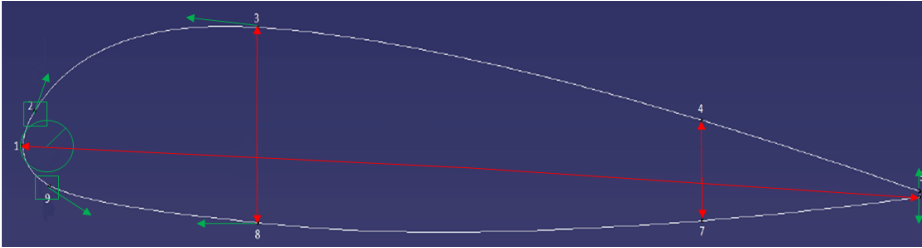


FIGURE 6.4. Control parameters for the optimization process.

Reproducing the edges of the shape of the TBM was time consuming and we noticed a great sensibility of the C_p distribution with respect to the shape of the leading edge. To better understand it, we have plotted two different shapes, both of them very close to the TBM, with the respective distribution of the pressure coefficient

As can be seen from the C_p distribution of Figure 6.6, we discovered a small blemish on the pressure side of the model (green line). For this reason, the red profile was used as reference for the optimization process.

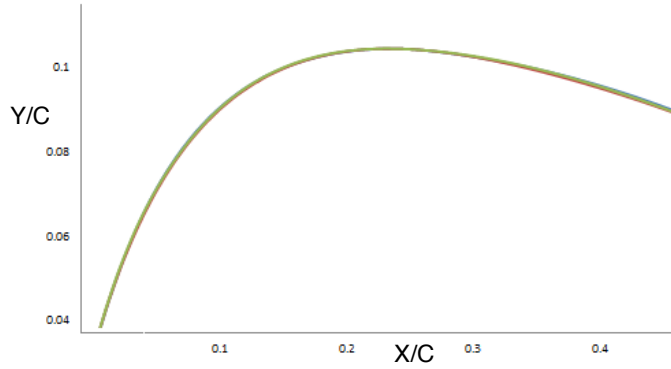


FIGURE 6.5. Zoom on the leading edge between 10% and 40% of the chord. Comparison between the shape of the TBM (green) and other 2 profiles very closed to it (red and blue).

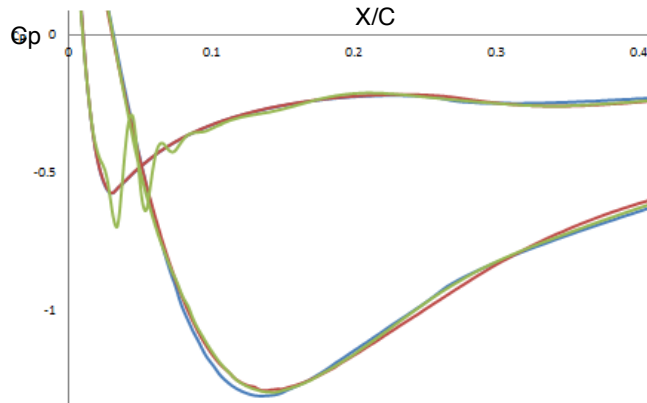


FIGURE 6.6. Comparison between the distribution of the pressure coefficient of the TBM (green) and two profiles very close to it (red and blue). The pressure coefficient is strongly affected from the shape of the leading edge.

After creating the parameterization of the original profile for the optimization, we checked that the control points didn't introduce oscillations on the profile looking at the derivate dy/dx as a function of x .

CHAPTER 7

Pre-processing: Domain, Meshing and CFD

The objective of this section is to describe how to find the domain for the numerical solutions and the parameters to discretize it (parameters of the mesh). The work is subdivided in two part: a first part where we define the domain and the mesh for a laminar profile, and a second one where a validation of the stability code with the mesh used on the TBM profile is done. The choice to use a laminar profile, in particular the OASL012 (Figure 7.1), is justified considering that the objective of the optimization is to re-laminarize the TBM profile as much as possible. For this reason, we can assume that the mesh parameters for the OASL012 should be suitable for the profiles found during the process. This profile has been used for several study by ONERA (Office national d'études et de recherches aérospatiales) to study its aerodynamic characteristics.

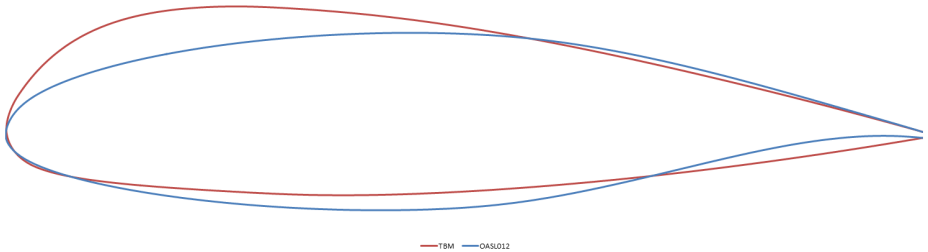


FIGURE 7.1. Geometry of the laminar profile OASL012 compared with the turbulent profile of the TBM 850. Chord fixed at 1 m.

1. Convergence and computational time

Ansys software Meshing is used to create the domain. The geometry can be imported in two different ways:

- from a file containing a list of points that define the shape
- from a CAD file

Following the first way, we have imported the geometry in Design Modeler, a software of Ansys Workbench platform, to create a domain around the airfoil. The text file divided the profile in two parts: airfoil and trailing edge. The procedure to create the domain is quite simple and it consists in defining a geometry in the background from which to extract the geometry of the airfoil. The structure of this domain was chosen as the kind called C, see Figure 7.2:



FIGURE 7.2. Domain C around the airfoil. The length of the rectangular is 150 meters, the high 90 meters and the chord of the airfoil is 1 meter.

This domain is large enough to prevent interactions between the downstream and the boundary conditions.

1.1. Mesh. We have considered 5 different grids, from a coarse and fine mesh with 72000 and 220000 cells respectively, to find the best solution (Table 1).

TABLE 1. Comparison between the mesh

Mesh	0	1	2	3	4
NonUni	y	y	y	y	y
Cells	220000	180000	140000	110000	72000
Growth rate	1.022	1.022	1.04	1.08	1.12
Min. size	0.0001	0.0009	0.001	0.002	0.003
Max. size	0.001	0.002	0.003	0.004	0.005
Max skewness	0.7567	0.8798	0.8316	0.8676	0.7299
Times	18'	12'	10'	5'	4'

The best solution must be considered as the most reasonable in terms of time and quality. In particular, we have determined the mesh for which we can consider invariant the values of C_l , C_d , C_m and the position of the stagnation point. In fact, this trade off gives reasonable computational time, while an invariant value and position of the items above set, are an assurance of good quality. We have used a non uniform distribution for the meshes. (Figure 7.3)

The maximum value of the skewness for each mesh is under 0.9 like Ansys's guide suggests¹. [15]

It was decided to begin with the most refined mesh (220000 cells) considering it as a reference for a good quality and good physical results. For this first approach the mesh created is without inflation for an inviscid study.

1.2. CFD. After creating the grids we ran the CFD simulation. The flight conditions used are given in table 2.

TABLE 2. Cruise conditions

Mach Number	Reynolds Number	Altitude (feet)	Velocity (knots)
0.51	8901189	26.000	320

¹The skewness indicates the quality of the mesh

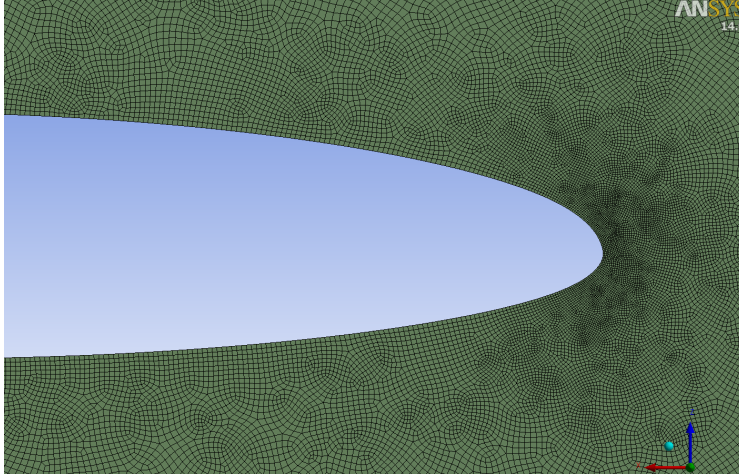


FIGURE 7.3. A representation of the leading edge for a non uniform mesh definition.

The flight conditions are the same as the TBM 850 in cruise condition. To run the CFD simulation we used the software Fluent inside the platform of Ansys. A journal file was used to write line by line the commands for fluent. This procedure allows to run Fluent in an automatic way. Hence in this journal file we have set the parameters explained in the following lines.

First of all we set the flight conditions. For inviscid case, the algorithm for the continuity and momentum equations is the pressure based coupled solver. The boundary conditions are about the velocity that is the velocity of the external flow to the inlet and to the outlet section and zero at the other two parts of the domain. We have used pressure-velocity coupling as algorithm for the solver. The airfoil has been analyzed for five different angles of attack from 0 to 4 degree with a spatial discretization from 1st to 3rd order.

1.3. Results. After running the calculation with fluent we checked the residual of the continuity and momentum equations and the convergence of the force on the airfoil. As can be see from Figure 7.4, these parameters did not converge.

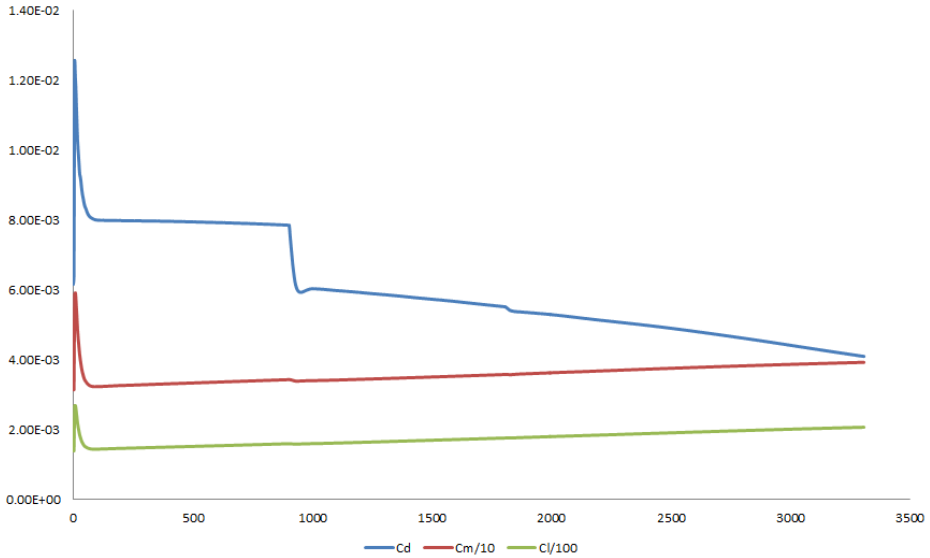


FIGURE 7.4. Results of convergence of the aerodynamic coefficients for the laminar airfoil OASL012. Cruise condition with 1 degree of angle of attack.

Looking at the C_p distribution (Figure 7.5), small oscillations were found on the upper surface, close to the minimum value. A good quality of the C_p distribution on the airfoil is a key point for a good solution of the stability equation of the boundary layer. In fact, a non-smooth C_p distribution can produce big oscillations on the disturbances inside the b.l. and to lead to non-physical instability.

We further noticed that sometimes fluent had problems to solve the equations close to the airfoil because there were numerical problems in some areas of the domain.

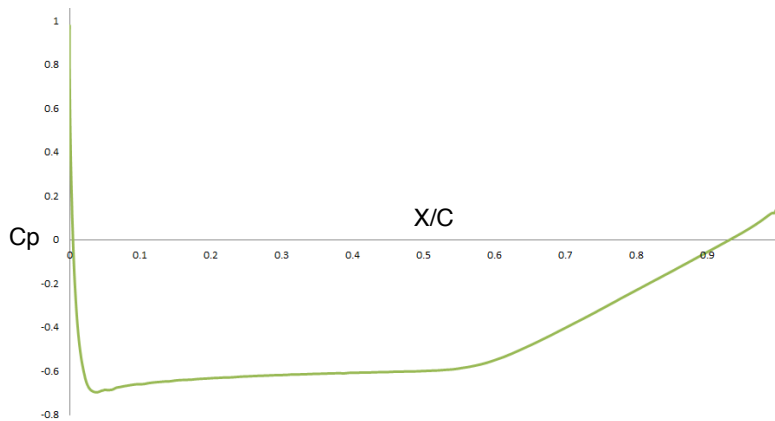


FIGURE 7.5. Distribution of pressure coefficient on the upper side of the laminar profile OASL012. We can see small oscillations just after the beginning of the adverse pressure gradient. 4 degree of angle of attack.

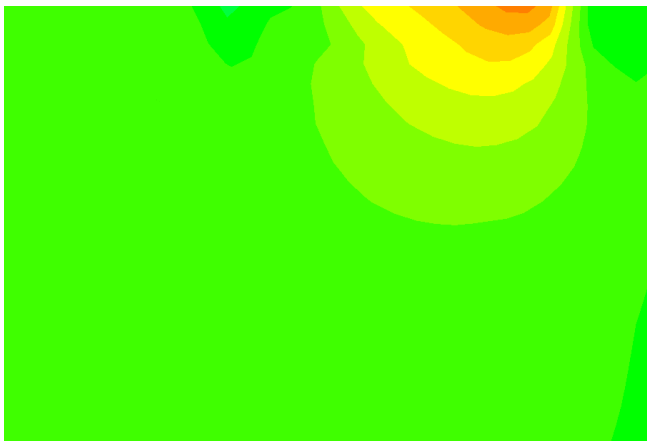


FIGURE 7.6. Numerical problem near to the corner of the domain in the top-right side. Inviscid and incompressible flow. The boundary conditions are the velocity of the flow to sections inlet and outlet.

1.4. Discussion. The problems of convergence were probably due to the algorithm used for the numerical solutions. On the other hand, the problems of the oscillations of C_p could be generated by two causes:

- (1) The geometries from the original points and from the mesh could have small oscillations.
- (2) For an inviscid analysis, fluent introduces a numerical dissipation instead of the viscous terms[14], and this dissipation could influence the C_p distribution by generating oscillations.

Therefore, we decided to monitor the pressure gradient on the airfoil by Fluent. In fact, the coefficients of lift and drag don't allow to see if we have oscillations or not because they are integral quantities.

On the other hand, for the first point it was decided to check the derivate $\frac{dy}{dx}$ for the geometry of each grid.

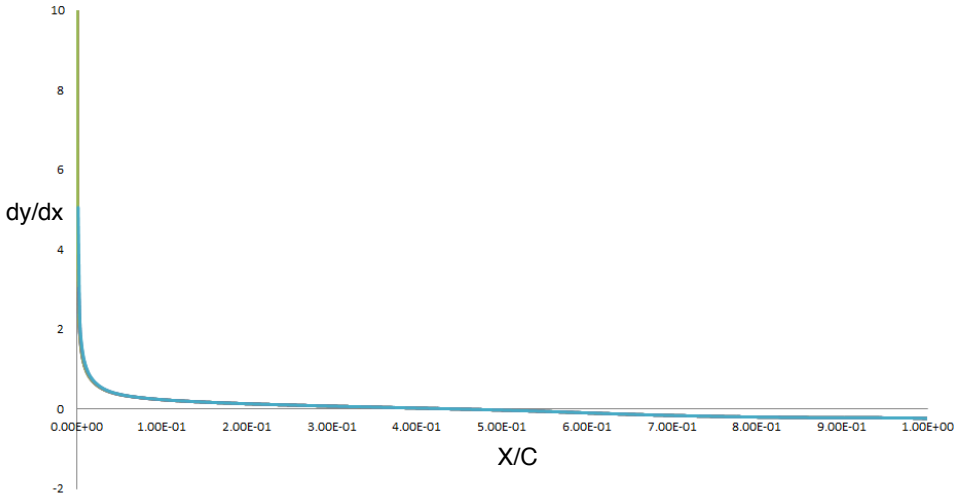


FIGURE 7.7. A representation of the derivate dy/dx as a function of the dimensionless coordinate x/c , for all the grid. y is the normal coordinate to x/c . As can be seen, all the meshes gave the same profile without oscillations.

As one can see in the Figure 7.7, the original profile and all meshes give a good geometry without oscillation, thus we can say that the problem of a non-smooth C_p distribution is due to of the CFD analysis.

Besides, for the numerical problems near to the wall of the domain, it was decided to change the domain.

2. New domain

The new domain is represented by a circle (Figure 7.8). The radius of the circle is set at 90 meters.

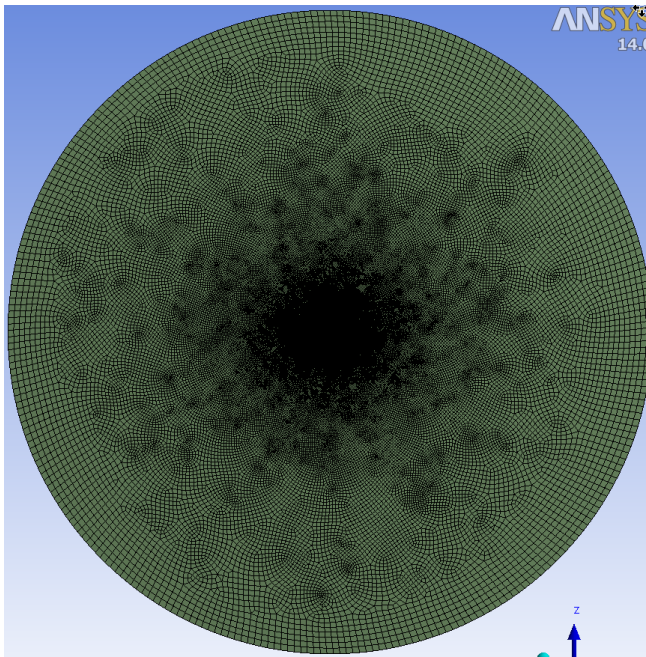


FIGURE 7.8. New domain for the airfoil. The chord of the airfoil is 1 m. and the radius of the domain is 90 m. Mesh without inflation for an inviscid calculation.

2.1. CFD. With the same journal file we have computed the energy and momentum equations.

Looking at the C_p distribution we noticed that the maximum value in the stagnation point, expected to be very closed to one for an inviscid calculation, was about 0.009 (Figure 7.9).

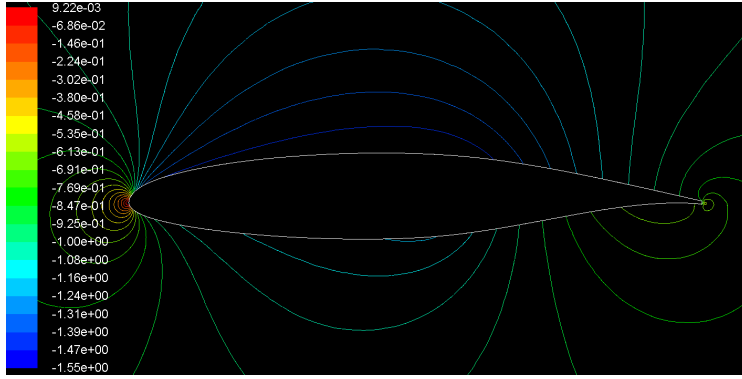


FIGURE 7.9. Maximum value of the pressure coefficient at the stagnation point. Inviscid and incompressible calculation. 2 degree for the angle of attack.

For this reason we decided to change the boundary condition considering the pressure at the far field and not the velocity inlet.

Considering the pressure far field, we also changed the state of the density and focused our study on a compressible flow.

2.2. Results. This set up gave a good convergence of the parameters monitored (Figure 7.10) and a value of maximum C_p a slightly larger than 1 for the meshes in the Table 1(Figure 7.11).

The values of the C_d coefficients of the meshes in Table 1 are plotted as a function of the number of cells on the surface of the airfoils.(Figures: 7.12)

In Figure 7.13 we can see a comparison between the position of the stagnation point for the 5 meshes.

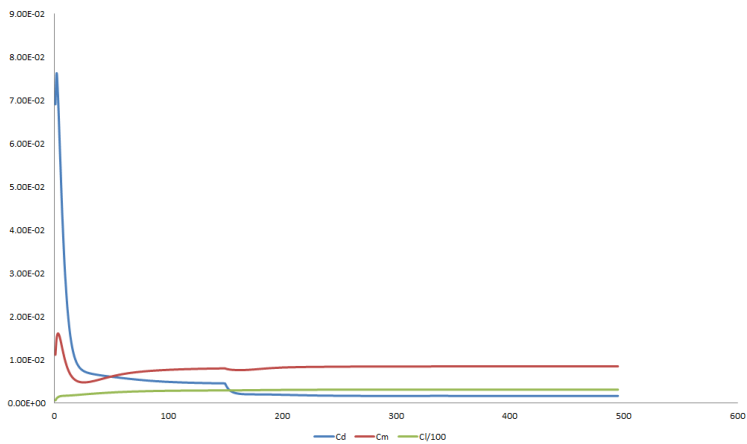


FIGURE 7.10. Convergence of the aerodynamic coefficients. OASL012. Cruise conditions with 1 degree of angle of attack.

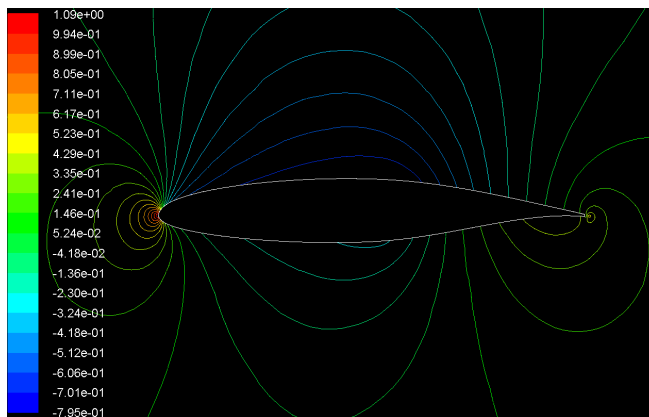


FIGURE 7.11. Maximum value of the pressure coefficient at the stagnation point. The boundary condition is the value of the pressure on the far field. Inviscid and compressible calculation. 2 degree for the angle of attack.

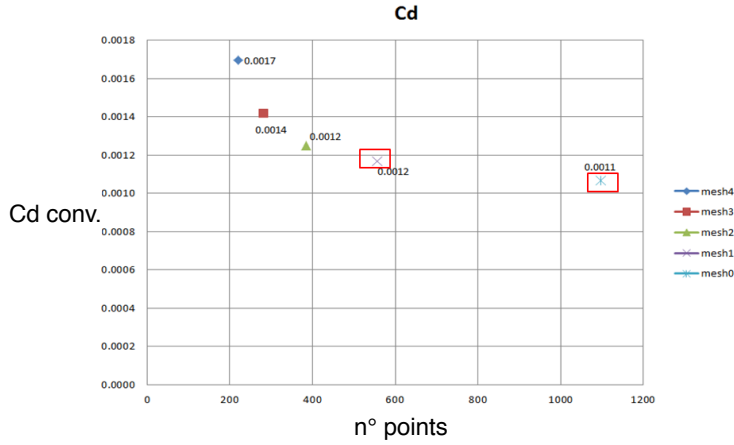


FIGURE 7.12. Value of Cd as a function of the number of points on the surface of the airfoil.

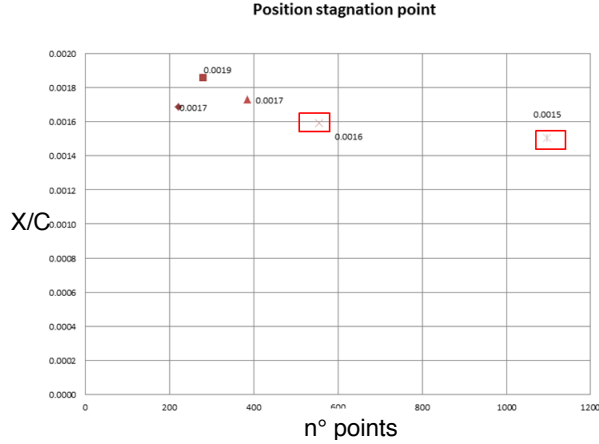


FIGURE 7.13. Comparison between the position of the stagnation point.

The most refined mesh (mesh 0) has been taken as a reference for a good quality. For the coefficients and the stagnation point (Figures 7.12 and 7.13), we see that mesh 1 shows values close to the value of mesh 0. Considering that the computational time using mesh 1 (Table 1) is less than

the time for mesh 0, we have chosen the mesh 1 as the better mesh in terms of quality and time. Unfortunately, the problem of the oscillations on the C_p distribution was not solved yet. Just to test how these oscillations influenced a local stability, we have checked the stability of small perturbations.

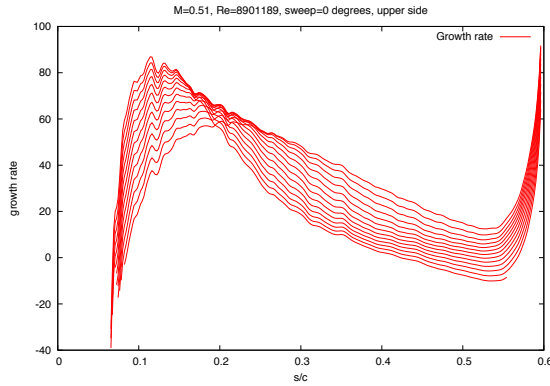


FIGURE 7.14. Oscillations of the growth rate because of a not smooth C_p distribution on the upper side of the airfoil.

Figure 7.14 shows that the growth rate of a perturbation in the flow is very sensitive to the development of pressure distribution on the surface.

2.3. Conclusions. Although the good results found for mesh 1, the C_p distribution still showed small oscillations close to minimum. Like previously said, the numerical dissipations that Fluent introduces in a inviscid case have a great influence on the smoothness of the C_p distribution. Therefore, a viscous analysis could lead to a more smooth distribution of the pressure coefficient on the upper side.

3. Viscous grid

With the same new domain, flight conditions and boundary conditions of the inviscid analysis, we have used the robust Spalart-Allmaras turbulent model.[16].

A viscous study requires a highly refined close to the profile, to consider the effects of the viscosity. To do that, there is the command "inflation". It creates a region close to the profile with thin prism cells.

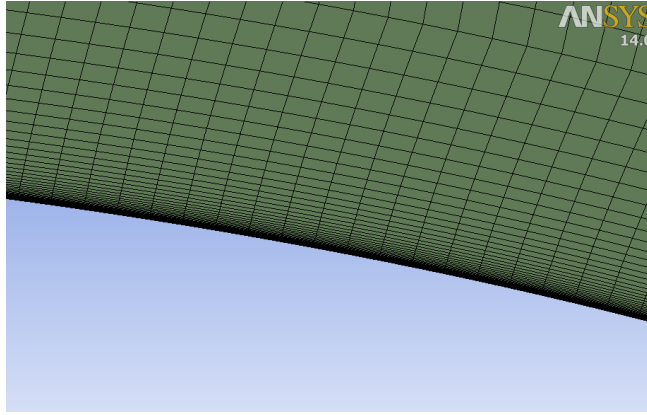


FIGURE 7.15. Grid for viscous analysis. The inflation allows to consider the viscosity effect close to the profile.

To well describe the phenomena in the near wall area, the first cell has to be small enough. A formula exists to find the minimal height of the first cell layer:

$$(3) \quad y = \frac{Y^+ * \nu}{\nu^*}$$

where:

Y^+ = dimensionless wall coordinate, set to a value of 1

ν = Kinematic viscosity of air

ν^* = wall friction velocity

The viscous mesh has been created taking into account the previous results of the pre-processing.

With these assumptions for the grid and CFD, we have computed the C_p

distribution for a viscous case for the profile OASL012, compared with the inviscid one in the Figure 7.16.

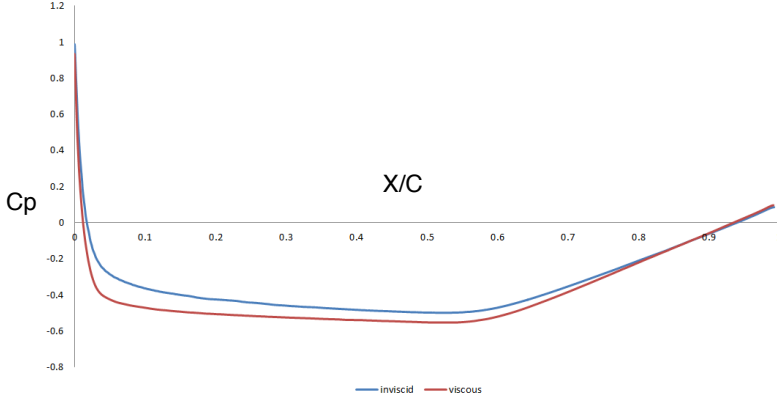


FIGURE 7.16. Comparison between distributions of the pressure coefficient on the upper side for viscous and inviscid case. Profile OASL012. Cruise conditions. 0 degree of angle of attack.

This result allows us to consider a viscous analysis for our optimization, having a good compromise between time calculation and physical results.

4. Validation on TBM profile

After the analysis of the laminar profile OASL012, we tested the grid, CFD, bl3D and the stability code NOLOT for the TBM profile. The flight conditions, like for the OASL012, are the cruise condition of the TBM 850. Although the optimization platform will be made only for 0 degree of angle of attack on cruise conditions, the validation test has been made at different angles of attack.

The results are showed below. As we can see the CFD results are good and the C_p distribution on the upper side is very smooth (Figure 7.17). The stability code finds that transition is around the 26% of the chord (Figure 7.18). This value will be taken as reference for the optimization

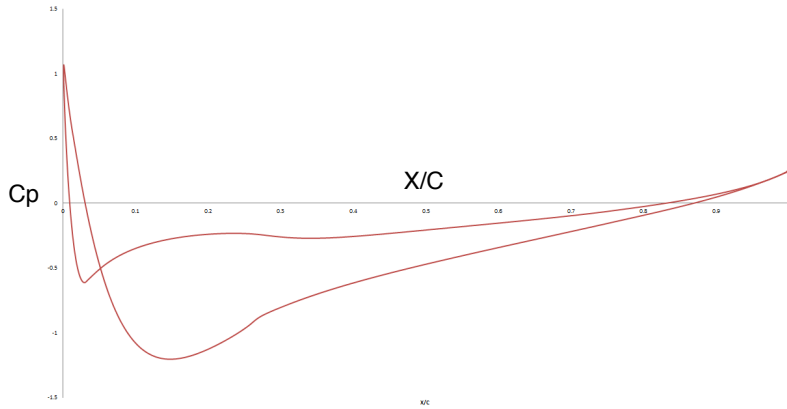


FIGURE 7.17. C_p distribution on the suction and pressure side of TBM profile. Cruise conditions. 0 degree of angle of attack.

process. As previously explained, the main objective will be to move downstream this position as much as possible.

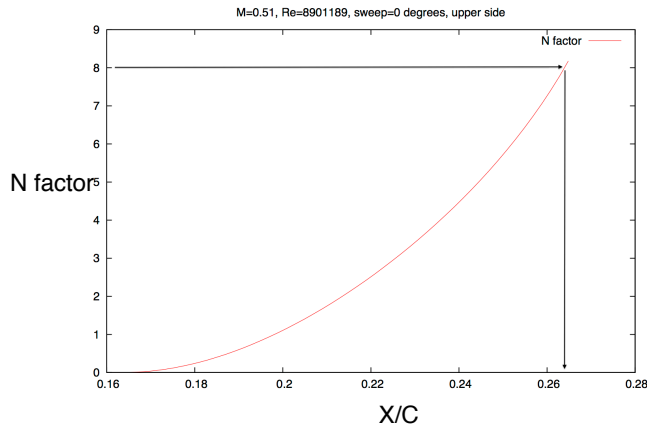


FIGURE 7.18. N factor on the suction side of the TBM profile. Cruise conditions. 0 degree of angle of attack. The black arrow indicates the transition location according to the Mack's Law.

CHAPTER 8

Platform Mode Frontier

After presenting the analysis performed, we can explain how the process has been created inside the platform of modeFRONTIER. The process is created inside the Workflow window and is formed by nodes connected to each other. This italian software offers the possibility to use several types of nodes including:

- **Logic Nodes** where we can find the node for the optimization process
- **Variable Nodes** with the nodes for input and output variables
- **Goal Nodes** to create the objective functions
- **Script Nodes** used here for the Dos Batch Script
- **CAD Nodes** they allow to have a direct connection with CAD software including Catia V 5.

With this procedure the process below has been developed.

In the horizontal direction we see in Figure 8.1 the four steps of the process with Catia, Design Modeler and Mesh, Fluent and bl3D with Nilot. On the other hand, in the vertical direction we have the input and the output data with the Objective functions.

1. Catia node

Inside this Node we have to set the folder of the catia file and select all the points of the geometry that we have chosen as design parameters (symbolized by input variables nodes). As output data for this node we have the geometry in .igs extension, compatible format for Design Modeler.

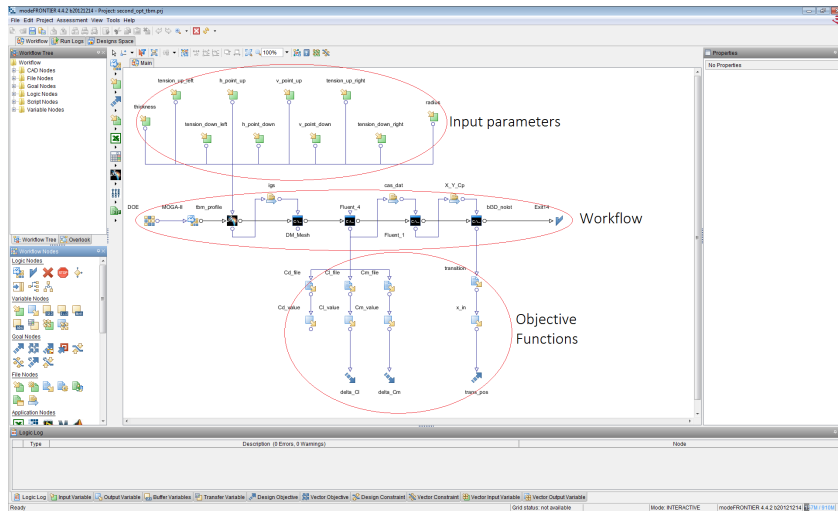


FIGURE 8.1. Interface modeFRONTIER.

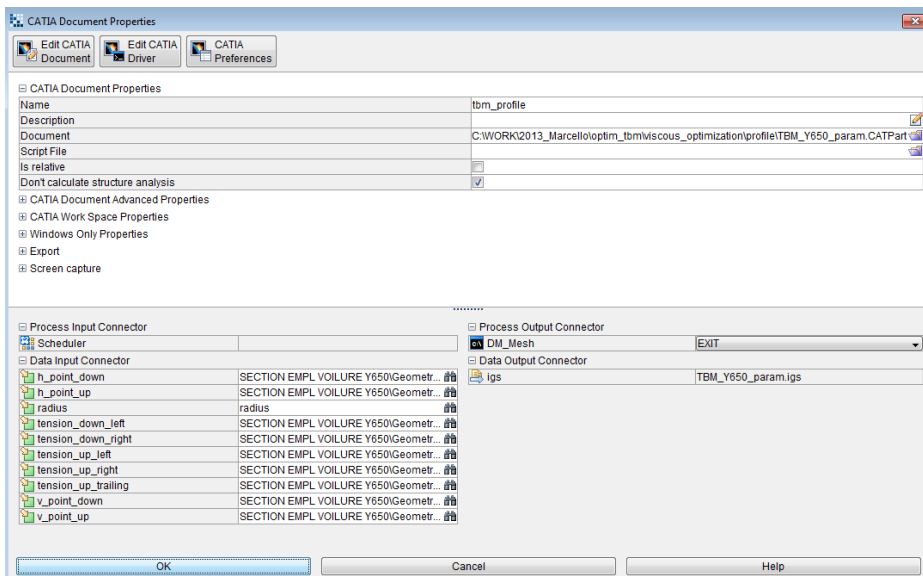


FIGURE 8.2. Interface of the Node Catia inside modeFRONTIER

2. Design Modeler and Mesh nodes

```

1 set optim=C:\WORK\2013_Marcello\optim_tbm\viscous_optimization
2
3 echo Delete old mesh and igs
4 del /Q %optim%\jou_mesh\TBM.msh
5 del /Q %optim%\profile\TBM_Y650_param.igs
6 C:\Applics\cygwin\bin\sleep 2
7
8 echo Copy igs_file for Design Modeler
9 copy /Y TBM_Y650_param.igs %optim%\profile
10
11 :start
12 "C:\Program Files\Ansys Inc\Shared Files\Licensing\win64\lsmutil.exe" lmsat -a -c 10558cfd -A > lics
13 "C:\APPLIS\cygwin\bin\grep.exe" agppi lics | "C:\APPLIS\cygwin\bin\head.exe" -1 | "C:\APPLIS\cygwin\bin\cut.exe" -c 55-56 > isok
14 set testlic=""
15 set /p testlic=ciok
16 del /Q lics isok
17 if %testlic%=="" goto end
18 echo no licence !!!
19 C:\Applics\cygwin\bin\sleep 5
20 goto start
21 :end
22
23 :start1
24 if EXIST TBM_Y650_param.igs goto end1
25 echo no igs file !!
26 C:\Applics\cygwin\bin\sleep 2
27 exit
28 :end1
29
30 echo Start with Design Modeler and Mesh
31 "C:\Program Files\ANSYS Inc\v140\Framework\bin\win64\RunWB2.exe" -B -R %optim%\jou_mesh\journalfile.wbjn -F %optim%\Maillage2D_IGS.wbpj
32 echo OK
33 exit

```

FIGURE 8.3. Dos batch file inside modeFRONTIER to run automatically Deisgn Modeler and Mesh.

A DOS batch has been used to run Design Modeler and the Mesh inside the Ansys platform (Figure 8.3). As we can see, this batch searches the folder of the executable of Ansys to run it. Ansys provides to run the software with scripts. A suitable script has been written to open the .igs file and create the grid in automatic way.

3. Fluent node

Two DOS batches are used to solve the Navier-Stokes's equations and extract the Cp distribution. In fact for the numerical calculation it is better to run Fluent with 4 processors to solve it quickly, whereas to have the distribution of the pressure coefficient need to open Fluent with 1 CPU to have the points in the proper order. For these reasons it will be necessary open Fluent two times. Like the previous node, command lines are used here to read the journal file. For Fluent we can see two different output data: the first is the Cp distribution for the stability code and the

second represents the force coefficients essential to create the objective functions. To run Fluent more quickly, we have decided to use it inside the server with 32 processors.

```

1 set cfd_fold=\cfd\sc0200155\Desktop\tbm_viscous
2 set jou_mesh=C:\WORK\2013_Marcello\optim_tbm\viscous_optimization\jou_mesh
3
4 :start
5 if EXIST %jou_mesh%\TBM.msh goto end
6 echo no mesh file !!
7 C:\Applics\cygwin\bin\sleep 2
8 exit
9 :end
10
11 echo Copy mesh and jou_fluent in server
12 copy /Y %jou_mesh%\tbm_viscous.jou %cfd_fold%
13 copy /Y %jou_mesh%\TBM.msh %cfd_fold%
14
15 echo Licence for Fluent
16 :start1
17 "C:\Program Files\Ansys Inc\Shared Files\Licensing\winx64\lmutil.exe" lmatat -a -c 10558cfd -A > licens
18 "C:\APPLIS\cygwin\bin\grep.exe" acfd_fluent licens | "C:\APPLIS\cygwin\bin\head.exe" -1 | "C:\APPLIS\cygwin\bin\cut.exe" -c 63-64 > control
19 set testlicens=""
20 set /p testlicens=control
21 if not "%testlicens%"=="2\" goto end1
22 echo no acfd licence !!!
23 C:\Applics\cygwin\bin\sleep 5
24 goto start1
25 :end1
26
27 echo Open server
28 "%jou_mesh%\plink.exe" sc0200155@152.60.51.220 -pw spottish < "%jou_mesh%\fluent_server.sh"
29
30 :start2
31 if EXIST %cfd_fold%\TBM-alpha0-Re8.901189-M0.515577.dat.gz goto end2
32 echo not yet running fluent!!
33 C:\Applics\cygwin\bin\sleep 15
34 goto start2
35 :end2
36
37 C:\Applics\cygwin\bin\sleep 2
38 move /Y %cfd_fold%*.
39 C:\Applics\cygwin\bin\sleep 10
40 exit

```

FIGURE 8.4. Example of script to run Fluent automatically inside the platform modeFRONTIER

4. bl3d and NOLOT nodes

This step uses two different codes: one of them is bl3D and it allows to create the viscous region of the boundary layer having the C_p distribution or the U_e distribution around the profile; the second one is the stability code NOLOT. Both of the codes can be used entering into the server and hence a batch script is used to do this (Figure 8.5).

A python code has been created to obtain the C_p distribution on the upper surface and write it to a file suitable for bl3D code, called geo.dat (Figure 8.6).

```

new
1 C:\Applis\cygwin\bin\sleep 2
2 set bl3D_NoIot=\\cfd\sc0200155\Desktop\program_stability\tbm_cruise_condition\alpha0_visc
3 set jou_mesh=C:\WORK\2013_Marcello\optim_tbm\viscous_optimization\jou_mesh
4 :start
5 copy /Y X_Cp_0.dat %bl3D_NoIot%
6 copy /Y X_Y_0.dat %bl3D_NoIot%
7 :exit
8
9 :start1
10 if EXIST X_Cp_0.dat goto end1
11 echo no cp distribution !!
12 C:\Applis\cygwin\bin\sleep 2
13 exit
14 :end1
15
16 echo run bl3D and NoIot
17 "%jou_mesh%\plink.exe" sc0200155@152.60.51.220 -pw spottish < "%jou_mesh%\stability.sh"
18 C:\Applis\cygwin\bin\sleep 3
19
20 echo Take files and transition location
21 move %bl3D_NoIot%\bl_pos.dat
22 move %bl3D_NoIot%\trans_pos.dat_1001
23 move %bl3D_NoIot%\edge.dat_1001
24 move %bl3D_NoIot%\blchar.dat_1001
25 move %bl3D_NoIot%\euro.dat_1001
26 move %bl3D_NoIot%\euro.dat_1001_env_E
27 del /Q %bl3D_NoIot%\modes.in_1001
28 del /Q %bl3D_NoIot%\modes.in
29 del /Q %bl3D_NoIot%\X_Cp_0.dat
30 del /Q %bl3D_NoIot%\X_Y_0.dat
31
32 exit

```

FIGURE 8.5. Batch script in modeFRONTIER to open the server and run NOLOT code.

This python code is thought to locate the stagnation-point value of the C_p distribution and to start from the respective x/c position to create the geo.dat file for bl3D (Figure 8.7). In this file we have to set the chord, the Reynolds and the Mach number, the reference temperature and the sweep on the wing. In the Figure 8.7 we see six columns: the coordinates and the C_p distribution of the profile, two coefficients about the suction at the wall and the heat transfer ¹, and the last one is a respective index useful to bl3D for the calculation.

¹Effect of active control like suction or cooling is used, hence these two coefficient are set to zero

```

import string
import sys
alpha=sys.argv[1]

filecp='X_Cp_'+alpha+'.dat'
filey='X_Y_'+alpha+'.dat'
cpfile=open(filecp,'r')
yfile=open(filey,'r')

linesCp=[]
linesCp=cpfile.readlines()
linesY=[]
linesY=yfile.readlines()

cpfile.close()
yfile.close()
# define variable
cploc=[]
cpmin1=[]
cpmin2=[]
xpos=[]
ypos=[]
cp=[]
# find out value and position of Cp max (stagnation point)
for i in range(4,len(linesCp)-1):
    cploc.append(string.atof(string.strip(string.split(linesCp[i])[1])))
    cpm=string.atof(string.strip(string.split(linesCp[i])[1]))
    cpmax=max(cploc)
    if cpm >= cpmax:
        icpmax=i
ycp=string.atof(string.strip(string.split(linesY[icpmax])[1]))
xcp=string.atof(string.strip(string.split(linesY[icpmax])[0]))
print cpmax,ycp,xcp
# look for first cp negative
for i in (range(4,icpmax)):
    cpmin1.append(string.atof(string.strip(string.split(linesCp[i])[1])))
    min1=min(cpmin1)
# look for second cp negative
for i in (range(icpmax,len(linesCp)-20)):
    cpmin2.append(string.atof(string.strip(string.split(linesCp[i])[1])))
    min2=min(cpmin2)
# define 1'upper side
if min1 < min2:
    for i in (range(4,icpmax+1)):
        xpos.append(string.atof(string.strip(string.split(linesCp[i])[0])))
        ypos.append(string.atof(string.strip(string.split(linesY[i])[1])))
        cp.append(string.atof(string.strip(string.split(linesCp[i])[1])))
    xpos.reverse()
    ypos.reverse()
    cp.reverse()
else:
    for i in (range(icpmax,len(linesCp)-1)):
        xpos.append(string.atof(string.strip(string.split(linesCp[i])[0])))
        ypos.append(string.atof(string.strip(string.split(linesY[i])[1])))
        cp.append(string.atof(string.strip(string.split(linesCp[i])[1])))
# copy in geo.dat
geofile=open('geo.dat_1001','w')
linesout=[]
linesout.append('# CHORD RE MACH TREF SWEEP\n')
linesout.append('1.00073 8901189 0.5155 253.64 0\n')
linesout.append('# X/C Y/C Cp CQ TW\n')

geofile.writelines(linesout)
for i in range(len(cp)):
    j=i+1
    geofile.write("%8f " %xpos[i] + "%8f " %ypos[i]+ "%8f \t0\t0\t"%cp[i]+"%d \n" %j)
geofile.close()

```

FIGURE 8.6. Python code that finds the value and position of the stagnation point and extracts the Cp distribution on the upper side: from stagnation point to trailing edge.

#	CHORD	RE	MACH	TREF	SWEEP		
1.	0.00073	8901189	0.5155	253.64	0		
#	X/C	Y/C	Cp	CQ	TW	index	
0.	0.00107474	0.01054080	1.06726000	0	0	1	
0.	0.00120262	0.01143590	1.06688000	0	0	2	
0.	0.00134772	0.01232760	1.06455000	0	0	3	
0.	0.00150932	0.01321690	1.06049000	0	0	4	
0.	0.00168883	0.01411420	1.05471000	0	0	5	
0.	0.00188761	0.01502540	1.04729000	0	0	6	
0.	0.00210828	0.01596020	1.03819000	0	0	7	
0.	0.00235429	0.01692900	1.02729000	0	0	8	
0.	0.00262787	0.01793520	1.01454000	0	0	9	
0.	0.00293077	0.01898020	0.99988700	0	0	10	
0.	0.00326486	0.02006560	0.98328300	0	0	11	
0.	0.00363214	0.02119310	0.96465100	0	0	12	
0.	0.00403464	0.02236470	0.94389500	0	0	13	
0.	0.00447445	0.02358120	0.92093700	0	0	14	
0.	0.00495399	0.02484410	0.89569800	0	0	15	
0.	0.00547576	0.02615500	0.86803700	0	0	16	
0.	0.00603254	0.02749240	0.83832700	0	0	17	
0.	0.00661399	0.02883140	0.80710500	0	0	18	
0.	0.00721404	0.03016020	0.77460300	0	0	19	
0.	0.00782704	0.03146950	0.74097800	0	0	20	
0.	0.00844596	0.03274790	0.70649000	0	0	21	
0.	0.00905707	0.03397160	0.67181400	0	0	22	
0.	0.00965536	0.03513640	0.63708000	0	0	23	
0.	0.01023760	0.03624130	0.60226700	0	0	24	
0.	0.01080570	0.03729430	0.56698000	0	0	25	

FIGURE 8.7. geo.dat file containing the Cp distribution on the suction side of the airfoil.

From the results of the stability code, it is important to know the position where the N-factor is 8². To extract this position, a Python code has been created (Figure 8.8). This code considers the maximum position corresponding to the range of N factor between 0 and 8. According to the physical phenomenon, if the value of 8 is not reached, it is possible that we have a separation before transition, and in this case it will be important

²Section 4 "Transition Prediction Model" in Chapter 4

find the position corresponding the separation to maximize it as well as the transition one.

```
import string
import sys

nfac=open('euro.dat_1001_env_E','r')

lines=[]
lines=nfac.readlines()

nfac.close()

xpos=[]
lowpos=[]
Npos=[]

# determine transition position
for i in range(2,len(lines)):
    Npos=string.atof(string.strip(string.split(lines[i])[7]))
    if Npos>8:
        for i in range(2,len(lines)):
            lowpos=string.atof(string.strip(string.split(lines[i])[7]))
            if lowpos<8:
                imin=i
                x1=string.atof(string.strip(string.split(lines[imin])[0]))
                n1=string.atof(string.strip(string.split(lines[imin])[7]))
                x2=string.atof(string.strip(string.split(lines[imin+1])[0]))
                n2=string.atof(string.strip(string.split(lines[imin+1])[7]))
                xpos=x1+(8-n1)/(n2-n1)*(x2-x1)
            else:
                xpos=string.atof(string.strip(string.split(lines[i])[1]))
print xpos

trans_pos=open('trans_pos.dat_1001', 'w')
trans_pos.write('x_in = ' "%.8f " %xpos)
trans_pos.close()
```

FIGURE 8.8. Python script to read the results from Nolot code and to extract the transition position.

CHAPTER 9

Viscous Optimization Cruise Conditions

After presenting the physical phenomena, the numerical models and the building of all the automatic process, we can present the results of the optimization. Therefore, in this chapter we explained the procedure, the choices and the results of the first optimization process.

1. Search DOE

In the first step we explore the domain of design parameters. This point is indispensable to have the greatest amount of information from a limited number of parameters and it is called DOE (Design Of Experiments).

To do that, we have used the algorithm Sobol that is a deterministic algorithm with a type of sequence called **quasi-random** even if this algorithm covers the design space in a good uniform manner. For the great influence between the shape and the range of each design parameter, it was quite predictable that in this first phase a lot number of designs gave unfeasible shapes.

The objective of this first exploration of the design space was to see if the designs covered all the range of design parameters and how the design parameters influenced and changed the shape of the airfoil and, eventually, to reduce or increase their domains. To check if all the range of the design parameters was covered, modeFRONTIER allows to plot the value of all parameters for each design.

From Figure 9.3 we can see that the Sobol algorithm covers well the domain of the parameters. On the other hand, from Figure 9.1 it was clear that it was necessary to reduce the range of some points. For this reason

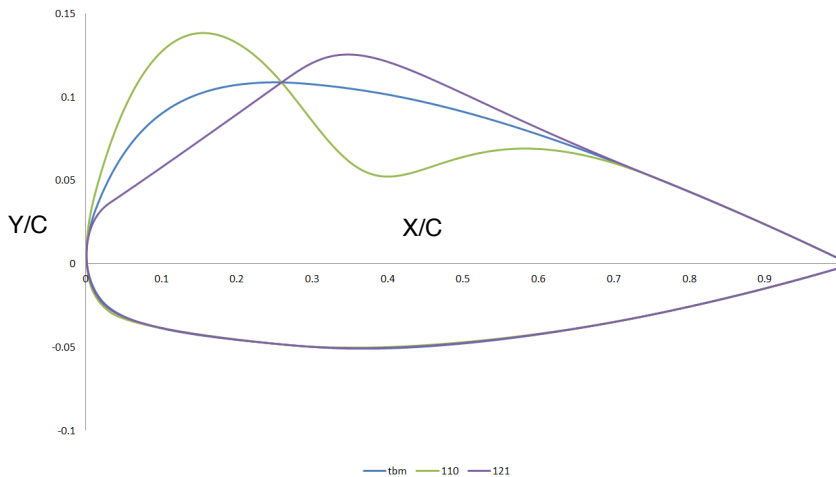


FIGURE 9.1. Two unfeasible shapes from the first DOE with the algorithm Sobol, compared with the TBM airfoil.

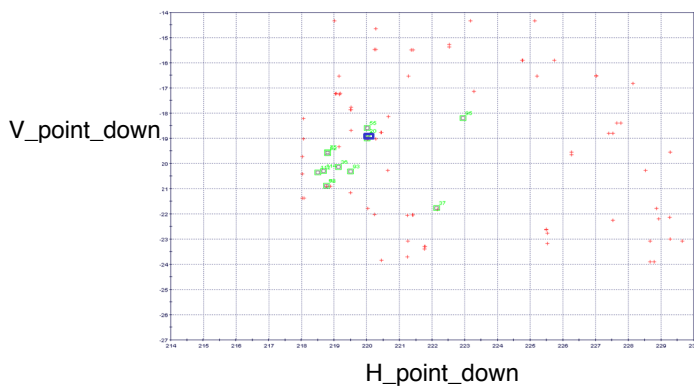


FIGURE 9.2. Example how DOE covered the domain of parameter A in the first exploration. Vertical range as a function of the horizontal range. The blue square represents the value of point 2 for the root airfoil of TBM 850. Green points: feasible design; Red points: unfeasible design.

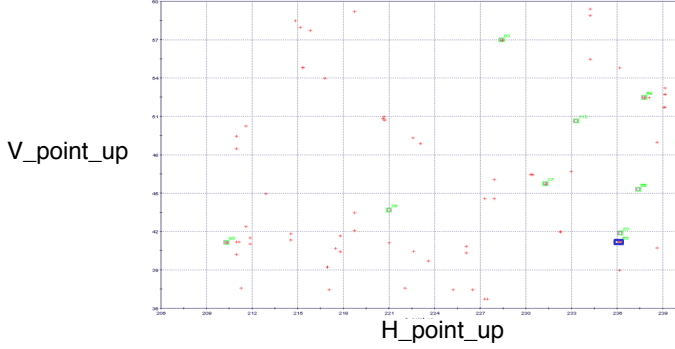


FIGURE 9.3. Example how DOE covered the domain of parameter B in the first exploration. Vertical range as a function of the horizontal range. The blue square represents the value of point 9 for the root airfoil of TBM 850. Green points: feasible design; Red points: unfeasible design.

the range of point 2 and the tension of point 3 were reduced.¹

With these new values, the DOE was used again. The DOE was stopped after 100 design point. The shapes of the profile were more feasible (Figure 9.4) but for most of them the transition was found before the relative position on the TBM profile. For this reason these profiles weren't considered suitable.

Although the shape is not so different from the TBM's one, as already explained, the pressure distribution is very sensitive to changes of the shape. This is clear looking at the Figure 9.5 where we can see very different C_p distribution along the chord of the profile.

The results obtained above didn't allow to have good enough DOE to start with an optimization algorithm. The quality of the optimum depends in fact on the quality of the DOE. Therefore, to have better results from the optimization we decided to start with only designs that had a transition location after than TBM's one. For this reason another DOE has been

¹To know which part of the profile these point control, refer to 6.2

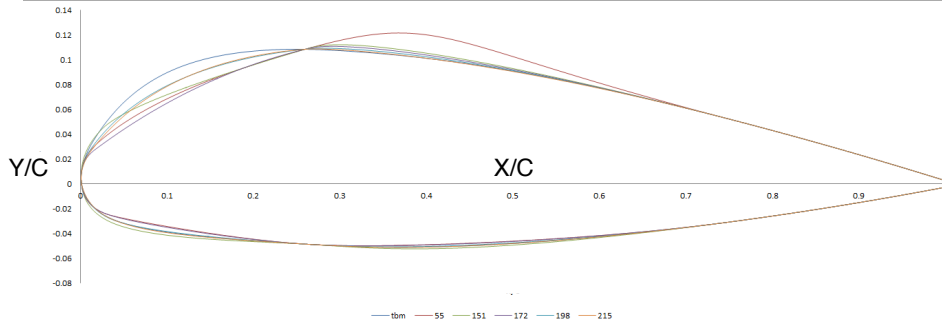


FIGURE 9.4. Some shapes from the second iteration of DOE. The shapes are compared with the TBM's one.

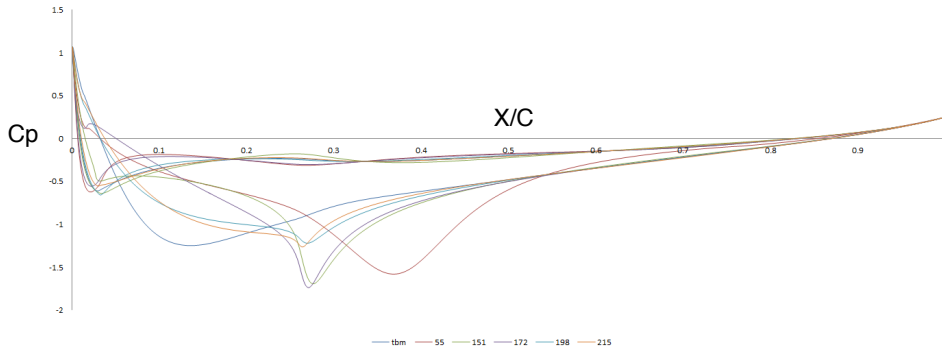


FIGURE 9.5. C_p distribution of the shape of 9.4. The possible transition for each shape is close to the first change of the pressure gradient.

computed, finding a number of design adequate to run an optimization algorithm.

2. Optimization Algorithms

2.1. MOGA II.

2.1.1. *Minimal DOE and Generations.* To run the optimization, a Genetic Algorithm called MOGA II has been chosen. According to the modeFRONTIER's Guide, this algorithm requires a minimal number of

DOE and of Generations to obtain a good evaluation of the results[17]. The minimum number of DOE is given by the following relation:

$$(4) \quad minDOE = 2 * n$$

where n is the number of input variables. Having 10 variables, we have decided to start with 30 DOE, to have a safety margin. On the other hand, the number of Generations is required between 10 and 30. It has been set to 20.

2.1.2. Results. The process has required a duration of 8 days, analyzing 399 profiles. 190 profiles were considered failed because they had a boundary layer that ended upstream compared to the TBM.

On the other hand, 209 profiles showed a boundary layer that ended downstream of the boundary layer of the TBM profile. Only 27 of them had a transition location downstream of the TBM (Figure 9.6)

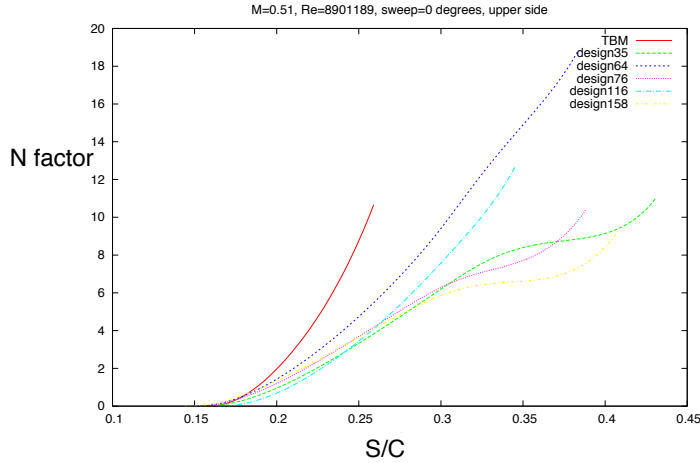


FIGURE 9.6. N factor of some profiles with a transition after the TBM.

For the remaining 182 good profiles, we didn't find a transition location before the end of the boundary layer (Figure 9.7).

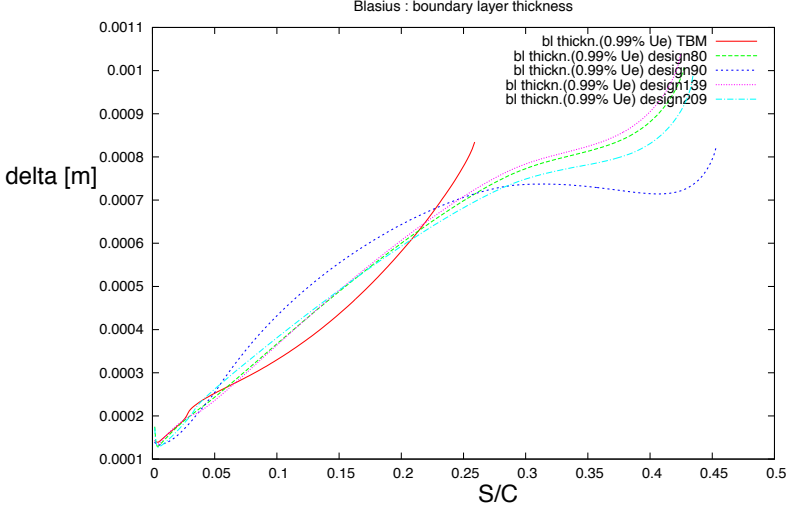


FIGURE 9.7. Laminar boundary layer of some profile of optimization as a function of the curvilinear axis.

This fact can be expressed physically: if the pressure gradient at the leading edge is strong and adverse, the mixing process is too slow to keep the lower part of the layer moving, and a dead-waged region starts to form. The boundary layer doesn't follow the direction of the surface and separates before a transition[18].

Looking at the history of the process (Figure 9.8), we can notice a trend to converge to values of the end of the boundary layer (e.b.l.) further downstream than the TBM.

Figure 9.9 represents the value of the Objective Functions δCl and e.b.l of all the acceptable profiles. The black line represents the Pareto Front which is a state of allocation of resources in which it is impossible to make any one individual better off without making at least one individual worse off.

As Figure 9.9 shows, all the value of δCl are very small, and this means that the value of Cl of the profiles is close to the Cl of the TBM (difference

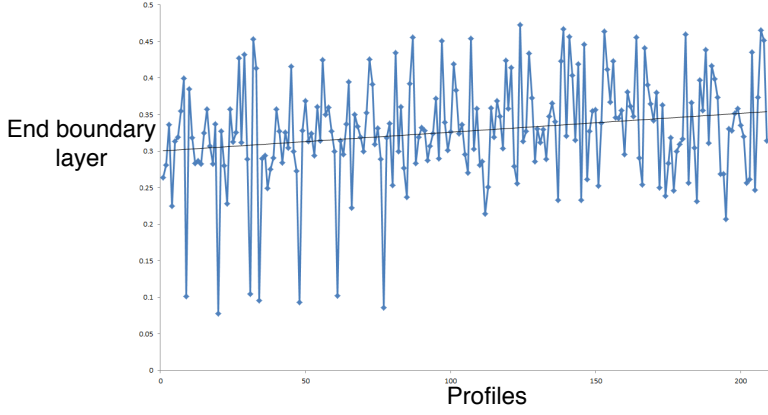


FIGURE 9.8. History of the process. The black line shows a tendency to search shape with a e.b.l more downstream than the TBM.

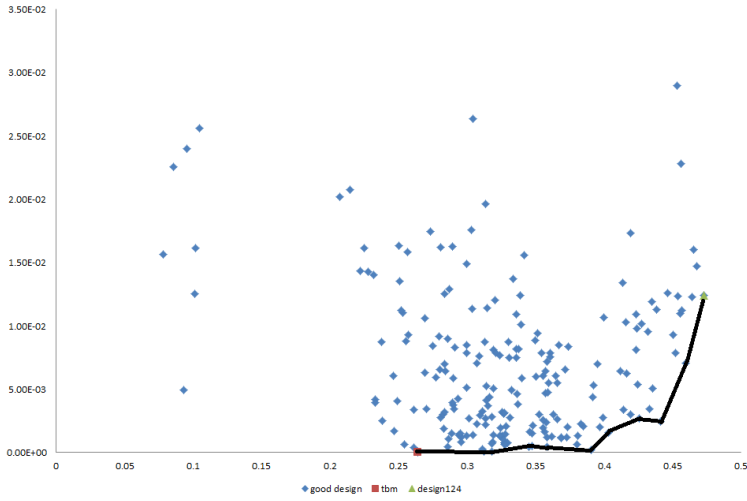


FIGURE 9.9. δCl as a function of the e.b.l. Black line: Pareto front. Red point: TBM. Green point: best design.

between 0.01% and 3%). The same results have been found for δCm . Therefore, these Objective Functions are not very penalized in the process.

This fact has allowed us to consider the shape with the highest value of e.b.l like the best profile. Figures 9.10 and 9.11 show the shape and the C_p distribution of the best solutions in terms of e.b.l.

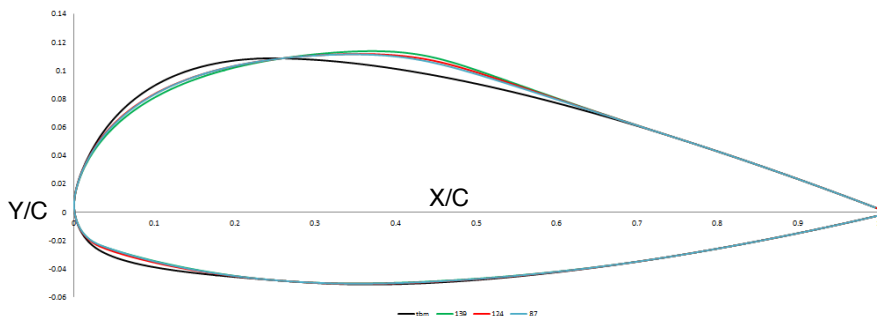


FIGURE 9.10. Shapes of the three best profiles compared with the shape of the TBM.

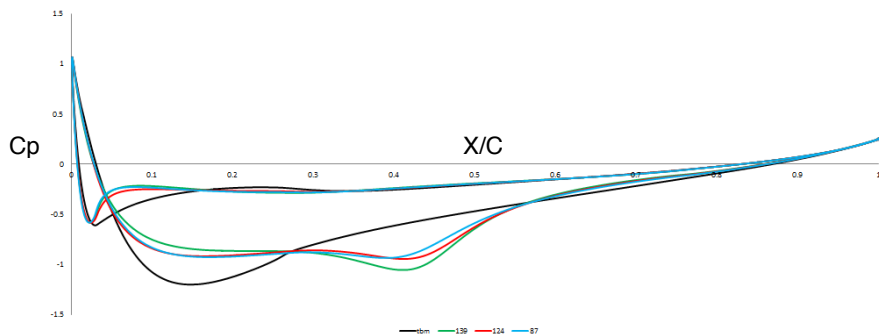


FIGURE 9.11. C_p distribution of the three best profiles compared with the C_p distribution of the TBM.

Looking at these Figures, the pressure reaches its minimum value somewhere around the position of maximum thickness on the upper surface. After this, the pressure gradually rises again, until it returns to a value close to the original free-stream pressure, at the trailing edge. This means, that over the rear part of the upper surface, the air has to travel from low

to high pressure (adverse pressure gradient) and it will lead to separation. The more smooth the shape is, the more gradual will the variation of pressure be and the risk of separation will be reduced. As we can see, the algorithm MOGA II has tried to smooth as much as possible the leading edge. Table 1 shows the value of the Objective Functions of the design plotted above:

TABLE 1. Value of the Objective Functions of the best profiles

Design	e.b.l.	δCl	δCm
TBM	0.264	-	-
87	0.455	0.011	0.008
139	0.467	0.015	0.012
124	0.473	0.012	0.009

The profile 124 has the best solution in terms of e.b.l. and all the values of the other two objective functions are very close to the values of the TBM. For these reasons the profile 124 represents the best solution we have found. The position of the boundary layer is plotted on Figure 9.12 and it is compared with the boundary layer of the TBM.

2.1.3. Discussion. The strategy used in this optimization has allowed to obtain good results. In fact, the genetic optimization algorithm MOGA II, coupled with the algorithm Sobol for the DOE were able to explore all the domain of the design parameters and to find an airfoil with a laminar boundary layer until the 47% of the curvilinear axis. It is known that the laminar boundary layer is very sensitive to big variations of the pressure gradient. It is important to remember that smooth shape of the upper surface lead to a gradual variations of the pressure gradient. Looking at the Figure 9.10, we can see how the process has tried to obtain smooth shape, according with the constraints at 25% and 75% of the chord, and therefore we can be satisfied for the results obtained.

As most of the optimization processes require, after a first global search of the optimal solution, it is useful to refine the study with a gradient based

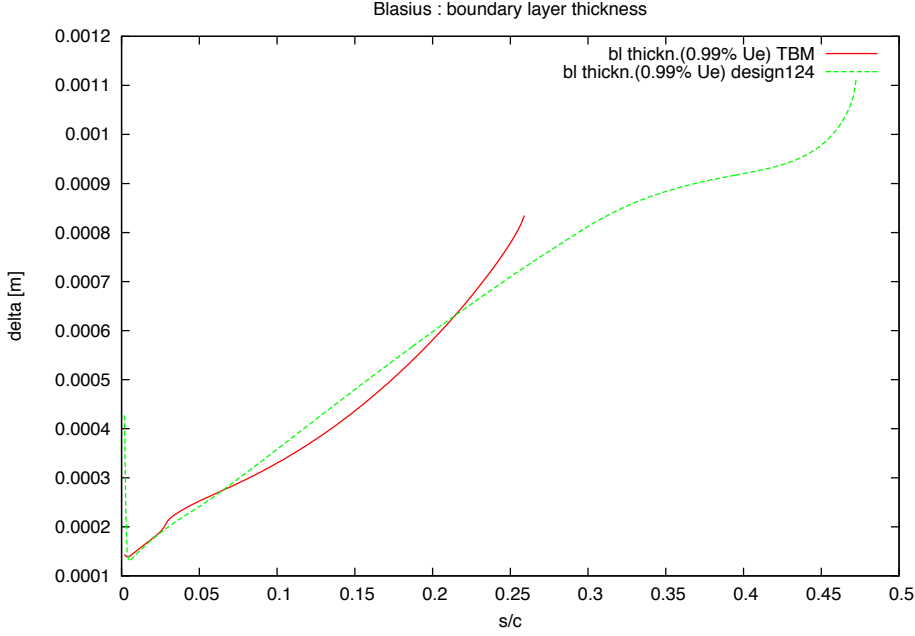


FIGURE 9.12. Boundary layer of TBM compared with the boundary layer of the profile 124.

algorithm. Therefore, we have decided to run the process with a gradient based algorithm to refine our solution. This strategy allows also to have a more robust solution, exploring and testing a lot of points close to the local optimum. This latter point is very important in this process, if we think at a possible production of the final airfoil.

2.2. Gradient Based.

2.2.1. Results. The process has required a duration of about 4 days, analyzing 213 profiles. More than half (120) failed. 50 of them failed for a problem of over flow on the gradient based algorithm. This problem is given by a not correct choice of the step of descent dk^2 . The other

²View Chapter 5/Section 4 - Gradient Based -

70 profiles had a laminar boundary layer that separated upstream of the 'starting design (design 124).' (Figure 9.13)

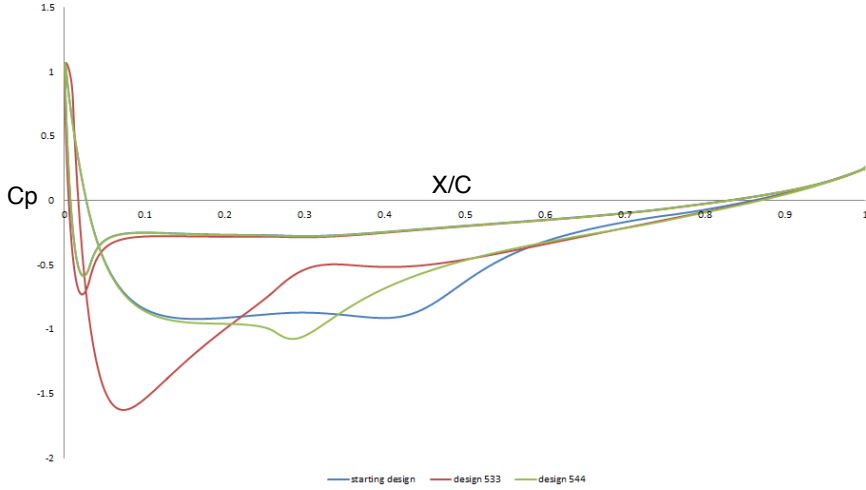


FIGURE 9.13. Pressure coefficient of two failed profiles compared with the starting design.

Looking at the acceptable profiles, the algorithm hasn't found any point with a e.b.l. better than the previous one. On the other hand, we have found a profile with a e.b.l. close to the best one, but with a transition position that occurs before the separation (Table 2).

TABLE 2. Value of the Objective Functions of the best profiles

Design	trans	e.b.l.	δCl	δCm
TBM	0.264	0.270	-	-
124	-	0.473	0.012	0.009
75	0.458	0.470	0.012	0.009

The two shapes and their C_p distribution have been plotted on the Figure 9.14 and 9.15

The presence of the transition on the airfoil 75 is due to a weaker adverse pressure gradient at point A.

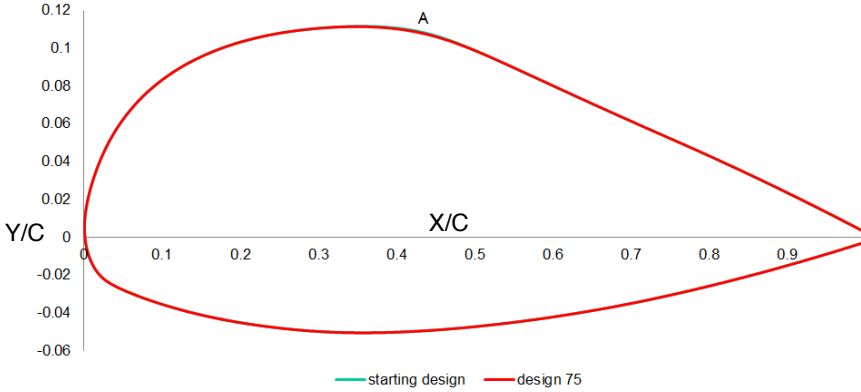


FIGURE 9.14. Comparison between the shapes of profile 124 (best by MOGA II) and 75 (best by Gradient-based). The plot shows a small difference at the point A: the profile 75 has a variation of the shape most gradual.

2.2.2. Discussion. The gradient based algorithm has the big disadvantage to have a very slow convergence. Generally it requires a very large number of test to converge to a optimal solution. Limited by time, we have hence stopped the process after a reasonable time, obtaining results not so different from the previous one. Looking at the results, we can notice the difficulty to find satisfactory profiles despite small variations of the control points. This fact proves once again the great sensibility of the laminar boundary layer to the shape variations. This problem generates the real difficulty of building wings that respected the same characteristics of the ideal model.

The Figure 9.16 shows a great sensibility of the transition to a small variations of the leading edge.

Therefore, the results proves that the optimal solution is not so robust.

On the other hand, the gradient based algorithm has allowed to obtain a design a little smoother compared to the previous with a transition at 46% of the curvilinear axis.

Considering that for reasons of aircraft control, the transition phenomenon

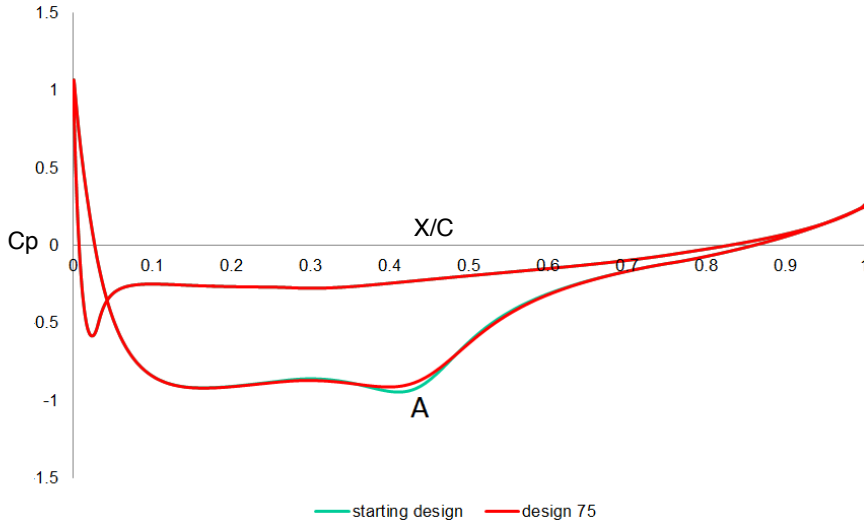


FIGURE 9.15. Comparison between the C_p distribution of profiles 124 and 75. The profile 75 has a lower adverse pressure gradient because of smoothness at point A (Figure 9.14).

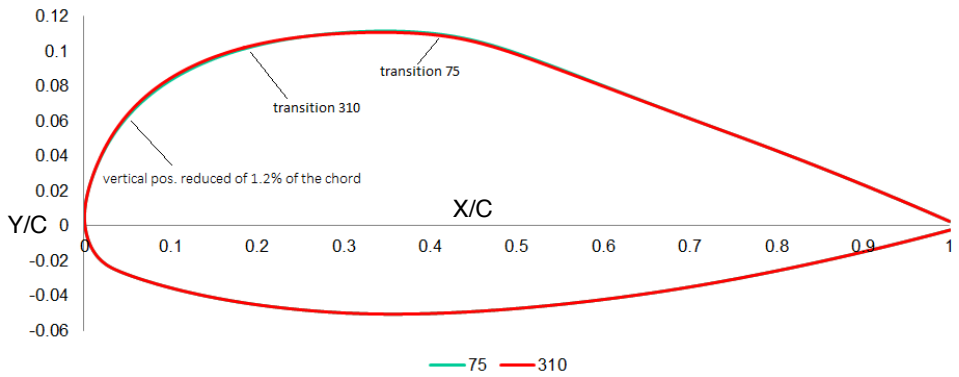


FIGURE 9.16. Comparison between profile 310 and 75. A small variation of the vertical position of the point that control the leading edge (only 1.27 mm) leads forward the transition of 50 %.

is better than the separation, we have considered the profile 75 like our optimal solution.

To have an idea of the reduction of the total drag between this profile and the TBM, we have decided to solve the flow around the two profiles with a Transition Model.

3. Drag Evaluation

3.1. Transition Models. A Transition Model allows the reliable prediction of the onset and extent of laminar-turbulent transition. The Ansys platform has developed two Transition Models, named the SST-transition and the k-kl transition model[19]. Due to its combination with the SST model, the SST-transition is favored. Coupling of Navier-Stokes code with a global turbulence model, this model allows to predict the position of the natural transition.

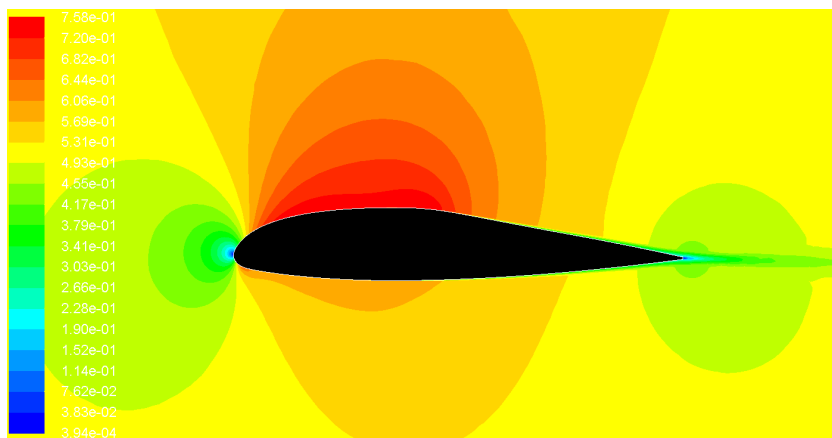


FIGURE 9.17. Example of transition model by Fluent. Distribution of the mach number around the profile. Cruise conditions: Mach 0.51; Altitude 26000 feet; Angle of attack 0.

3.2. SST-transition model results and discussion. After creating a Journal File with the same flight conditions and boundary conditions used for the RANS model, we have run a CFD simulation with the SST-transition model for the wing root airfoil of the TBM 850 and for the optimal solution (profile 75). As explained in the Chapter 3, the skin friction increases a lot because of the transition phenomenon. Therefore, a simple way to see where the transition occurs is to plot the value of the skin friction on the upper surface.

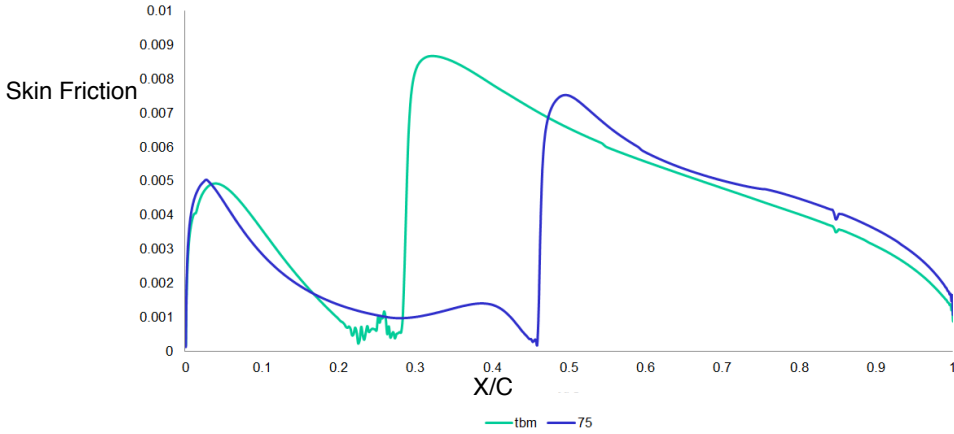


FIGURE 9.18. Comparison between the skin friction of the TBM and of the design 75. SST-transition model. Cruise conditions. 0 degree of angle of attack.

Figure 9.18 proves the results obtained by the stability code NOLOT. In fact, for the profile 75 a transition occurs after the position on the TBM profile. This difference in the transition location produces a reduction of 18,86% of the total drag, as one can see in table 3.

The results are in agreement with the physical phenomena. In fact, a more extended laminar boundary layer has more effect on the skin friction than on the pressure drag.

Looking at the Figure 9.19 we can see the value of the pressure drag and skin friction of the two airfoil

TABLE 3. Drag reduction between TBM and design 75.

	Friction drag	Pressure drag	Total drag
Reduction	14.26%	4.6%	18.86%

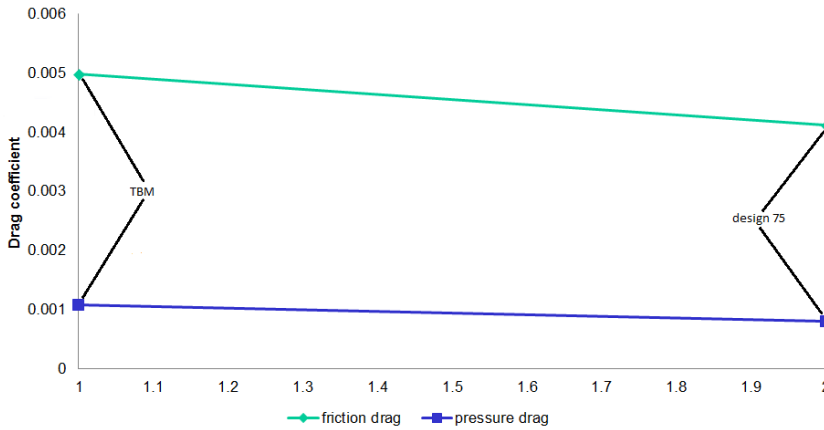


FIGURE 9.19. Pressure drag and skin friction before and after the optimization process.

4. Conclusions

The final results can be considered satisfactory. In fact, maintaining the value of lift and momentum coefficient close to the original geometry, the optimal solution decreases the total drag more than 18%. This reduction is due to a transition moved from 26% to 45% of the curvilinear axis. Therefore, we conclude that the optimization strategy used is suitable for this type of problems.

The phenomena of transition and separation are very sensitive to the smoothness of the profile and often occur close to the maximum thickness of the airfoil. The constraints of the thickness at 25% of the chord didn't allow us to smooth very much the shape and to move the maximum thickness downstream to 40% of the chord. For this reason we think that a

shape with less constraints on the thickness could obtain better results in terms of transition/separation. On the other hand, the parameterization could be more taxing and the optimization more expensive.

Besides, large modifications of the thickness of a wing can lead to structural problems compared with the original wing. It is for these problems that we have also tried to reduce the degrees of freedom of the shape. The process, however, has shown problems in finding a robust solution. In fact the best shape exhibits very different results for small variations of the control points. Therefore, from a manufacturing point of view, we think that the process should be considered insufficient.

CHAPTER 10

Viscous Optimization High and Low speed

After optimizing the profile at high speed, we decided to analyze its stall characteristics at low speed. Therefore we improved the process for two different flight conditions. One of them is the cruise condition, already used for the previous optimization. The second one is the take off. The goal was to optimize two profiles for the two different flight conditions at the same time. The two airfoils analyzed were the root and the tip profiles because they represent the profiles generators of the wing. Therefore a new platform was created in modeFRONTIER.

1. Take-off/Landing conditions

During the flight envelope the performance requirements of the aircraft changes. In fact at cruise conditions we want the aircraft to be efficient in terms of fuel consumption. On the other hand, at take off a great lift is required to allow to the aircraft to climb (Figure 10.1).

1.1. Lift generation. For a aircraft, the lift is generated by producing a pressure different between the upper and lower side of the wing. This pressure difference is produced by a inclination of the surface relative to the air flow direction or with a curved surface (cambered) as the profile of the TBM. The angle at which the wing is inclined relative to the air flow is known as the angle of attack. The variation of lift with angle of attack can be calculated by using a single graph of C_l plotted as a function of the angle of attack[20].



FIGURE 10.1. Take off of the TBM. A great value of lift is required during take off.

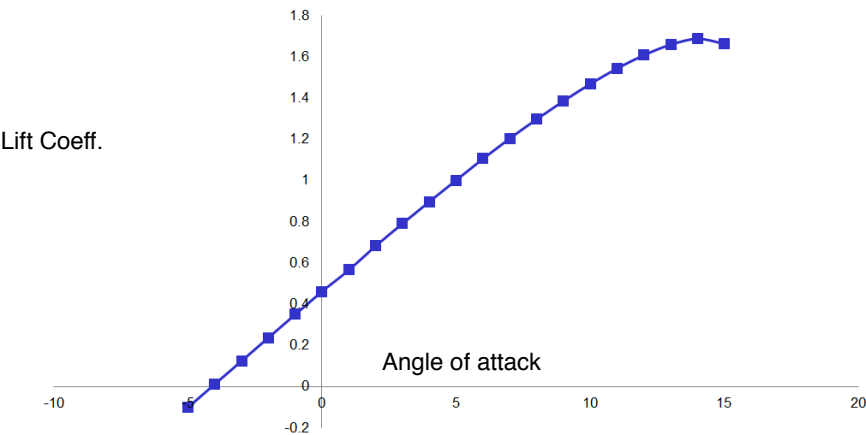


FIGURE 10.2. Lift coefficient against the angle of attack for the root of the wing of the TBM. Altitude 0.

As we can see, the amount of lift is directly proportional to the angle of attack, for small angles. Figure 10.2 shows a straight line until a point where the lift starts to fall off. This effect is known as stalling. In Figure 10.2 the stall occurs at an angle of attack of around 14 degrees. Stalling

occurs when the air flow fails to follow the contours of the airfoil and becomes separated. A delay of the stall allows to stretch the production of lift at larger angles of attack.

2. Changes in the modeFRONTIER platform

Instead of delaying the stall, we have decided to maximize the highest value of lift coefficient. To do that, we have created a loop inside the CFD simulation to study the flow increasing the angle of attack until the maximum Cl . (Figure 10.3)

```
; ciclo do
(do ((aoa 17 (- aoa 1))) ((< dcz 0))
  (ti-menu-load-string (format #f "/report/forces/wall-forces y (-sin(deg2rad -aoa)) (cos(deg2rad -aoa)) y cz,max,dat n y" (- aoa 1) (- aoa 1)))
  (set! cz cz1)
  (display cz)
  (display aoa)
  (ti-menu-load-string (format #f "/define/boundary-conditions/pressure-far-field out n 0 n -a n -a n -a n n n 10" (rpgetvar 'n #f) (rpgetvar 'temperature #f) (cos(deg2rad aoa)) (sin(deg2rad aoa))))
  (ti-menu-load-string (format #f "/solve/monitors/force/drag-coefficient y airfoil {} n y \"\"/cx-history-a.dat\"\" n n -a -a\"\" aoa (cos(deg2rad aoa)) (sin(deg2rad aoa))"))
  (ti-menu-load-string (format #f "/solve/monitors/force/moment-coefficient y airfoil {} n y \"\"/cy-history-a.dat\"\" n n -a -a\"\" aoa (-sin(deg2rad aoa)) (cos(deg2rad aoa))"))
  (ti-menu-load-string (format #f "/solve/set/discretization-scheme/nom 0"))
  (ti-menu-load-string (format #f "/solve/set/discretization-scheme/pressure 10"))
  (ti-menu-load-string (format #f "/solve/set/discretization-scheme/temperature 0"))
  (ti-menu-load-string (format #f "/solve/set/discretization-scheme/density 0"))
  (ti-menu-load-string (format #f "/solve/set/discretization-scheme/nut 0"))
  (ti-menu-load-string (format #f "t 200"))
  (ti-menu-load-string (format #f "/solve/set/discretization-scheme/nom 1"))
  (ti-menu-load-string (format #f "/solve/set/discretization-scheme/pressure 12"))
  (ti-menu-load-string (format #f "/solve/set/discretization-scheme/temperature 1"))
  (ti-menu-load-string (format #f "/solve/set/discretization-scheme/density 1"))
  (ti-menu-load-string (format #f "/solve/set/discretization-scheme/nut 1"))
  (ti-menu-load-string (format #f "t 400"))
  (ti-menu-load-string (format #f "/solve/set/discretization-scheme/nom 0"))
  (ti-menu-load-string (format #f "/solve/set/discretization-scheme/pressure 12"))
  (ti-menu-load-string (format #f "/solve/set/discretization-scheme/temperature 0"))
  (ti-menu-load-string (format #f "/solve/set/discretization-scheme/density 0"))
  (ti-menu-load-string (format #f "/solve/set/discretization-scheme/nut 0"))
  (ti-menu-load-string (format #f "t 500"))
  (rp-var-define 'name "rte" 'char #f)
  (set! cz1 (string-number (pick "/report/forces/wall-forces y (-sin(deg2rad -aoa)) (cos(deg2rad aoa)) n" 1)))
  (display cz1)
  (set! dcz (- cz1 cz2))
  (ti-menu-load-string (format #f "wc -a alpha-a-Re-a-M-a.cas.gz" (rpgetvar 'name #f) aoa (/ (rpgetvar 'nu_objectif #f) 1000000) (rpgetvar 'h #f)))
  (ti-menu-load-string (format #f "wd -a alpha-a-Re-a-M-a.cas.gz" (rpgetvar 'name #f) aoa (/ (rpgetvar 'nu_objectif #f) 1000000) (rpgetvar 'h #f)))
  (display dcz)
)
```

FIGURE 10.3. Loop inside Journal file of fluent.

Therefore, in the optimization process, a new objective function with the value of Cl has been considered. (Figure 10.4)

As we can see in the Figure 10.4, this new flight condition has been coupled with the cruise. The objective of the process is to find a profile capable to reduce the drag at cruising speed at 0 of angle of attack and, at the same time, capable to increase the lift at low speed.

3. Root optimization

This new root optimization consider the same profile of the previous one. For this reason, creating the new platform has not required much time.

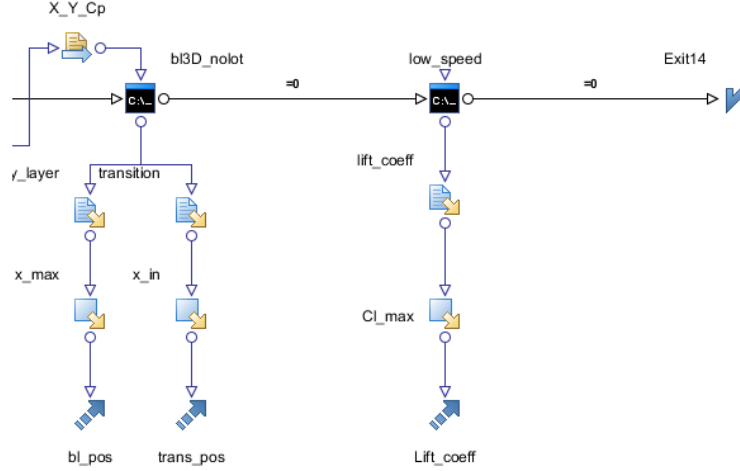


FIGURE 10.4. New interface modeFRONTIER for optimization high/low speed

The only new feature was to integrate the CFD simulation at low speed in the process. The new CFD simulation is very expensive in terms of time. The time of each iteration of the optimization indeed is passed from 30 to 60 minutes.

3.1. Strategy. According to the good results obtained in the process at cruising speed, the strategy used for this optimization is the same as the previous one. Therefore, the domain of the control parameters has been explored with the Sobol algorithm. Secondly, the optimization algorithm MOGA II has been used to find the best solution. 80 DOE have been studied before getting a reasonable number of design to start with MOGA II. The Gradient Based algorithm has not been used to refine the solution. In the previous process indeed it didn't give good results.

3.2. Results. After about 5 days and 300 shapes analyzed, the process was stopped. More than half (170) gave good results. The failed

profiles presented no transition delayed compared with the TBM. In Figure 10.5 are plotted the value of the Lift coefficient at low speed against the e.b.l. at high speed and their Pareto front.

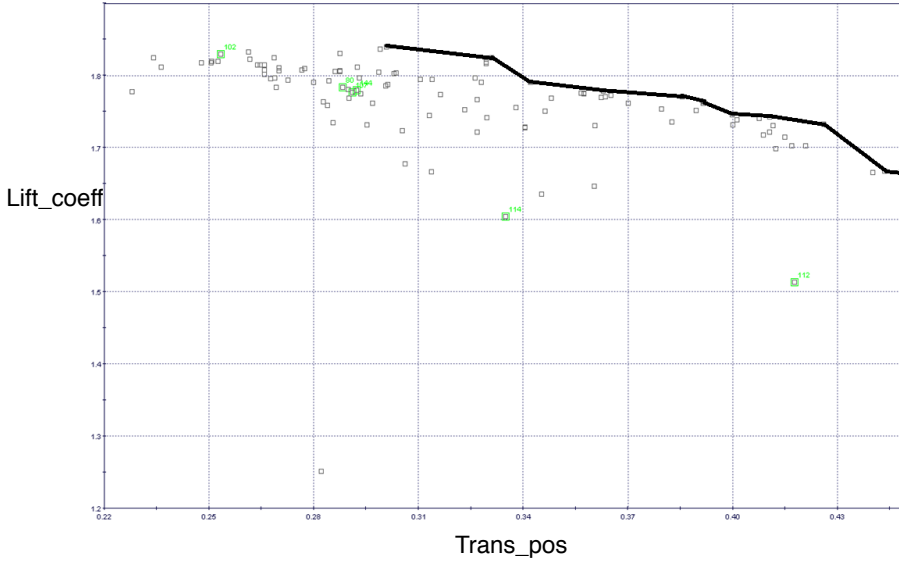


FIGURE 10.5. Pareto front

As the plot shows, these Objective Functions are one in opposition to the other. A profile that assures a low drag at cruising speed is not able to give a high lift coefficient at taking-off speed and vice versa. We can see the two different shapes in the Figure 10.6

After all, although the different flight conditions lead to opposite ways, the process has found good results for each O.F. As regards cruising speed, the best profile presents an e.b.l. at 44.8% of the curvilinear axis. This value is pretty close to the 47% of the previous optimization. This fact says that this O.F. has not been penalized so much by the CFD simulation at low speed.

On the other hand, we have found a maximum Cl of 1.837. This value is 1.2% more than the TBM and it can't be considered a good improvement. These values, compared with TBM, are put on the table 1.

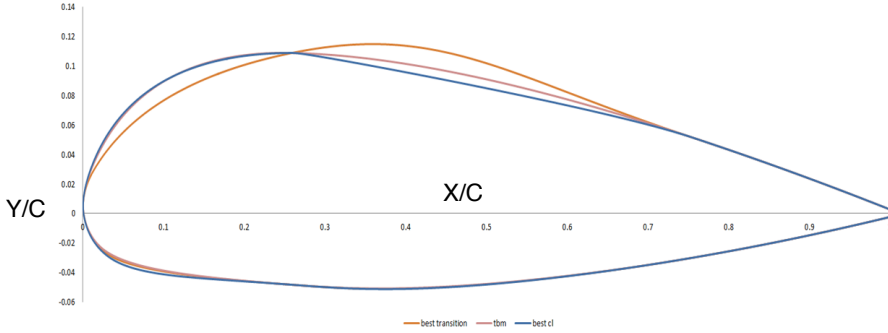


FIGURE 10.6. Best shape for transition and best shape for Lift coefficient compared with the TBM.

TABLE 1. Comparison between the objective functions of TBM and the best shapes at low and high speed.

Profile	e.b.l.	Cl_{max}
TBM	0.264	1.814
best high speed	0.448	1.666
best low speed	0.299	1.837

3.3. Discussion. This analysis has showed how the flight conditions considered require different shapes for their optimization. Although, the strategy applied has found good solutions to maximize the position of transition, it has not been the same for the lift coefficient.

Generally an aircraft spends more time in cruise condition than take-off or land one. For this reason we have preferred to choose a profile with a drag reduced as much as possible but with value of Cl close to the starting value. Therefore, the best choice has been on the profile 355. We can see its shape and characteristics respectively in Figure 10.7 and Table 2.

The value of the max. Cl has been reduced of the 4.57% of the value of TBM. In the Certification Specifications CS-23, the E.A.S.A. imposes that the taking-off speed (V_t) must be at least 1.2 the stalling speed (V_s). The latter must be less than 61 Knots and it is defined by the following

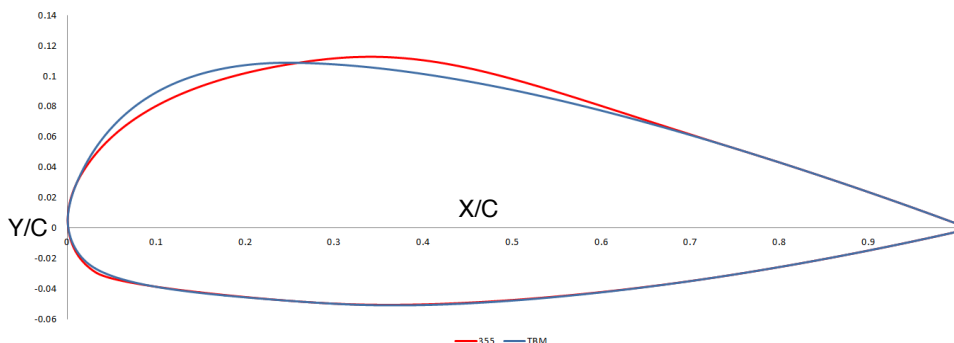


FIGURE 10.7. Shape of the compromise between all the solutions.

TABLE 2. Best compromise

Profile	e.b.l.	Cl_{max}
TBM	0.265	1.815
355	0.426	1.732

equation[21]:

$$M * g = \frac{1}{2} * \rho * S * V_s^2 * Cl$$

As we can see, a too small value of Cl , without changing the others parameters, can increase a lot the value of V_s , not allowing to respect the Certifications. Changes of the Cl of an airfoil lead to changes of the Cl of the aircraft and therefore we have tried to stay as much as possible near to the Cl max of the TBM.

4. Tip optimization

The main difference between the root and tip airfoils is the relative thickness, defined as the ratio of maximum thickness and the chord. In fact, for the first it is 16% and for the second one is 12%

Hence, to create the optimization platform for the tip has required to review all the steps of the process to find the reference values. Since the

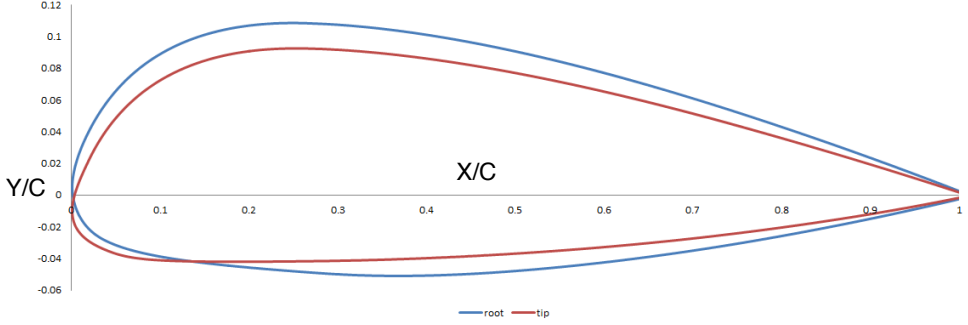


FIGURE 10.8. Comparison between the tip and root profiles. We can see the different relative thickness.

root optimization had given us good results, we have decided to keep the same steps of the previous one. Therefore, the same parameterization, domain, mesh and CFD simulations for high and low speed have been done. The reference values for the TBM show a maximum e.b.l. at 26% of the curvilinear axis while the maximum value of Cl at low speed was 1.82.

4.1. Strategy. The strategy Sobol+MOGA II has been employed. 80 DOE have been studied before having a reasonable number to start with MOGA II.

4.2. Results. The process has been stopped after 263 profiles. Only 67 of them were unfeasible, presenting a transition more upstream than the starting profile. Like for the other optimizations, we have plotted the Pareto Front.

Like for the root, even this process proves the opposition between the two O.F. The best shape for the cruising speed has a e.b.l. at 39% of the curvilinear axis. On the other hand, the best shape for low speed has a Lift coefficient of 1.85. The values of the two best airfoils are put in the Table 3

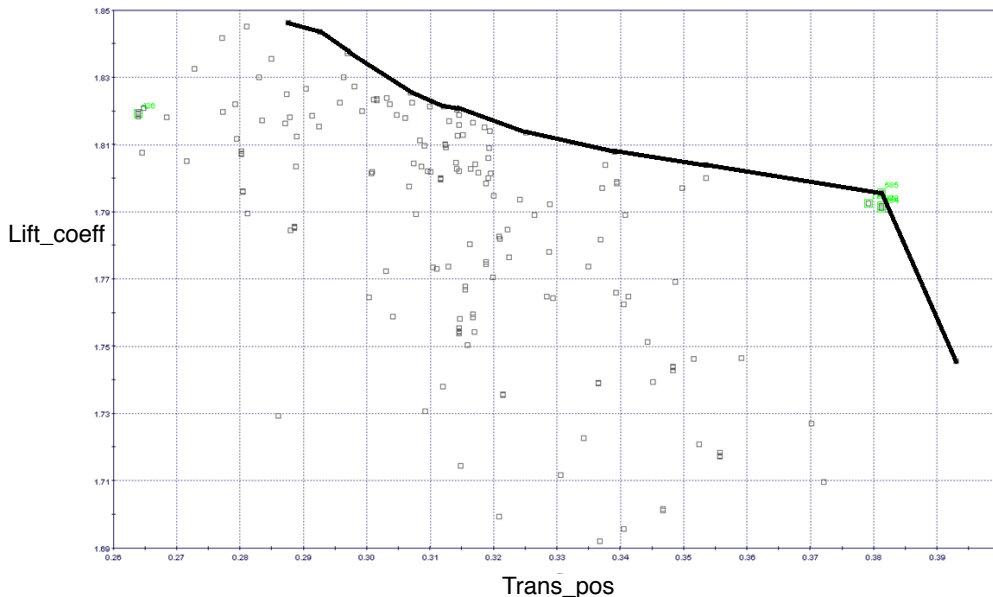


FIGURE 10.9. Pareto front of the solutions.

TABLE 3. Comparison between the objective functions of TBM and the best shapes at low and high speed.

Profile	e.b.l.	Cl_{max}
TBM	0.264	1.819
best high speed	0.393	1.75
best low speed	0.287	1.85

4.3. Discussion. The optimization at low speed has showed better results for the maximum value of Cl . As with the process for the root, the solution must be taken like a compromise among the two O.F. Analyzing the Pareto front the profile 585 has been chosen. We can see its characteristics in the table 4.

TABLE 4. Objective functions of the best compromise, compared with the TBM. Tip profile. High speed: cruise condition; Low speed: take-off condition.

Profile	e.b.l.	Cl_{max}
TBM	0.264	1.819
585	0.381	1.796

CHAPTER 11

Validation 3D: Wing

In this chapter a CFD simulation of the wing of TBM 850 is done. The results are then compared with a CFD simulation of the same wing with different root and tip profiles. In fact, considering the best solutions of the last optimization processes, a ' new ' wing of the TBM is created with these two profiles. This study is done to compare the drag of the two wings at cruising speed with 0 of angle of attack.

It is important to keep in mind that the flows over a 2D and a 3D geometry are very different. In fact 3D effects and trailing vortex can influence the flow over the wing and add drag.

1. Trailing Vortex

First of all on a wing there are effects called trailing vortex that add a contribute to the global drag, called induced drag[22].

The nature of this phenomenon is explained by the different pressure on the sides of the wing. On the lower side of a wing, the pressure is higher than the surrounding atmosphere, so the air flows outwards towards the tip. On the upper surface, the pressure is low, and the air flows inwards. This results in a twisting motion in the air as it leaves the trailing edge.

2. 3D effects

The TBM, like many modern aircraft, is equipped with a small swept-wing configuration. This fact introduces another important effect on the flow. Indeed, as already explained in the chapter 3, the boundary layer developing on swept wings is different from its two-dimensional counterparts

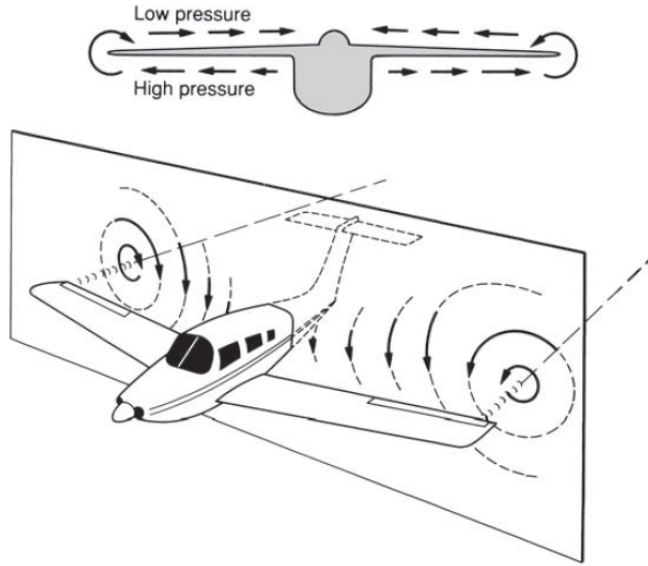


FIGURE 11.1. Generation of trailing vortex behind the wings of an aircraft.

in that it exhibits a crossflow profile[23]. This crossflow profile introduces effects on the boundary layer changing the characteristics of the transition.

For the presence to these effects, the flow over the root and tip profiles can give different results respect to the 2D analysis. Besides, it is important to say that, although Fluent could solve the natural transition of the boundary layer, the numerical method used to do that is less accurate than NOLOT code. Therefore, this difference must be considered in the analysis of the results.

3. TBM wing

The wing of the TBM has been taken as reference. Its characteristics are the following:

- A span of 12161.3 mm

- A dihedral of 6.5

A frontal, lateral and from above view is in the Figure 11.2.

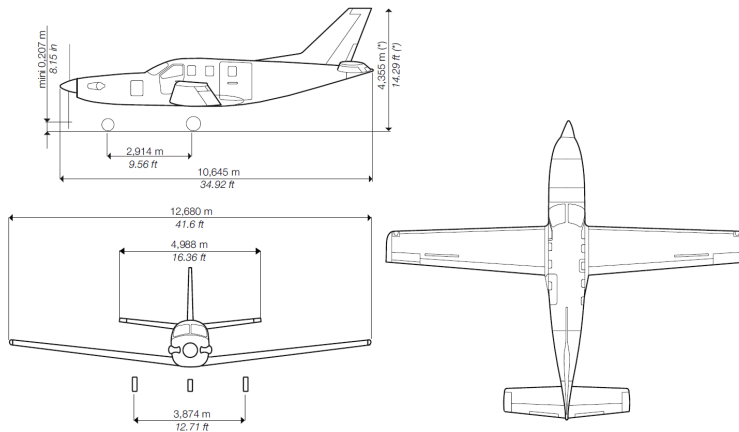


FIGURE 11.2. Main dimensions of the TBM. We can see the dimensions of its wings.

4. Catia V 5

Respecting the list of the main parameters of the wing, the CAD software Catia V 5 has been used to create the ' new ' wing. The wing was built being able to change its dihedral and its span (Figures 11.3 and 11.4).

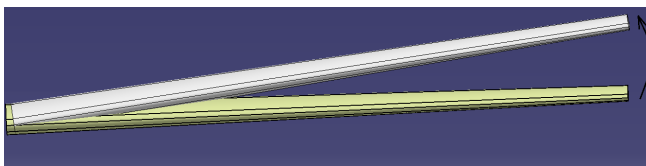


FIGURE 11.3. Variation of the dihedral.

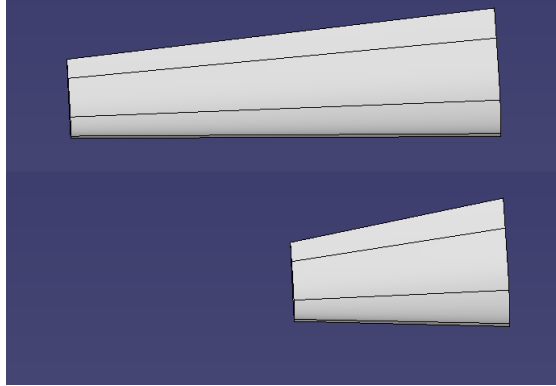


FIGURE 11.4. Variation of the span.

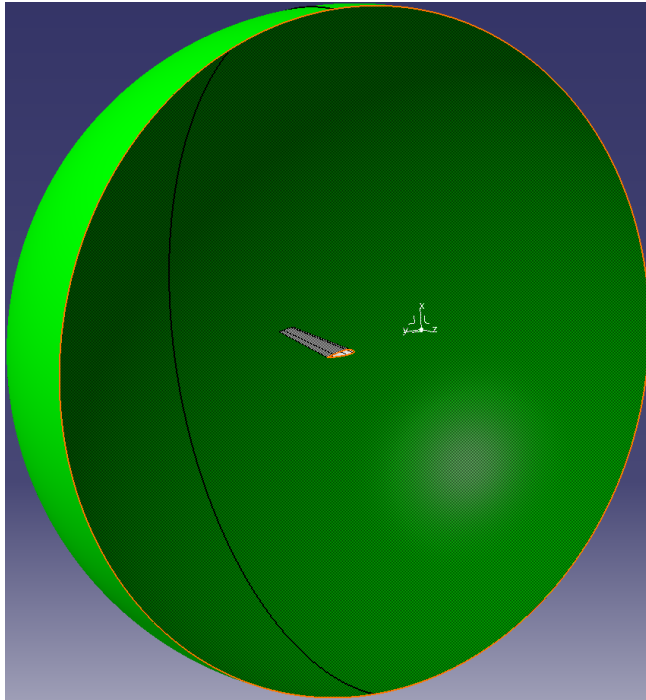


FIGURE 11.5. Half sphere for the fluid domain around the wing.

5. Mesh

A half sphere has been created as the fluid domain. We can see it in Figure 11.5:

The domain has been discretized with Hybrid mesh. The command inflation has been considered close to the wing, to study the effects of the viscosity. The domain so created has 3.8 million of cells. The maximum skewness is 0.93.

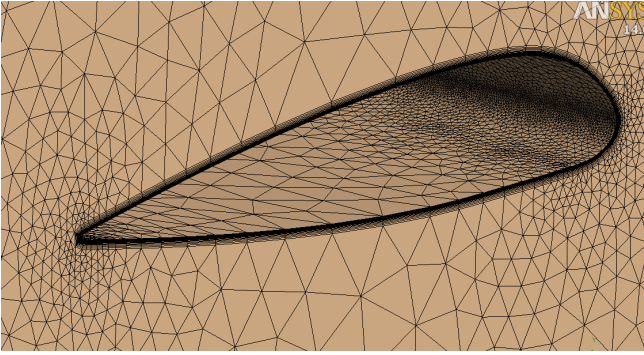


FIGURE 11.6. Grid around the wing.

6. CFD simulation

The SST-transition model has been used to study the natural transition on the two wings. The algorithm method for the continuity and momentum equations is the pressure based solver. The boundary conditions are:

- pressure-far-field to the two surface of the half sphere
- symmetry to the symmetry plane of the half sphere

The algorithm for the solution is Coupled with low values for the under-relaxation factors and a CFL set to 10.

The wings have been studied in the cruise conditions of the TBM 850:

TABLE 1. Cruise conditions of the TBM 850.

Mach number	Reynolds number	Altitude (feet)	Velocity (knots)
0.51	8901189	26.000	320

7. Results

The CFD simulation has given unexpected results in terms of drag. In fact, as we can see in the Figures 11.7 and 11.8, high values of skin friction are more extended on the surface of the new wing than on the TBM.

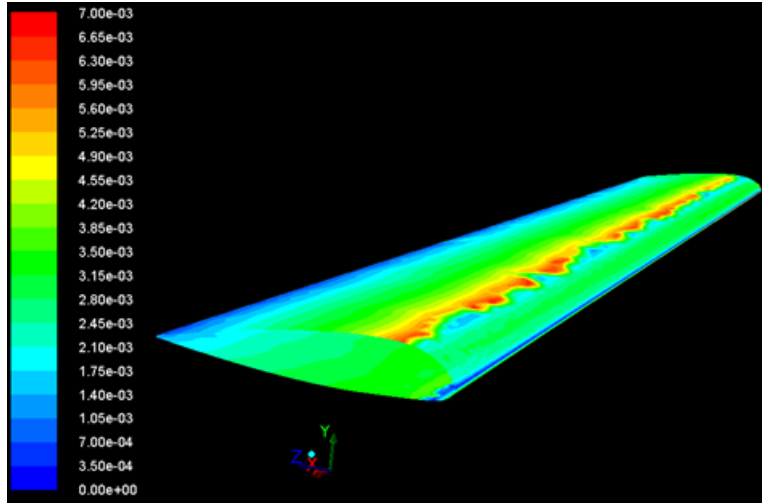


FIGURE 11.7. Skin friction over the surface of the TBM wing; $\text{aoa} = 0$ degrees; cruise conditions

The numerical values of C_d and C_l are in the Table 2

8. Discussion

The results of the CFD simulation on the wing shows that there is a big differences between 2D and 3D flows. To show how the presence of a small sweep can generate a velocity gradient in the span direction and influence

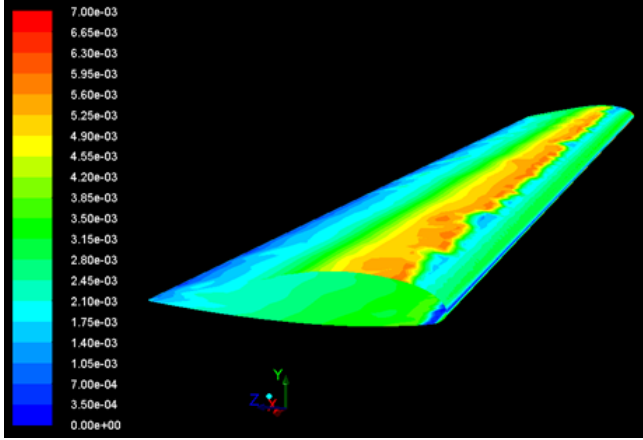


FIGURE 11.8. Skin friction over the surface of the New wing; $\text{aoa} = 0$ degrees; cruise conditions

TABLE 2. Comparison of drag and lift coefficients between TBM and new wing.

Wing	Visc. drag	Press. drag	Total drag	Lift coeff
TBM	0.00273	0.00754	0.01027	0.1919
New	0.00279	0.00755	0.01035	0.1903

the boundary layer, we have looked at the shear stress at the wall. (Figure 11.9)

The presence of a not zero value stresses that the flow at the wall is forced also in the span direction. We can see also the high value of these stresses close to the tip profile, suggesting the presence of trailing vortex. This 3D effect generates crossflow instabilities that are absent in 2D dimension. To see the difference between 2D and 3D flow, we have plotted the C_p distribution of the root profile of the wing (Figure 11.10) and compared it with the C_p from the 2D optimization (Figure 11.11).

Figure 11.11 shows very different C_p distribution. In the 3D validation in fact, the C_p distribution on the root profile has a maximum value

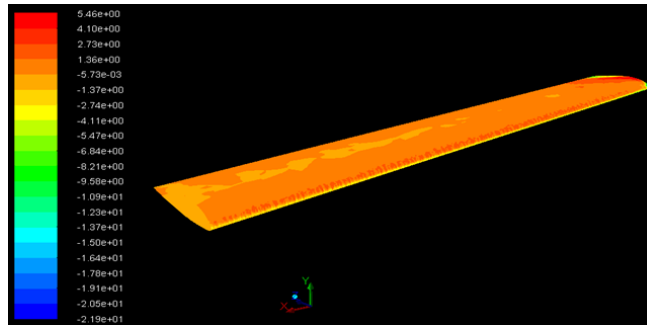


FIGURE 11.9. Shear stress along the span direction over the New wing.

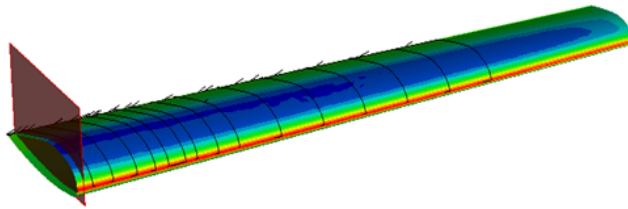


FIGURE 11.10. Root section of the New wing

slightly higher than the 2D, and the adverse pressure gradient starts more upstream.

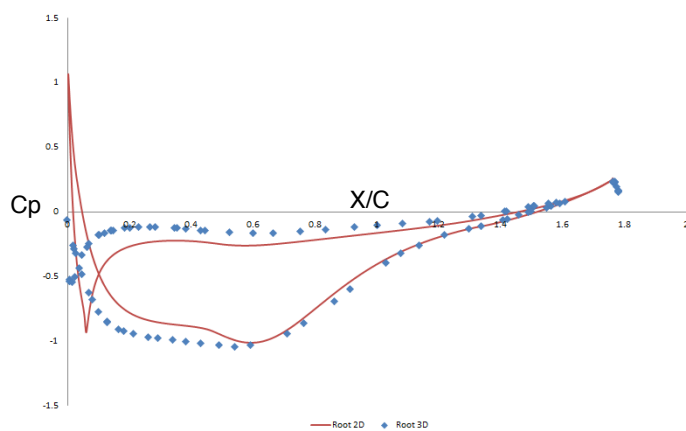


FIGURE 11.11. Comparison between the C_p distribution over the upper surface of the root profile in the 2D and 3D validation. Cruise condition. 0 degrees of α . Blue points: 3D; Red line: 2D.

CHAPTER 12

Conclusions and Future Works

1. Conclusions

An automatic shape optimization has been developed for an airfoil. The platform allows to change the geometry of an airfoil with the chord and the thickness at 25% and 75% of the chord fixed, to find an optimal shape able to delay the transition phenomenon and increase the max lift coefficient.

The process has been running for one and two flight conditions at the same time. The strategy used has showed a convergence for both of them:

- At cruise speed the results show good aerodynamic characteristics for the optimal shape, with an delay of the transition phenomenon from 26% to 47% of the curvilinear axis and with value of C_l and C_m almost unchanged.
- At low and high speed, the results have showed the constraints in finding a shape with low viscous drag at high speed and high max C_l at low speed. Therefore, the process proves that each flight condition requires different optimal shape and, an airfoil with high C_l max (1.66% higher) requires a different shape respect an airfoil with low value of viscous drag (transition from 26.4% to 44.8% of the c.a.)

The 3D validation has given unexpected results. The wing built with the optimal root and tip profiles has a higher value of the viscous drag than

that of the TBM 850. This result comes from the differences between 2D and 3D flows. In fact, shear stresses in the span direction suggests the presence of crossflow profiles that they add instabilities in the boundary layer.

2. Future Works

The crossflow instabilities can be investigated by NOLOT. Setting the sweep and considering an infinity span, NOLOT is able to study the effects of the crossflow disturbances on the stability of the laminar boundary layer. Besides, especially with the crossflow profiles, the evolution of disturbances is significantly affected by base-flow non-parallelism[2]. NOLOT can also consider these effects but the method requires more time and is less robust than the local method used in the optimization[10].

However, a non-local stability for a swept wing can be introduced in the optimization platform to optimize a profile with these effects.

For the 2D optimization, we have seen how the transition location is linked to the maximum thickness of the airfoil. For this reason, a profile with different constraints at the thickness can be analyzed to see the possible improvements in terms of transition. With different constraints, another parameterization can be tested to reduce the design parameters or to improve the changes of the shapes¹.

¹Reduce the risk to have unfeasible design

Appendices

These Appendices deal with a work performed at the University of Genoa regarding the study of the laminar boundary layer equations governing inviscid and incompressible flow in 2-dimension and in 2,5-dimension. The boundary layers on a flat plate and on an infinite swept wing are investigated with the bl3D code using the Boundary-Layer equations. This code, starting from a pressure or velocity distributions, allows to calculate the most important parameters of the boundary layer like thickness, shape factor, velocity and pressure distribution with their gradients. Different cases have been investigated considering three different external flow: Blasius, considering a constant velocity for the oncoming flow (or pressure, according with Bernoulli's equation for potential flow); accelerated flow with a negative pressure gradient and decelerated flow with an adverse pressure gradient. The influence of the pressure gradient on the separation has been investigated on a flat plate and on an infinite swept wing.

After the validation of the bl3D code, a code called Nolot was used based on the linear stability analysis with the semi-empirical e^N method to find out the transition of the boundary layer. This analysis considers small infinitesimally perturbations inside the boundary layer and it studies their spatial growth rate. The transition occurs when the integration of the growth rate, starting from the neutral stability point, arrives at value of 8, according with the Macks law. The integration of the growth rate is the amplification factor also called N factor. The code Nolot, developed by Hanifi, Hennigson, Hein, Bertolotti and Simen in September 1993, is validated for local and non-local stability.

APPENDIX A

Linear boundary layer 2 D

1. Prandtl's Boundary Layer Equations

Considering a two-dimensional incompressible and steady flow along a semi-infinite flat plate, we can write the Navier-Stokes equations:

$$(5) \quad \frac{\partial \bar{u}}{\partial t} + (\bar{u} \cdot \nabla) u = -\frac{\nabla p}{\rho} + \nu \nabla^2 \bar{u}$$

$$(6) \quad \nabla \cdot \bar{u} = 0$$

The wall is assumed to be flat and coinciding with the x -direction while the y -axis is perpendicular to it. With the exception of the immediate neighborhood of the surface, the velocities are of the order of the free-stream velocity, U , and the pattern of streamlines and the velocity distribution deviate only slightly from those in frictionless (potential) flow. From the reality we have that the fluid does not slide over the wall, but adheres to it. The transition from zero velocity at the wall to the full magnitude at some distance from it takes place in a very thin layer, the so-called **boundary – layer**. Very near the wall the velocity gradient normal to it, $\frac{\partial \mathbf{u}}{\partial y}$, is very large. In this region the very small viscosity ν of the fluid exerts an essential influence. The convection forces and the friction forces must have the same order of magnitude in this region, hence

$$(7) \quad \frac{\rho U^2}{L} \approx \frac{\mu U}{\delta^2}$$

From this equality we obtain that:

$$(8) \quad \delta^2 = \frac{\nu L}{U}$$

In the remaining region the viscosity is unimportant and the flow is frictionless and potential. The first approximation is that for the condition of steady flow the $\frac{\partial \mathbf{u}}{\partial t} = 0$. We can assume that $x \sim L$ and $y \sim \delta$ and $u \sim U$. For the partial derivatives we have $\frac{\partial}{\partial x} = \frac{1}{L}$ while $\frac{\partial}{\partial y}$ which we expect to be very large ($\gg 1$).

The Navier-Stokes are then simplified by considering that the thickness of the boundary layer, δ , is very small compared with the dimension, L , of the wall ($\delta \ll L$). We don't know anything about the order of magnitude of v but, from the equation of continuity, we get that $\frac{\partial \mathbf{u}}{\partial x}$ and $\frac{\partial \mathbf{v}}{\partial y}$ must have the same order of magnitude. About the previous consideration we have $\frac{\partial \mathbf{u}}{\partial x} \sim \frac{U}{L}$ and $\frac{\partial \mathbf{v}}{\partial y} \sim \frac{v}{\delta}$ and hence the v in the boundary layer is of the order $\frac{U\delta}{L}$. For the pressure we can consider that its order of magnitude is the order which allows the other quantities depend on ρU^2 . Now we can write the equations of Navier-Stokes under an order magnitude form:

$$(9) \quad \begin{aligned} \frac{U^2}{L} + \frac{U^2}{L} &= \frac{U^2}{L} + \nu \left(\frac{U^2}{L} + \frac{U^2}{\delta^2} \right) \\ \frac{U^2 \delta}{L^2} + \frac{U^2 \delta}{L^2} &= \frac{U^2}{\delta} + \nu \left(\frac{U \delta}{L^3} + \frac{U}{L \delta} \right) \\ \frac{U}{L} + \frac{U}{L} &= 0 \end{aligned}$$

Estimating the order of magnitude of each term we can have a simplification of the equations. Looking at the first equation $\frac{\partial u^2}{\partial x^2}$ is neglected with respect to $\frac{\partial u^2}{\partial y^2}$ because $\delta \ll L$. From the expression of δ^2 we have that the order of the term $\nu \left(\frac{\partial u^2}{\partial y^2} \right)$ is $\frac{U^2}{L}$. For the second equation we have that all the terms except the pressure, have the order of magnitude $\frac{U^2 \delta}{L^2}$. Making a comparison between the orders of magnitude of pressure and other terms we obtain:

$$(10) \quad \frac{U^2}{\delta} \frac{L^2}{U^2 \delta} = \left(\frac{L}{\delta}\right)^2$$

Since $\delta \ll L$ we can neglect all the terms of this equation with respect to the pressure:

$$(11) \quad \frac{\partial p}{\partial y} = 0$$

Considering these approximations and writing the Navier-Stokes equations referring to the dimensionless terms :

$$(12) \quad \dot{x} = \frac{x}{L} \dot{y} = \frac{y}{\delta} \dot{u} = \frac{u}{U} \dot{p} = \frac{p}{\rho U^2}$$

We obtain:

$$(13) \quad \begin{aligned} u \frac{\partial u}{\partial x} + v \frac{\partial u}{\partial y} &= -\frac{\partial p}{\partial x} + \frac{1}{Re} \left(\frac{\partial^2 u}{\partial y^2} \right) \\ \frac{\partial p}{\partial y} &= 0 \\ \frac{\partial u}{\partial x} + \frac{\partial v}{\partial y} &= 0 \end{aligned}$$

Re is the number of Reynolds which is assumed very large and it is equal to:

$$(14) \quad Re = \frac{UL}{\nu}$$

Now we have the important equation to determinate the thickness of the boundary layer

$$(15) \quad \frac{\delta}{L} \sim \frac{1}{\sqrt{Re}}$$

The boundary conditions are: absence of slip between the fluid and the wall $u = v = 0$ per $y = 0$ and $u = U$ per $y \rightarrow \infty$. Away from the boundary layer, the parallel component u becomes equal to the free-stream velocity U . So the viscous terms vanish for large values of R_e , and consequently, for the outer flow we obtain:

$$(16) \quad U \frac{\partial U}{\partial x} = - \frac{\partial p}{\partial x}$$

We can see that the pressure depends only on x . This suggests that the flow is accelerated by a pressure gradient.

2. Falkner-Skan

To study the laminar boundary layer we can consider a more simple method used by Falkner-Skan. They introduce the expression of the stream-function defined by:

$$(17) \quad u = \frac{\partial \Psi}{\partial y}$$

$$(18) \quad v = - \frac{\partial \Psi}{\partial x}$$

The function $\Psi(x, y)$ satisfy the continuity equation, hence we can write the Prandtl's boundary equation like only one equation:

$$(19) \quad \Psi_y \Psi_{yx} - \Psi_x \Psi_{yy} = - \frac{U dU}{dx} + \nu \Psi_{yyy}$$

with the boundary conditions $\frac{\partial \Psi}{\partial x} = \frac{\partial \Psi}{\partial y} = 0$ at the wall ($y = 0$) and $\frac{\partial \Psi}{\partial y} = U(x)$ for $y \rightarrow \infty$. The important feature of this study is based on the similarity solutions of the boundary layer equations. We shall define here similarity solution as those for which the component $u(x, y)$ of the velocity doesn't depend on x and y but only on a dimensionless function $\eta = \frac{y}{G(x)}$ that is a combination of the two coordinate where $G(x)$ is proportional to the boundary layer thickness $G(x) = \sqrt{\frac{x\nu}{U(x)}}$. The quest for

similarity solutions is particularly important with respect to the mathematical character of the solution. In cases where similarity solutions exist, it is possible, as we shall see in more detail later, to reduce the system of partial differential equations to one involving ordinary differential equations, which, evidently, constitutes a considerable mathematical simplification of the problem. Now introducing the *similarity transformation* η , we will obtain an ordinary differential equation for the stream function $f(\eta)$, instead of the original partial differential equation. The relation between $f(\eta)$ and $\Psi(x, y)$ is: $\Psi(x, y) = U(x)G(x)f(\eta)$. Now we can define the expression for $\Psi_i = \frac{\partial \Psi}{\partial i}$ and introduce them in the equation of the boundary layer:

$$(20) \quad \frac{\partial \eta}{\partial x} = \frac{\partial}{\partial x} \left(\frac{y}{G(x)} \right) = -G^I(x) \frac{y}{G(x)^2} = -\frac{G^I(x)}{G(x)} \eta$$

$$(21) \quad \frac{\partial \eta}{\partial y} = \frac{\partial}{\partial y} \left(\frac{y}{G(x)} \right) = \frac{1}{G(x)}$$

$$(22) \quad u = \frac{\partial \Psi}{\partial y} = \frac{\partial \Psi}{\partial \eta} \frac{\partial \eta}{\partial y} = U(x)f^I(\eta)$$

$$(23) \quad v = -\frac{\partial \Psi}{\partial x} = -\frac{\partial}{\partial x} U(x)G(x)f(\eta)$$

$$(24) \quad \Psi_{yx} = U^I(x)f^I(\eta) - \frac{U(x)G^I(x)}{G(x)}f^{II}(\eta)\eta$$

$$(25) \quad \Psi_{yy} = \frac{\partial}{\partial y} (U(x)f^I(\eta)) = f^{II}(\eta) \frac{U(x)}{G(x)}$$

$$(26) \quad \Psi_{yyy} = \frac{\partial}{\partial y} \Psi_{yy} = f^{III}(\eta) \frac{U(x)}{G(x)^2}$$

After introducing them in the boundary layer we obtain:

$$(27) \quad -U(x)U^I(x) + \nu f^{III}(\eta) \frac{U(x)}{G(x)^2}$$

$$(28) \quad f^{III}(\eta) + \frac{G(x)(U(x)G(x))^I}{\nu} f(\eta) f^{II}(\eta) + \frac{G(x)^I U^I(x)}{\nu} (1 - f^I(\eta))^2 = 0$$

$$(29) \quad \alpha = \frac{G(x)(U(x)G(x))^I}{\nu}$$

$$(30) \quad \beta = \frac{G(x)^I U^I(x)}{\nu}$$

Similarity solutions exist only when α and β do not depend on x and hence they must be constant. Replacing the values for $U(x)$ and $G(x)$ like below:

$$(31) \quad G(x) = \sqrt{\frac{x\nu}{U(x)}}$$

$$(32) \quad U(x) = cx^m$$

we obtain:

$$(33) \quad \alpha = \frac{m+1}{2}$$

$$(34) \quad \beta = m$$

and the similar equation which governs the velocity profile in the boundary layer became:

$$(35) \quad f^{III}(\eta) + \frac{m+1}{2} f(\eta) f^{II}(\eta) + m(1 - f^I(\eta))^2 = 0$$

with the boundary conditions for $\eta = 0$, $u = 0$ and we have $f^I(\eta) = 0$. For $v = 0$ we have $f(\eta) = 0$ while for $\eta \rightarrow \infty$, $u = U(x)$ and $f^I(\eta) = 1$. The equation found by Blasius is a particular case of this study because he considered $U(x) = cost$. We can obtain his equation from the equation of Falkner-Skan $m = 0$:

$$(36) \quad f^{III}(\eta) + \frac{1}{2}f(\eta)f^{II}(\eta) = 0$$

The coefficient m is representative of an acceleration of the flow. In fact if we consider $m > 0$ we have an acceleration of the flow and considering the Bernoulli's equation we have a negative pressure gradient leading to a boundary layer, which remains more attached to the wall. On the other hand with a negative value of m we have a positive (adverse) pressure gradient that decelerates the flow and potentially leads to separation. We can see it with the graphs of the thickness, shape factor and also of the velocity v in the boundary layer for three different value of m . In fact, although very near the stagnation point the velocity v is positive for each m , then for $m > 0$ the boundary layer remains more attached the wall, while not in the others case. (Figure A.1)

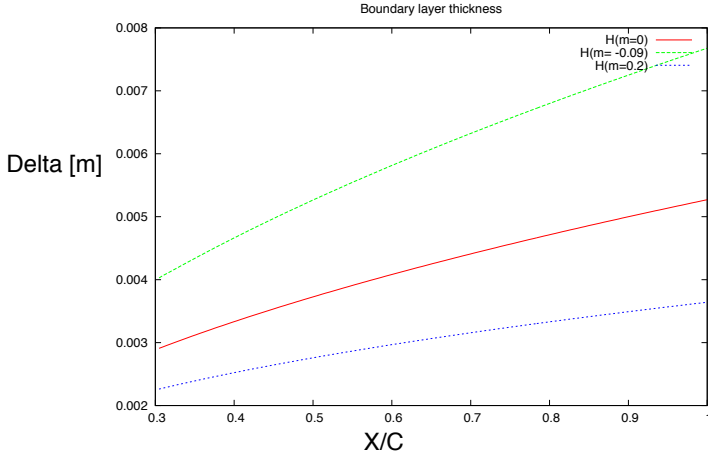


FIGURE A.1. Boundary layer thickness distribution on a flat plate for incompressible and steady flow. The blue line is for acceleration of the external flow; the green line is for a deceleration; the red line is relative to a constant flow.

We can see the dependence of the acceleration from the value of m in the Figure A.4.

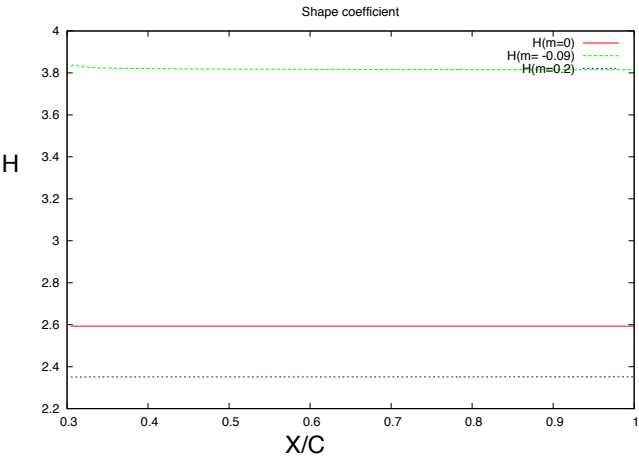


FIGURE A.2. Shape factor distribution on a flat plate for three different acceleration of the flow: positive (blue); negative (green); constant (red)

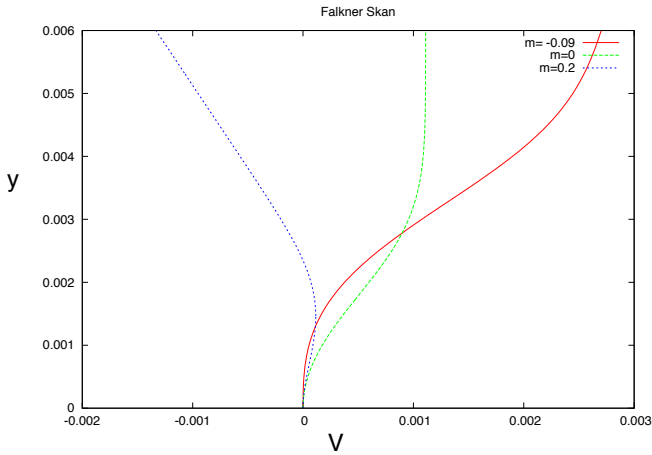


FIGURE A.3. Distribution of the normal velocity at the wall , v , in the boundary layer for a flat plate. Deceleration external flow (red); constant external flow (green); acceleration external flow (blue)

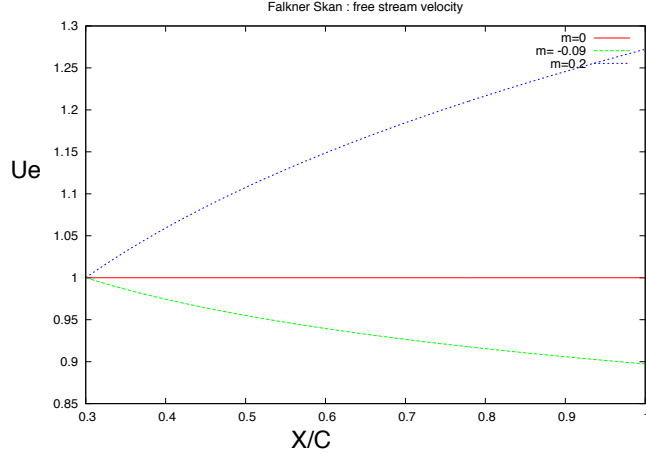


FIGURE A.4. Velocity distribution of the main flow $U_e = x^m$. Acceleration flow (blue); Decelerated flow (green); Constant flow (red).

We have made the study for a flat plate with three different value of m . We must remember that when we made the simplifications introduced into the Navier-Stokes's equations it was assumed that the thickness is very small compared with a still unspecified line dimension. It means that very near at the stagnation point δ is very similar to the value of the x -component and the Prandtl's equations are not valid. This is the fact that let us to take the first point to study the equation $x = 0.3$. $m = 0$ is the case of Blasius and the velocity U_e is constant. For $m > 0$ we have decided to take 0.2 and we can see the growth of the velocity. For $m < 0$ we have taken the value -0.09 that is a limit value for m as we explain after. In the case of decelerated flow they exhibit a point of inflexion for the velocity distribution. Separation occurs for $m = -0.09$. As we said before, when a region with an adverse pressure gradient exist along the wall, the retarded fluid particles can't, in general, penetrate too far into the region of increased pressure owing to their small kinetic energy. Thus the boundary layer is deflected sideways from the wall, separated from it,

and moves into the main stream. In general the fluid particles behind the point of separation follow the pressure gradient and move in a direction opposite to the external stream. The point of separation is defined as the limit between forward and reverse flow in the layer in the immediate neighborhood of the wall, or

$$(37) \quad \frac{\partial u}{\partial y}_{y=0} = 0$$

Trying different values for m we have found the point of inflection for $m = -0.091$ which agrees with the results of the literature. This result shows that the laminar boundary layer is able to support only a very small deceleration without separation occurring.

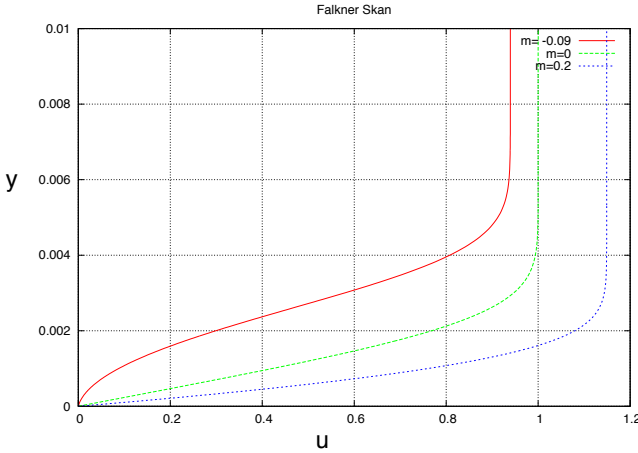


FIGURE A.5. Distribution of the streamwise velocity in the boundary layer for three different pressure gradient: negative (red); positive (blue); zero (green).

To see better the difference of the u profiles in the y direction for different values of m , we have plotted, in Figure A.7, the distribution of

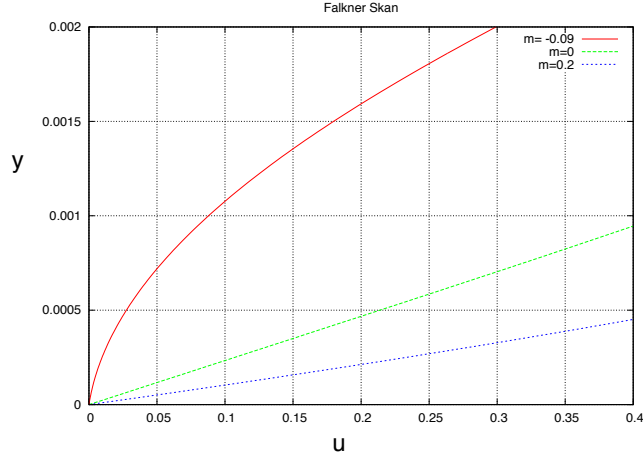


FIGURE A.6. Distribution of the normal velocity at the wall in the boundary layer for three different pressure gradient: negative (red); positive (blue); zero (green).

$$(38) \quad \frac{\partial u}{\partial y}$$

where it is worth noticing, for example, that for $m > 0$ we have the bigger variation of u near to the wall, and not for $m < 0$.

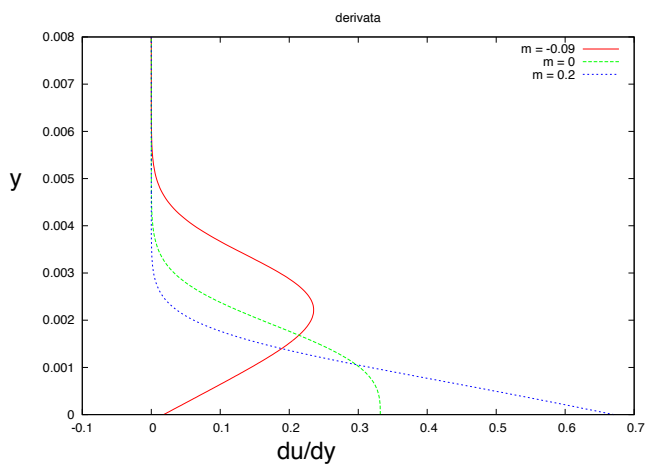


FIGURE A.7. Distribution of the derivate of the streamwise velocity in the boundary layer for three different pressure gradient: positive (blue); zero (green); negative (red).

APPENDIX B

Linear boundary layer 2,5 D

1. Prandtl's Boundary Layer Equations

In the case of a three-dimensional boundary layer the external potential flow depends on two coordinates at the wall surface (x, z) and the flow within the boundary layer possesses all three velocity components which, moreover, depend on all three space coordinates in the general case. An important case of a three-dimensional boundary layer is that of an aircraft's wing, whose leading edge is not perpendicular to the stream. For the purpose of establishing the boundary layer equations we shall confine ourselves to the simplest case of a plane wall. x and z denote the coordinates at the wall surface, y denoting the coordinate which is perpendicular to the wall as we can see in Figure B.1:

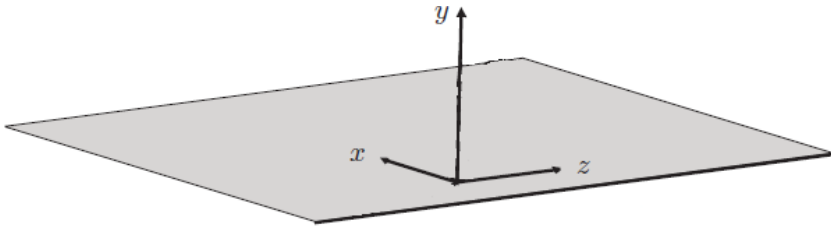


FIGURE B.1. Reference axis x, y, z .

The velocity vector is assumed to have the component $U(x, z)$ and $W(x, z)$. As we had seen in the two-dimensional study, for the frictional terms of the equations for the x and z directions, it is possible to neglect the derivatives with respect to the coordinates which are parallel to the wall compared to

the derivative with respect to the coordinate y . Regarding the equation in the y direction we again obtain the result that $\frac{\partial p}{\partial y}$ is equal to zero. So the pressure has seen to depend on x and z alone and is imposed on the boundary layer by the potential flow.

$$\begin{aligned}
 u \frac{\partial u}{\partial x} + v \frac{\partial u}{\partial y} + w \frac{\partial u}{\partial z} &= -\frac{\partial p}{\partial x} + \frac{1}{Re} \left(\frac{\partial^2 u}{\partial y^2} \right) \\
 \frac{\partial p}{\partial y} &= 0 \\
 u \frac{\partial w}{\partial x} + v \frac{\partial w}{\partial y} + w \frac{\partial w}{\partial z} &= -\frac{\partial p}{\partial z} + \frac{1}{Re} \left(\frac{\partial^2 w}{\partial y^2} \right) \\
 \frac{\partial u}{\partial x} + \frac{\partial v}{\partial y} + \frac{\partial w}{\partial z} &= 0
 \end{aligned}
 \tag{39}$$

The boundary conditions are $u = v = w = 0$ for $y = 0$ and $u = U$, $w = W$ for $y \rightarrow \infty$. We can see that for $w = W = 0$ the system is the same as the system of equations for the two-dimensional boundary layer flow. Until now, no exact solution for this system of the equations for the three-dimensional boundary layer is found, so a particular case for it is that the potential flow depends on x but not on z : $U = U(x)$, $W = W(x)$. We consider an aircraft's wing with infinity length in the z -coordinate. For this simplification the system is written:

$$\begin{aligned}
 \frac{\partial u}{\partial x} + \frac{\partial v}{\partial y} &= 0 \\
 u \frac{\partial u}{\partial x} + v \frac{\partial u}{\partial y} &= -\frac{\partial p}{\partial x} + \frac{1}{Re} \left(\frac{\partial^2 u}{\partial y^2} \right) \\
 \frac{\partial p}{\partial y} &= 0 \\
 u \frac{\partial w}{\partial x} + v \frac{\partial w}{\partial y} &= \frac{1}{Re} \left(\frac{\partial^2 w}{\partial y^2} \right)
 \end{aligned}
 \tag{40}$$

2. Falkner-Skan-Cooke

Like we had seen for the two-dimensional boundary layer equations, we can study the three-dimensional boundary layer equations considering a similarity function. We shall consider the same stream function $\Psi(x, y)$ and the dimensionless similar stream function $f(\eta)$. Looking at the system we see that we have the same system of Falkner-Skan with a new equation that we will call *Cooke Equation* :

$$(41) \quad u \frac{\partial w}{\partial x} + v \frac{\partial w}{\partial y} = \nu \left(\frac{\partial^2 w}{\partial y^2} \right)$$

With the first three equations we obtain the solution of Falkner-Skan. Considering the equation in the z -direction we introduce relation between w and a similar function which we call $g(\eta)$. $w = Wg(\eta)$ where W is a constant and η is the similarity transformation $\frac{y}{G(x)}$. In order to introduce the similarity relation in the equation finding the similar function for the velocity profile we must deduce the derivatives:

$$(42) \quad \begin{aligned} \frac{\partial w}{\partial x} &= W \frac{\partial}{\partial \eta} g(\eta) \frac{\partial \eta}{\partial x} = - \frac{W G^I(x)}{G(x)} \eta g^I(\eta) \\ \frac{\partial w}{\partial y} &= W \frac{\partial}{\partial \eta} g(\eta) \frac{\partial \eta}{\partial y} = - \frac{W g^I(x)}{G(x)} \\ \frac{\partial^2 w}{\partial y^2} &= \frac{\partial}{\partial y} \left(\frac{W g^I(x)}{G(x)} \right) = \frac{W g^{II}(x)}{G(x)^2} \end{aligned}$$

After introducing (42) in the (41) we obtain:

$$(43) \quad g^{II}(\eta) + \alpha f(\eta) g^I(\eta) = 0$$

with the boundary conditions for $\eta = 0$, $w = 0$ we have $g(\eta) = 0$ and for $\eta \rightarrow \infty$, $w = W$ we obtain $g(\eta) = 1$. Considering the Falkner-Skan solution with the Cooke solution we obtain the velocity field of the three-dimensional boundary layer:

$$(44) \quad u = U(x)f^I(\eta)$$

$$(45) \quad v = U(x)G^I(x)f^I(\eta)\eta - (U(x)G(x))^I f(\eta)$$

$$(46) \quad w = Wg(\eta)$$

With this equation we can study the dynamic of the flow on a yawed wing with infinity length in z-direction. In this case we'll use only $m < 0$ and $m > 0$ because for $m = 0$ the solution would be equal to the case without sweep. In fact, for $U(x) = cost$ the fact that the plate is yawed has seen to have no influence on the formation of the boundary layer. The velocity $U(x) = x^m$ while $W(x) = W_\infty = cost$ as we can see from the Figures B.2 and B.3.

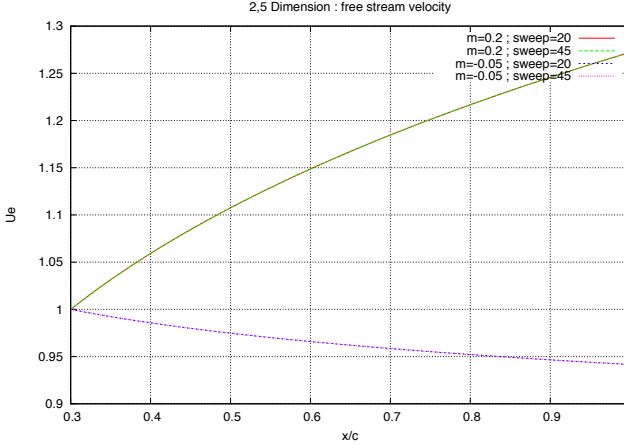


FIGURE B.2. Distribution of the external streamwise velocity on a flat plate. 2 different angle of sweep. Red and green for negative pressure gradient; blue and purple for positive pressure gradient.

We have decided to take $m = 0.2$ and $m = -0.05$ and for these two cases we have obtained the Figures B.4 - B.7. In the code bl3D used to make the calculation of the boundary layer, the reference system has been taken

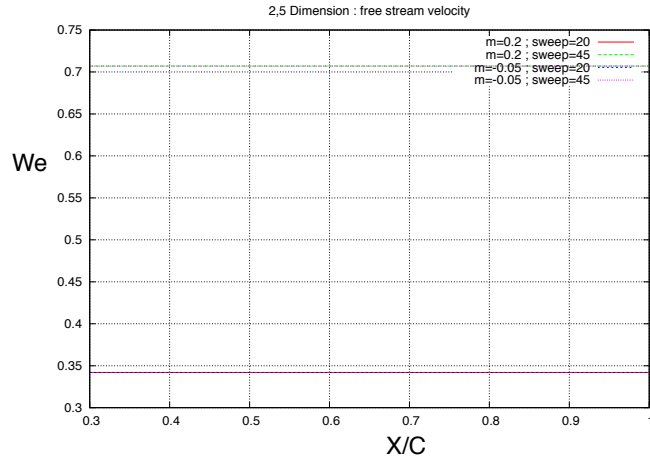


FIGURE B.3. Distribution of the external spanwise velocity on a flat plate. 2 different angle of sweep. Red and green for negative pressure gradient; blue and purple for positive pressure gradient.

following the streamline very near at the wall and not along the streamline of potential flow.

As the Figures B.4 - B.7 show, increasing the sweep of the wing reduces the boundary layer thickness at the same conditions (same distribution of external flow).

B. LINEAR BOUNDARY LAYER 2,5 D

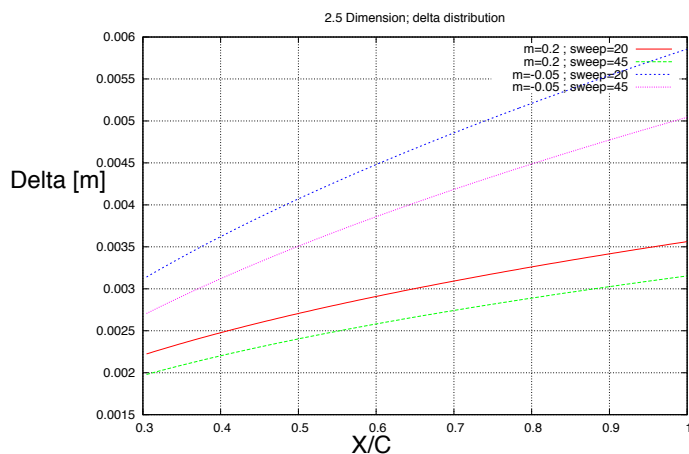


FIGURE B.4. Distribution of the boundary layer thickness on a flat plate. 2 different angle of sweep. Red and green for negative pressure gradient; blue and purple for positive pressure gradient.

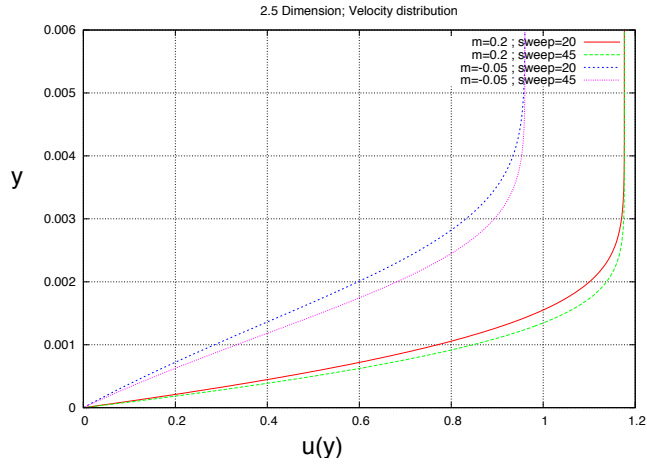


FIGURE B.5. Streamwise velocity distribution in the boundary layer on a flat plate. 2 different angle of sweep. Red and green for negative pressure gradient; blue and purple for positive pressure gradient.

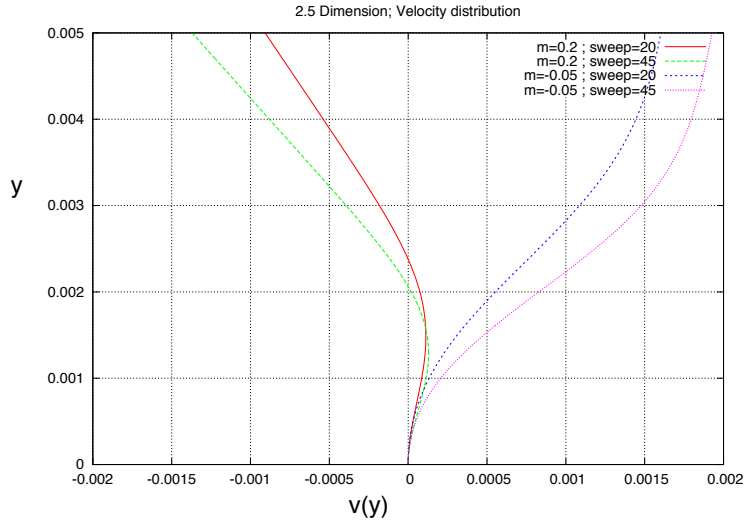


FIGURE B.6. Normal velocity distribution in the boundary layer.

B. LINEAR BOUNDARY LAYER 2,5 D

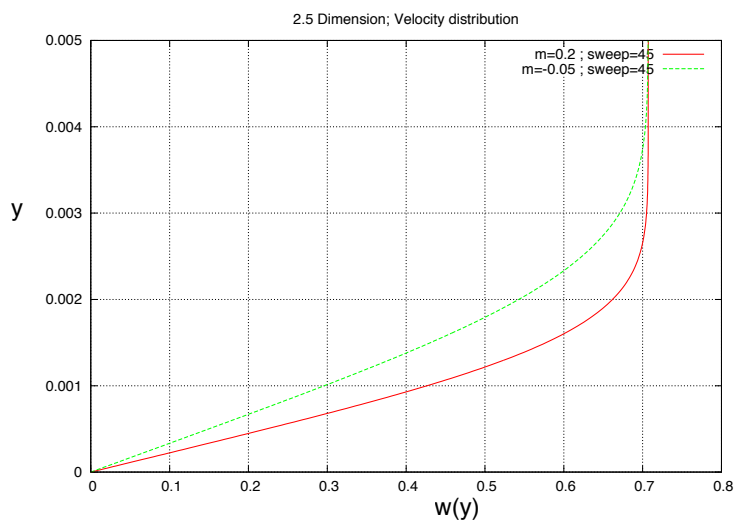


FIGURE B.7. Spanwise velocity distribution in the boundary layer.

APPENDIX C

Thickness of the boundary layer

1. Displacement and Momentum thickness

A first approximation of the thickness of the boundary layer is consider that for a fixed x , the end of the boundary layer in the perpendicular direction respect with the flow, is at the point we have $u = 99\%U$ where U is the velocity of the potential flow. Now we can consider better estimations of the boundary-layer thickness by evaluating the quantity like mass and momentum flux which through the boundary layer.

Displacement thickness:

This expression of the thickness is sometimes used and indicates the distance by which the external streamlines are shifted owing to the formation of the boundary layer. To determine this equation we can consider the equality between two streamlines:

$$\begin{aligned} (47) \quad \int_0^h U(x)dy &= \int_0^{h+\delta} u(x,y)dy^1 \\ &= \int_0^h u(x,y)dy + \int_h^{h+\delta} u(x,y)dy \\ &= {}^2 \int_0^h u(x,y)dy + U(x)\delta_1(x,h) \end{aligned}$$

we have that:

$$U(x)\delta_1(x,h) = \int_0^h (U(x) - u(x,y))dy$$

and:

$$\begin{aligned}
 \delta_1(x, h) &= \int_0^h \left(1 - \frac{u(x, y)}{U(x)}\right) dy \\
 (48) \qquad &= \int_0^\infty \left(1 - \frac{u(x, y)}{U(x)}\right) dy
 \end{aligned}$$

3

Momentum thickness:

Now we shall consider the momentum flux through the boundary layer. Comparing the inviscid flow with the viscous flow, we obtain that in the second case there is a loss of the momentum which we can write:

$$\begin{aligned}
 \Delta Q_M &= \\
 &= \rho \int_0^\infty (U^2(x) - u^2(x, y)) dy \\
 &= \rho \int_0^\infty [(U(x) + u(x, y))(U(x) - u(x, y))] dy \\
 &= \rho \int_0^\infty U(x)(U(x) - u(x, y)) dy + \rho \int_0^\infty u(x, y)(U(x) - u(x, y)) dy \\
 (49) \quad &= \rho U^2(x) \delta_1(x) + \rho U^2(x) \int_0^\infty \frac{u(x, y)}{U(x)} \left(1 - \frac{u(x, y)}{U(x)}\right) dy
 \end{aligned}$$

We can consider the subject of the integral as a correction for the first term. Hence we shall introduce another expression for the thickness of the boundary layer:

$$(50) \qquad \delta_2(x) = \int_0^\infty \frac{u(x, y)}{U(x)} \left(1 - \frac{u(x, y)}{U(x)}\right) dy$$

It is worth saying that $\delta_2(x)$ it is not a thickness of the boundary layer but it is a correction to make for the displacement thickness. In the figure below we can see the distribution of the three thickness on a flat plate.

³for $h \rightarrow \infty$

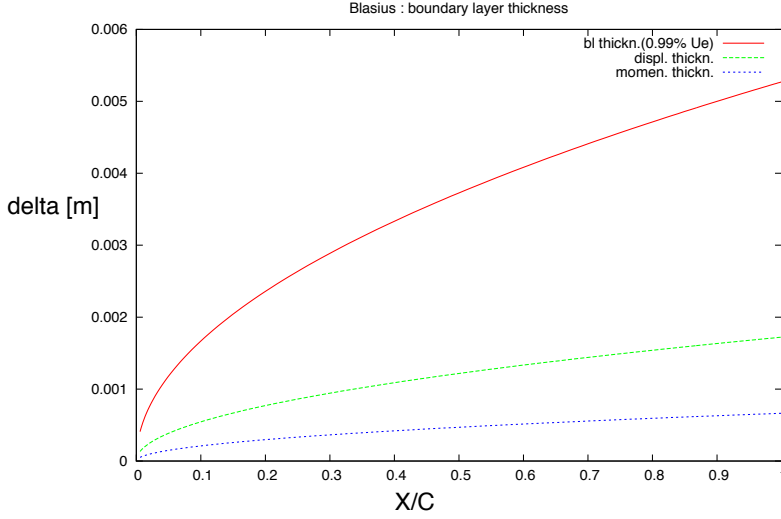


FIGURE C.1. Distribution of the three boundary layer thickness on a flat plate as a function of the streamwise coordinate. Two-dimensional, steady and incompressible flow.

2. Von Karman's integral equation

Looking at the Prandtl's equation we can obtain an equation which governs the boundary layer thickness in the flow. We shall consider the two-dimensional, incompressible, steady flow. We focus on a fixed x and we integrate the Prandtl's equation on the y -direction:

$$(51) \quad \int_0^\infty \left[u \frac{\partial u}{\partial x} + v \frac{\partial u}{\partial y} + \frac{\partial p}{\partial x} - \nu \left(\frac{\partial^2 u}{\partial y^2} \right) \right] dy = 0$$

From the third equation of (13) we have:

$$v = - \int_0^y \frac{\partial u}{\partial x} dy$$

One of the terms of the momentum equation in the x -direction is:

$$\begin{aligned}
\int_0^\infty v \frac{\partial u}{\partial y} dy &= - \int_0^\infty \left[\int_0^y \frac{\partial u}{\partial x} dy \right] \frac{\partial u}{\partial y} dy \\
&= -u \left[\int_0^y \frac{\partial u}{\partial x} dy \right]_0^\infty + \int_0^\infty u \frac{\partial u}{\partial x} dy \\
(52) \qquad &= -U(x) \int_0^\infty \frac{\partial u}{\partial x} dy + \int_0^\infty u \frac{\partial u}{\partial x} dy
\end{aligned}$$

Now we can introduce the shear stress at the wall $\tau = -\mu \frac{\partial u}{\partial y}$. Hence:

$$- \int_0^\infty \nu \left(\frac{\partial^2 u}{\partial y^2} \right) dy = \frac{\tau(x)}{\rho}$$

Replacing these expression in the momentum equation we obtain:

$$\begin{aligned}
\frac{\tau(x)}{\rho} &= - \int_0^\infty \left[2u \frac{\partial u}{\partial x} - U(x) \frac{\partial u}{\partial x} - U(x) \frac{dU(x)}{dx} \right] dy \\
\frac{\tau(x)}{\rho} &= - \int_0^\infty \left[\frac{\partial u^2}{\partial x} - U(x) \frac{\partial u}{\partial x} - u \frac{\partial U(x)}{\partial x} + u \frac{\partial U(x)}{\partial x} - U(x) \frac{dU(x)}{dx} \right] dy \\
\frac{\tau(x)}{\rho} &= - \int_0^\infty \left[\frac{\partial u^2}{\partial x} - \frac{\partial}{\partial x} (U(x)u) + u \frac{\partial U(x)}{\partial x} - U(x) \frac{dU(x)}{dx} \right] dy \\
\frac{\tau(x)}{\rho} &= \int_0^\infty \left[\frac{\partial}{\partial x} ((U(x) - u)u) + \frac{\partial U(x)}{\partial x} (U(x) - u) \right] dy \\
\frac{\tau(x)}{U^2(x)\rho} &= \frac{1}{U^2(x)} \frac{d}{dx} \int_0^\infty u(U(x) - u) dy + \frac{1}{U^2(x)} \int_0^\infty \frac{\partial U(x)}{\partial x} (U(x) - u) dy \\
(53)
\end{aligned}$$

Now, we define:

$$\begin{aligned}
\frac{\tau(x)}{U^2(x)\rho} &= \frac{C_f(x)}{2} \\
\int_0^\infty \frac{u}{U(x)} \left(1 - \frac{u}{U(x)}\right) dy &= \delta_2(x) \\
\frac{\partial U(x)}{\partial x} &= U^I \\
\int_0^\infty \left(1 - \frac{u}{U(x)}\right) dy &= \delta_1(x)
\end{aligned}$$

and obtain:

$$(54) \quad \frac{d}{dx} \delta_2(x) + \frac{U^I(x)}{U(x)} (2 + H_{1,2}) \delta_2(x) = \frac{C_f(x)}{2}$$

Where $H_{1,2}$ is a *shape coefficient* and $C_f(x)$ is a *drag coefficient*. This equation is known as the momentum-integral equation of boundary-layer theory, or as Von Karman's integral equation. It is often used in the approximate methods for the solutions of the boundary layer equation.

APPENDIX D

Linear stability theory of laminar boundary layers

1. Orr Sommerfeld and Squire equations

Linear stability theory concerns the evolution of perturbations with infinitesimal amplitude superimposed on a laminar flow. The flow is decomposed in mean flow and non-steady disturbance. The goal is to determine if the disturbances amplify or not. If the disturbances decay with time, the flow is considered stable; on the other hand, if the disturbances are amplified with time, the flow is considered unstable. An important object of this theory is to evaluate the critical Reynolds number for which the flow become unstable. We describe the velocity components of the mean flow as U, V, W and its pressure P . The corresponding quantities for the non-steady disturbance will be denoted by u^I, v^I, w^I, p^I . So, the resultant quantities will be:

$$\begin{aligned} u &= U + u^I \\ v &= V + v^I \\ w &= W + w^I \\ p &= P + p^I \end{aligned} \tag{55}$$

The magnitude of the disturbance is smaller than that of the mean flow and for this reason the method investigating the stability is called *method of the small disturbances*. We consider a three-dimensional flow and study the Navier-Stokes's equations seen previously.

$$\begin{aligned}
\frac{\partial u}{\partial t} + u \frac{\partial u}{\partial x} + v \frac{\partial u}{\partial y} + w \frac{\partial u}{\partial z} &= -\frac{\partial p}{\partial x} + \frac{1}{Re}(\nabla^2 u) \\
\frac{\partial v}{\partial t} + u \frac{\partial v}{\partial x} + v \frac{\partial v}{\partial y} + w \frac{\partial v}{\partial z} &= -\frac{\partial p}{\partial y} + \frac{1}{Re}(\nabla^2 v) \\
\frac{\partial w}{\partial t} + u \frac{\partial w}{\partial x} + v \frac{\partial w}{\partial y} + w \frac{\partial w}{\partial z} &= -\frac{\partial p}{\partial z} + \frac{1}{Re}(\nabla^2 w) \\
(56) \quad \frac{\partial u}{\partial x} + \frac{\partial v}{\partial y} + \frac{\partial w}{\partial z} &= 0
\end{aligned}$$

A first simplification is to consider the velocity components of the mean flow depending only on y and so $U = U(y)$ and $W = W(y)$. $V = 0$. It can be considered a good approximation because in the equations of the laminar boundary layer we had found that the dependence of the velocity U in the main flow on the x -coordinate was smaller than that on y . These flows are called parallel flows. As far as the pressure in the main flow is concerned, it is necessary to assume a dependence on x as well y and z , because the pressure gradient $\frac{\partial p}{\partial x}$ maintains the flow. $P = P(x, y, z)$. The three-dimensional disturbance is a function of the time and space:

$$\begin{aligned}
u^I &= u^I(x, y, z, t) \\
v^I &= v^I(x, y, z, t) \\
w^I &= w^I(x, y, z, t) \\
(57) \quad p^I &= p^I(x, y, z, t)
\end{aligned}$$

With the previously consideration and neglecting quadratic terms in the disturbance velocity component we obtain:

$$\begin{aligned}
\frac{\partial u^I}{\partial t} + U \frac{\partial u^I}{\partial x} + v^I \frac{\partial U}{\partial y} + W \frac{\partial u^I}{\partial z} &= -\frac{\partial p^I}{\partial x} + \frac{1}{R_e} (\nabla^2 u^I) \\
\frac{\partial v^I}{\partial t} + U \frac{\partial v^I}{\partial x} + W \frac{\partial v^I}{\partial z} &= -\frac{\partial p^I}{\partial y} + \frac{1}{R_e} (\nabla^2 v^I) \\
\frac{\partial w^I}{\partial t} + U \frac{\partial w^I}{\partial x} + v^I \frac{\partial W}{\partial y} + W \frac{\partial w^I}{\partial z} &= -\frac{\partial p^I}{\partial z} + \frac{1}{R_e} (\nabla^2 w^I) \\
(58) \quad \frac{\partial u^I}{\partial x} + \frac{\partial v^I}{\partial y} + \frac{\partial w^I}{\partial z} &= 0
\end{aligned}$$

Now we can consider the disturbance composed of a number of discrete partial fluctuations, each of which is said to consist of a wave which is propagated in the x -, z -direction. Hence, it is possible to introduce a stream function Ψ representing a single oscillation of the disturbance:

$$(59) \quad \Psi(x, y, z, t) = \Phi(y) e^{i(\alpha x + \beta z - \omega t)}$$

α and β are the wavelength number of the disturbance respectively on x - and z -directions. ω is the frequency of the oscillation. Now we can write the quantities of the disturbance as Ψ :¹

$$\begin{aligned}
u^I(x, y, z, t) &= \hat{u}(y) e^{i(\alpha x + \beta z - \omega t)} \\
\frac{\partial u^I}{\partial x} &= (i\alpha) \hat{u}(y) e^{i(\alpha x + \beta z - \omega t)} \\
\frac{\partial}{\partial y} U &= DU \\
\frac{\partial u^I}{\partial z} &= (i\beta) \hat{u}(y) e^{i(\alpha x + \beta z - \omega t)} \\
\frac{\partial u^I}{\partial t} &= (-i\omega) \hat{u}(y) e^{i(\alpha x + \beta z - \omega t)} \\
(60) \quad \nabla^2 u^I &= D^2 - K^2
\end{aligned}$$

¹ $K = \alpha^2 + \beta^2$

Introducing these terms in the system we obtain:

$$\begin{aligned}
 i(\alpha U + \beta W - \omega)\hat{u} + \hat{v}DU + i\alpha\hat{p} - \frac{\hat{u}}{R_e}(D^2 - K^2) &= 0 \\
 i(\alpha U + \beta W - \omega)\hat{v} + D\hat{p} - \frac{\hat{v}}{R_e}(D^2 - K^2) &= 0 \\
 i(\alpha U + \beta W - \omega)\hat{w} + \hat{v}DW + i\beta\hat{p} - \frac{\hat{w}}{R_e}(D^2 - K^2) &= 0 \\
 i\alpha\hat{u} + i\beta\hat{w}D\hat{v} &= 0
 \end{aligned}
 \tag{61}$$

After the elimination of the pressure we obtain an equation better known as the **Orr-Sommerfeld Equation** which governs the stability of nearly parallel viscous flow such as the boundary layer:

$$\hat{v}(D^2 - K^2)^2 - iR_e[(\alpha U + \beta W - \omega)(D^2 - K^2)\hat{v} - (\alpha D^2U + \beta D^2W)\hat{v}] = 0
 \tag{62}$$

The boundary conditions for this equation are: $\hat{v}(0) = D\hat{v}(0) = 0$ and $\hat{v} = 0$ for $y \rightarrow \infty$ where \hat{v} is the **normal velocity**. To determinate the total velocity vector it is necessary to derive the equation of **normal vorticity**. The vorticity is defined like $\vartheta = \partial_z u - \partial_x v$ which satisfies the equation:

$$\frac{\partial \vartheta}{\partial t} + U \frac{\partial \vartheta}{\partial x} - \frac{1}{R_e} \nabla^2 \vartheta = -DU \frac{\partial v^I}{\partial z}
 \tag{63}$$

As we made for the normal velocity, we can introduce an wavelike disturbance and we obtain:

$$[(-i\omega + i\alpha U) - \frac{1}{R_e}(D^2 - K^2)]\hat{\vartheta} = -i\beta DU\hat{v}
 \tag{64}$$

This equation is well-known **Squire Equation** and we can see that it depends on the normal velocity. A system of these equations allows us to know all the velocity components of the flow and determinate its stability. The system poses an eingvalue problem and it is important to say than there is no a general restriction to real or complex wave numbers or

frequencies. If we want study a temporal stability we must consider the frequency like a complex numbers ($\omega = \omega_r + i\omega_i$) while the wave numbers α and β are real. In this case to have stability it's necessary that $\omega_i < 0$ because $u = e^{\omega_i t} \hat{u}(y) e^{i(\alpha x + \beta z - \omega_r t)}$ and the growth rate is determinate by ω_i . On the other hand, if we want study a spatial stability we must consider the wave-numbers like a complex numbers ($\alpha = \alpha_r + i\alpha_i$ and $\beta = \beta_r + i\beta_i$) while the frequency ω is real. The stability will hold for the imaginary part of the wave-numbers, being positive. In our study we have analyzed a spatial stability considering ($\alpha = \alpha_r + i\alpha_i$) and β and ω real.

2. Parabolized Stability Equations (PSE)

Now we introduce a set of equations known as the Parabolized Stability Equations (PSE). Differently from the Orr-Sommerfel and Squire equations, these equations are used to study the spatial evolution of disturbances affected by baseflow nonparallelism, that are significant in crossflow-dominated boundary layer. The fundamental assumption of this theory is that the disturbances consist of a fast oscillatory part and an amplitude that varies slowly in the stream wise direction. This decomposition allows us to have equations amenable to a numerical marching procedure. At first we are going to consider the two-dimensional linear Navier-Stokes's equations. The disturbance decomposed like above is:

$$(65) \quad u(x, y, t) = \hat{u}(x, y) e^{i \int_{x_0}^x \alpha(\xi) d\xi - i\omega t}$$

where α is the complex stream wise wave number. Introducing this equation in the Navier Stokes equations, and neglecting all terms of order R_e^{-2} and higher, we arrive at the following system of equations written in matrix form:

$$\frac{d}{dx} = \begin{pmatrix} U \\ V \\ P \end{pmatrix} \begin{pmatrix} -i\alpha & -D & 0 \\ 0 & -\frac{C_1}{U} - \frac{V_y}{U} & -\frac{D}{U} \\ -C_1 + i\alpha U - U_x & UD - U_y & -i\alpha \end{pmatrix} \begin{pmatrix} U \\ V \\ P \end{pmatrix}$$

with

$$(66) \quad C_1 = i\alpha U - i\omega + VD - \frac{1}{R_e}(D^2 - \alpha^2)$$

where D denotes the derivate with respect to the normal direction y . The form of the solution (60) assumes an x -dependent amplitude function and an x -dependent stream wise wave number α , thus causing an ambiguity. To remove this ambiguity we impose an auxiliary condition on the amplitude function:

$$(67) \quad \int_{y_{min}}^{y_{max}} (\hat{u}^* \hat{u}_x + \hat{v}^* \hat{v}_x + \hat{p}^* \hat{p}_x) dy = 0$$

This relation imposes to the stream wise variation of the amplitude function to remain small and ensures that most of the x -variation of the disturbance will be accounted for by the exponential function. These approximation can be applied to more complicated flows like quasi three-dimensional flows. Now we consider the disturbance $q = (\hat{u}, \hat{v}, \hat{w}, \hat{p})$ decomposed in the following way:

$$(68) \quad q = \hat{q}(x, y) e^{i\Theta}$$

with

$$(69) \quad \Theta = \int_{x_0}^x \alpha(x') dx' + \beta z - \omega t$$

As before, neglecting all terms which are of the order R_e^{-2} and higher, leads to a quasi-parabolic equation system of the form:

$$(70) \quad A\hat{q} + B\frac{\partial\hat{q}}{\partial y} + C\frac{\partial^2\hat{q}}{\partial y^2} + \frac{\partial\hat{q}}{\partial x} = 0$$

where A,B,C and D are functions of α, β, ω , mean flow, and, in general, metric quantities. In this case, the ambiguity in the x-dependence of the amplitude function and the stream wise wave number is removed with the help of an auxiliary condition which takes on the form:

$$(71) \quad \int_0^\infty \hat{q}^H \frac{\partial}{\partial x} \hat{u} dy = 0$$

APPENDIX E

Stability analysis of laminar boundary layer

In this chapter we investigate the stability of three different models: a flat plate boundary layer, a swept flat plate boundary layer and the boundary layer on a infinite swept wing. To make this, we will use a stability code called NOLOT. NOLOT is a non-local stability code based on PSE (65) and it was developed by Hanifi, Henningson, Hein, Bertolotti and Simen in 1993. For our analysis is important to say that although NOLOT is a non-local stability code, it has four different subsets of equation:

local parallel: all streamwise derivatives of amplitude functions are neglected ($D=0$) and all terms which are related to the nonparallel basic flow are removed from A and B.

nonlocal parallel: only terms related to the nonparallel basic flow are removed from A and B.

local nonparallel: all streamwise derivatives of amplitude functions are neglected ($D=0$) but terms related to the nonparallel basic flow are kept in A and B.

nonlocal nonparallel: the complete set of equations is considered.

In the following section we are going to make a local analysis.

1. Local stability analysis

The term local means that the analysis wherein the mean-flow variation and the geometry variation in the direction of amplification is neglected, and only the variation normal to the wave-rays is considered. In order to consider this case, as we have said before, we must consider $D=0$ in the PSE and all terms which are related to the nonparallel basic flow

are removed from A and B. The results is an equation equal to a Orr-Sommerfeld equation. Hence, the local case is described by a system of ordinary differential equations which in NOLOT are solved as a boundary-value problem. The first case we have studied is the flat plate with $U_e = cost$. We have changed the value of the β maintaining constant the value of frequency of perturbation. Obviously, for $\beta = 0$ we have a two dimensional case. In the graph we have considered the growth-rate and the N-factor in function of s/c . The growth-rate is defined below:

$$(72) \quad \sigma = \frac{1}{h_1}(-\alpha_i + Real[\frac{1}{\xi} \frac{\partial \xi}{\partial y}])$$

where the first term on the right-hand represents the contribution from the exponential part of the disturbance and the second term is the correction due to the changes of the amplitude function. ξ can be taken the maximum of the stream wise or normal velocity component for each fixed x-position. Alternatively, we can consider the kinetic energy E

$$(73) \quad E = \frac{1}{2} \int_0^\infty (|\hat{u}|^2 + |\hat{v}|^2 + |\hat{w}|^2) dy$$

and the (68) becomes

$$(74) \quad \sigma = \frac{1}{h_1}(-\alpha_i + \frac{\partial}{\partial y}(ln\sqrt{E}))$$

Like the Figure E.2 shows, in a 2D case we have most high number of *Nfactor* and this is in agree with the Squire's theorem saying that parallel shear flows first become unstable to two-dimensional wavelike perturbations at a value of the Reynolds number that is smaller than any value for which unstable three-dimensional perturbations exist. For this reason we can study the local stability for 2D flow. At first we have changed the value of frequency for $\beta = 0$ (see Figures E.3, E.4).

We can notice (see Figure E.4) that for lower frequency we have the maximum of *Nfactor* at larger s/c . Now we have made a study on a flat plate

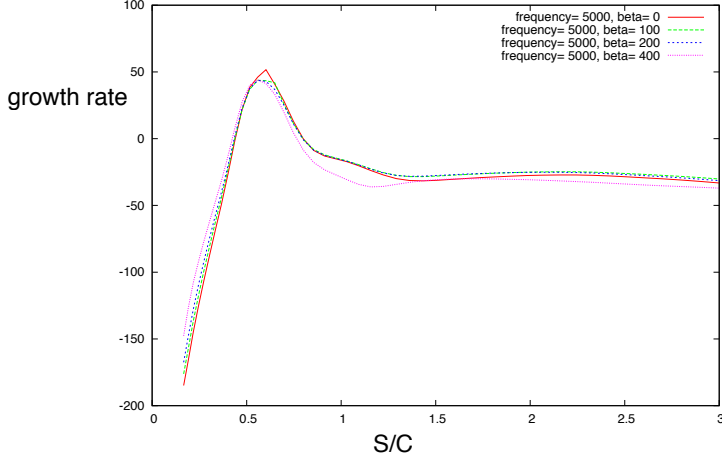


FIGURE E.1. Growth-rate $\sigma = -\alpha_i$ for different value of β at frequency of 5000 Hz

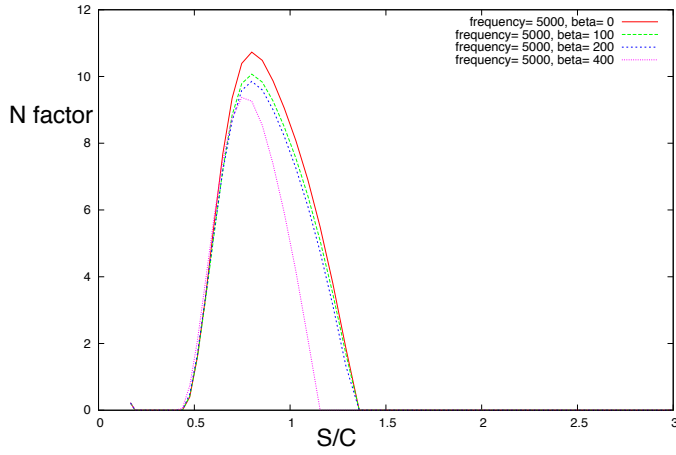


FIGURE E.2. N factor for different value of β at frequency of 5000 Hz. $N = \int_{x_0}^x (-\alpha_i) dx$. We can notice the growth-rate is higher with 2D perturbation than with 3D perturbation. It is agreement with the Squire theorem

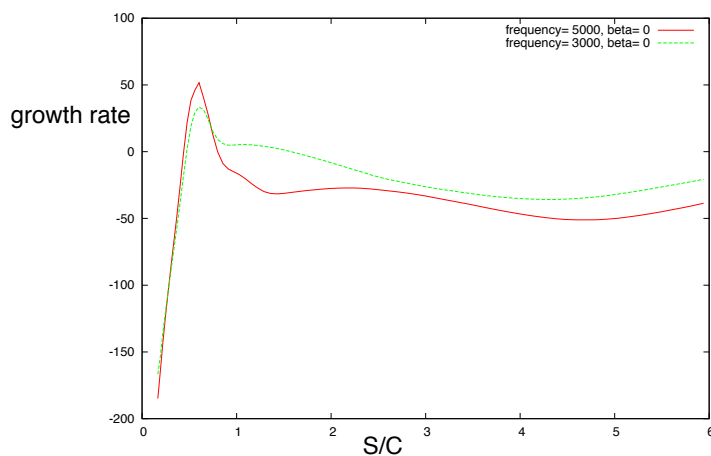


FIGURE E.3. Growth-rate for two-dimensional flow. We can see the different value of σ for different frequency.

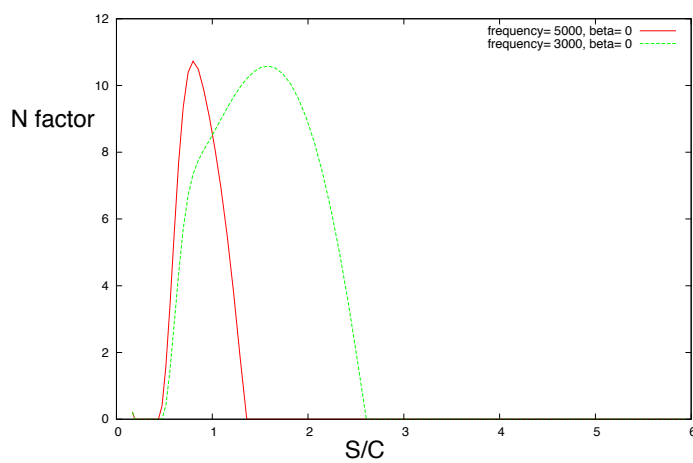


FIGURE E.4. N factor for two-dimensional flow. We have the position of instability nearest the trading edge for lower frequency.

for different value of external velocity. In particular we have used the flow $U_e = x^m$ with three different value of m like we saw in Appendix A. After a first calculation we have seen that $R_e = 1000000$ was too low for the flat plate, so we have increased it to 4000000. (see Figures E.5, E.6, E.7)

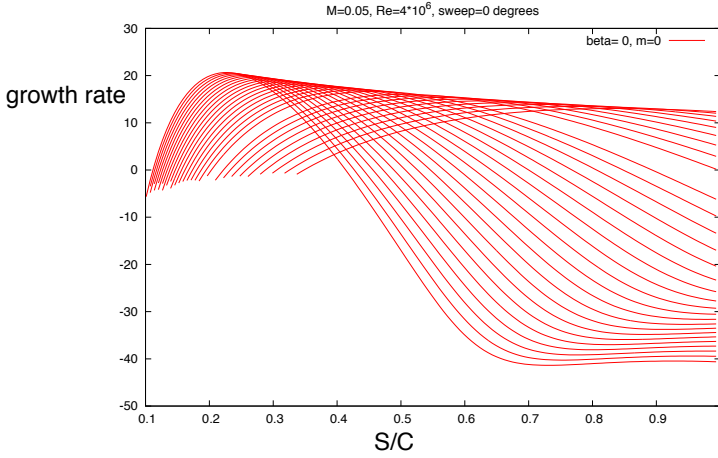


FIGURE E.5. Growth-rate on a flat-plate for $R_e = 4 \times 10^6$; $M = 0.05$; $m = 0$; $\beta = 0$. They can see the dependence of TS waves from the viscosity. Two dimensional, incompressible and steady flow.

The next results are for $m=0.08$ (see Figures E.8, E.9, E.10).

For this case we see that N factor remains very low and this is agree with the fact that $m > 0$ determines a favorable pressure gradient . At least we make the study for $m = -0.03$ (see Figures E.11, E.12, E.13).

To better see the influence of the pressure gradient on the stability of laminar boundary layer, we have plotted the N factor for the three cases in a same Figure E.14.

The Figures we have seen show the development of a particular type of instability that were studied for the first time by Tollmien (1992) and Schlichting (1933) for the Blasius boundary layer. These instability are

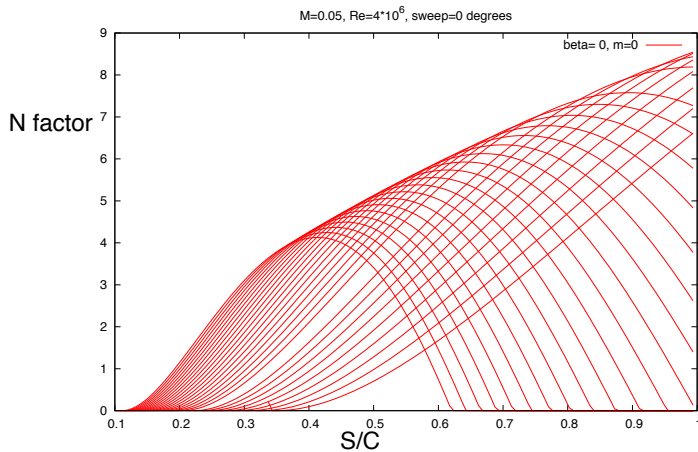


FIGURE E.6. N factor on a flat-plate for $R_e = 4 \times 10^6$; $M = 0.05$; $m = 0$; $\beta = 0$. The figure shows the development of N factor for different frequency. As we will see later we have the maximum value for low frequency.

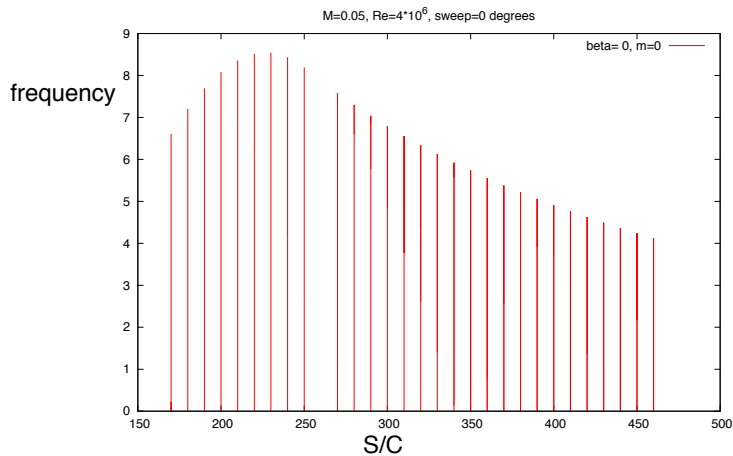


FIGURE E.7. N factor as a function of frequency. $R_e = 4 \times 10^6$; $M = 0.05$; $m = 0$; $\beta = 0$. We have the top of N factor near to 220 Hz.

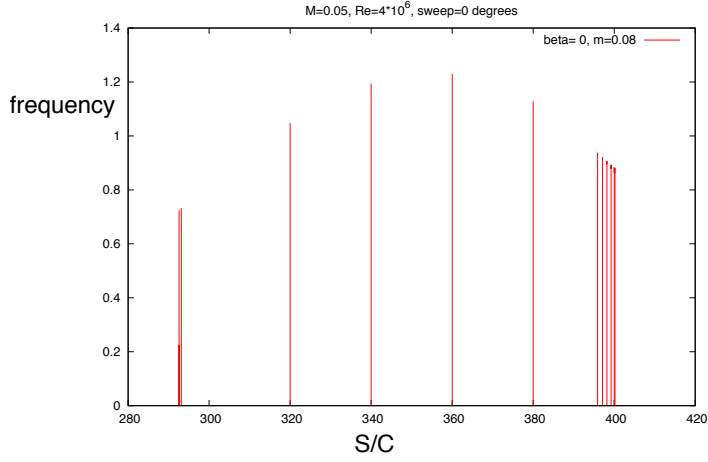


FIGURE E.8. N factor as a function of frequency. Negative pressure gradient. $R_e = 4 \times 10^6$; $M = 0.05$; $m = 0.08$; $\beta = 0$.

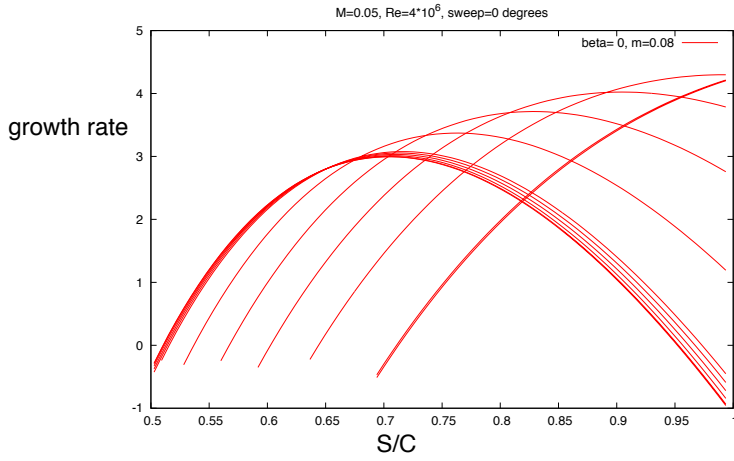


FIGURE E.9. Growth rate of the small disturbances for a accelerate and incompressible flow. $R_e = 4 \times 10^6$; $M = 0.05$; $m = 0.08$; $\beta = 0$.

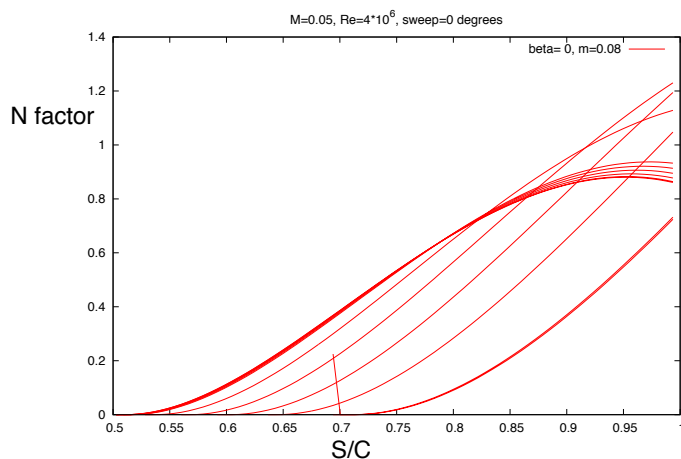


FIGURE E.10. N factor as a function of the dimensionless chord. $R_e = 4 \times 10^6$; $M = 0.05$; $m = 0.08$; $\beta = 0$. Negative pressure gradient and incompressible flow.

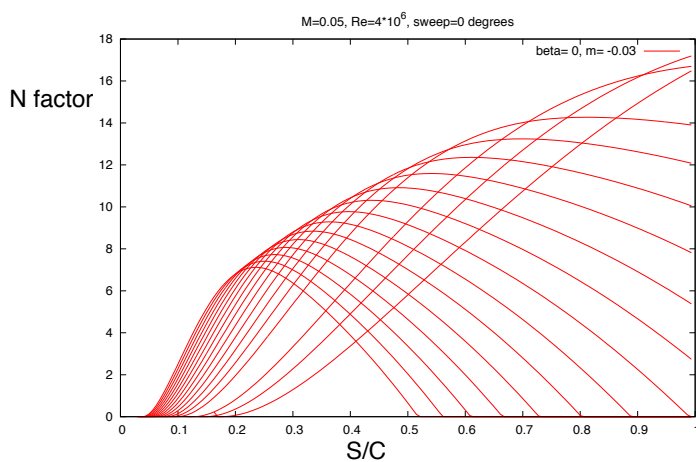


FIGURE E.11. N factor as a function of the dimensionless chord. $R_e = 4 \times 10^6$; $M = 0.05$; $m = -0.03$; $\beta = 0$. Positive pressure gradient.

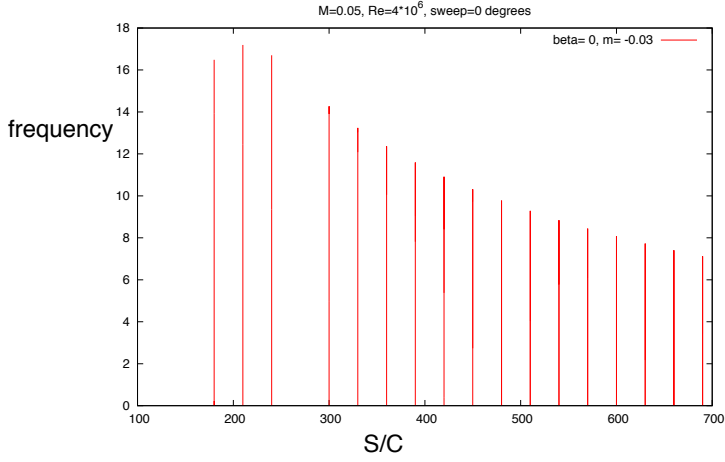


FIGURE E.12. N factor as a function of the frequency for a positive pressure gradient. $R_e = 4 \times 10^6$; $M = 0.05$; $m = -0.03$; $\beta = 0$.

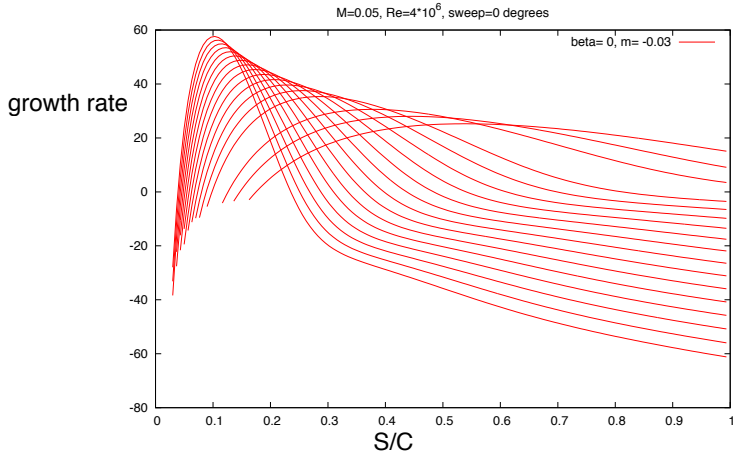


FIGURE E.13. Growth rate of the small disturbance in a decelerate flow. $R_e = 4 \times 10^6$; $M = 0.05$; $m = -0.03$; $\beta = 0$.

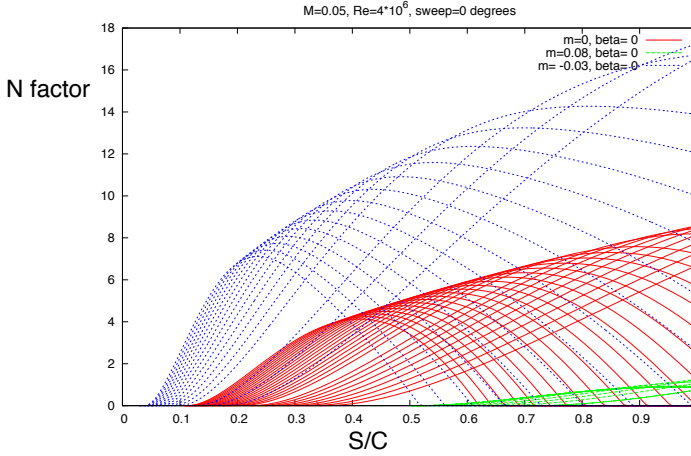


FIGURE E.14. Comparison between N factors for three different external flow. Decelerate flow (blue); Constant flow (red); Accelerate flow (green). $R_e = 4 \times 10^6$; $M = 0.05$; $\beta = 0$. Two dimensional, steady and incompressible flow.

called Tollmien-Schlichting (TS) waves and they represent a viscous instability. We have seen it in the diagram of σ where, after the top, we have a decreasing development for the effect of viscosity. This means they are stable in the inviscid limit. The wave vector and the direction of propagation are closely aligned with the streamline direction. As we will see later, these waves also exist in a swept wing boundary layer but they are not the principal responsible for the instability.

2. Local stability analysis for 2,5 D

Now we consider a boundary layer for a quasi three-dimensional flow in a swept flat plate with infinity length in z-direction. Considering a quasi three-dimensional flow we will have a perturbation with also the wave number β and it will be a more complicated case. At first we see the case with a positive pressure gradient. We have choose a swept flat plate with a sweep = 45, $M = 0.05$ like the two-dimensional case, $R_e = 4 \times 10^6$

and m , the coefficient relatives to acceleration of the flow, is 0.2. For this parameters we have made the study of stability with Nolut. This time we have had the difficult to decide the right combination of α, β and wave angle and it has let the calculation more long than before.

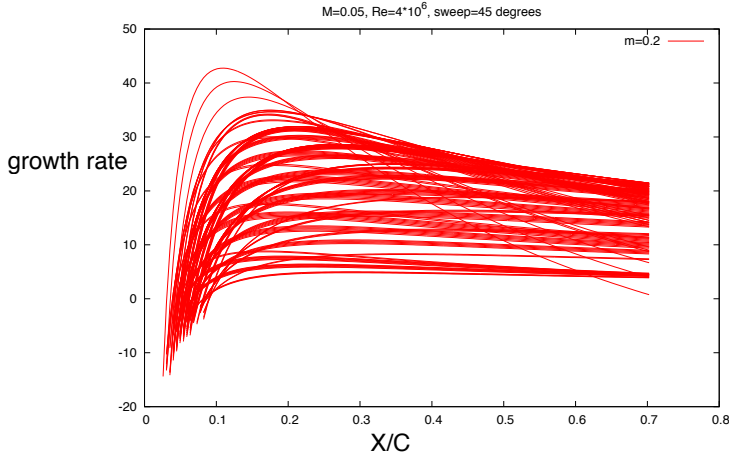


FIGURE E.15. Growth-rate for a swept flat plate. $Sweep = 45$; $M = 0.05$; $Re = 4 \times 10^6$. As the figure shows, only for few frequency we have negative value of σ after the top.

As we can see from the graphic of σ (see Figure E.15), the growth-rate is larger near the leading edge and, almost for all frequency, σ remain always positive. This effect due to the presence of crossflow profile which are inviscid instability. In fact, when the crossflow profile tends to zero in the free-stream, we have an inflection point and agreement with Reyligh (1880), an inflection point is a necessary condition for inviscid instability to arise. This crossflow profile results from the combined effect of pressure gradient and sweep angle which leads to a curved streamline in the outer inviscid flow. From experimental works, their lines of constant phase are approximately parallel with the external streamline and we can see it from the graphic of wave angle (Figure E.17). As it shows, the angle is between

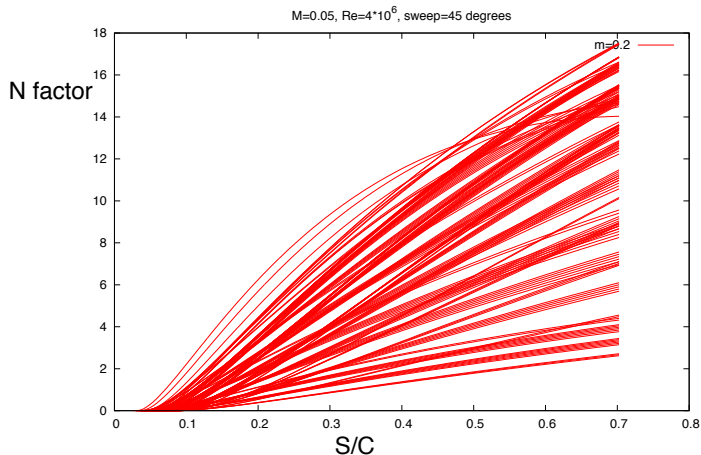


FIGURE E.16. N factor for a swept flat plate. $Sweep = 45$; $M = 0.05$; $Re = 4 \times 10^6$. The development of N factor shows the importance of crossflow for the stability.

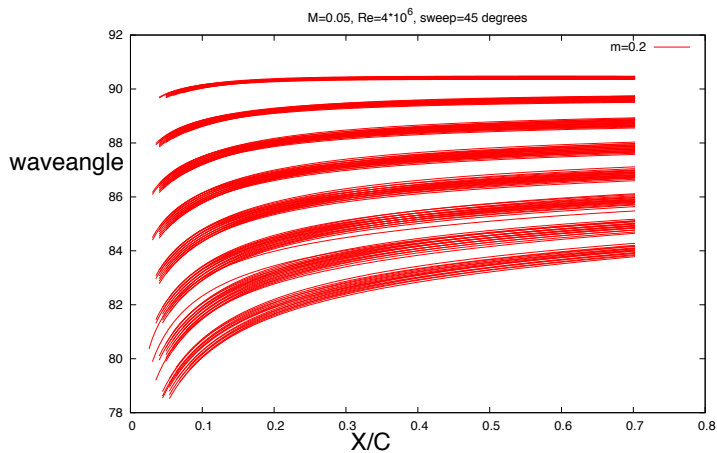


FIGURE E.17. Wave angle for a swept flat plate. $Sweep = 45$; $M = 0.05$; $Re = 4 \times 10^6$. As the figure shows, the lines of constant phase are almost parallel with the external streamline.

80 – 90 degrees.

In the Figure E.18, we also represent the envelope of the maximum of N factor. This is an important curve for the study of shape optimization of profiles.

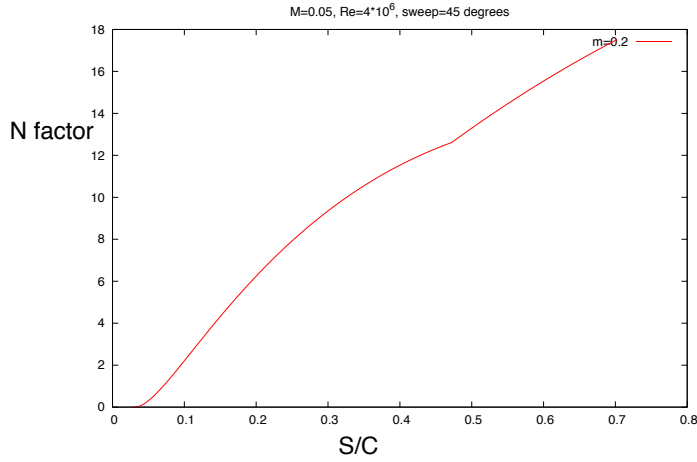


FIGURE E.18. N factor envelope for a swept flat plate. $Sweep = 45$; $M = 0.05$; $Re = 4 \times 10^6$. The red line represents the envelope of N factor of the dominant mode at each position.

Bibliography

- [1] Dr. Hermann Schlichting, Boundary-Layer Theory, McGraw-Hill Book Company, Part C.
- [2] Peter J. Schmid and Dan S. Henningson, Stability and Transition in Shear Flows, Springer, 2001.
- [3] David Templelmann, Receptivity of crossflow-dominated boundary layers, Royal Institute of Technology, Technical Reports, Stockholm December 2011.
- [4] Dr. Hermann Schlichting, Boundary-Layer Theory, McGraw-Hill Book Company, pp 132-133.
- [5] Jan Pralits, Optimal Design of Natural and Hybrid Laminar Flow Control on Wings/Optimal Design for Disturbance control, Royal Institute of Technology, Technical Reports, Stockholm, October 2003.
- [6] Dr. Hermann Schlichting, Boundary-Layer Theory, McGraw-Hill Book Company, Chapter XIV.
- [7] Brenda M. Kulfan, "CST" Universal Parametric Geometry Representation Method, Fourth International Conference on Flow Dynamics, Japan September 26-28, 2007.
- [8] Kathleen T. Alligood and Tim D. Sauer and James A. Yorke, CHAOS: An Introduction to Dynamical Systems, Springer, Chapter 12, 2000.
- [9] ANSYS - User Guide content, FLUENT/User's Guide/Modeling Turbulence/Reynolds Averaged Navier-Stokes (RANS) Turbulence Models.
- [10] Ardeshir Hanifi, Local and Non-local Stability Analysis and Transition Prediction of Compressible Boundary Layer Flows, Royal Institute of Technology, Doctoral Thesis, Stockholm, 1995. Paper 3.
- [11] Yongsheng Lian and Wei Shyy, Laminar-Turbulent Transition of a Low Reynolds Number Rigid or Flexible Airfoil, University of Michigan, equation 17, July 2007.
- [12] www.esteco.com, modeFRONTIER's Guide, DOE - Design Of Experiment.
- [13] www.esteco.com, modeFRONTIER's Guide, Algorithms of Optimization.
- [14] Ansys - User Guide content, FLUENT/User's Guide/Modeling Basic Fluid Flow/Inviscid Flow.

- [15] Marco Oswald, Best Practice Guidelines for Aerospace Simulations with FLUENT 6.3/Impact of Mesh Quality (1), ANSYS, 2006.
- [16] ANSYS - User Guide content, FLUENT/User's Guide/Modeling Turbulence/Reynolds Averaged Navier-Stokes (RANS) Turbulence Models/Spalart-Allmaras One-Equation Model.
- [17] www.esteco.com, modeFRONTIER's Guide, Algorithms of Optimization/MOGA II.
- [18] RH Barnard and DR Philpott, Aircraft Flight, Pearson Education Limited, The Boundary Layer and its Control, fourth edition 2010.
- [19] ANSYS - User Guide content, FLUENT/User's Guide/Modeling Turbulence.
- [20] RH Barnard and DR Philpott, Aircraft Flight, Pearson Education Limited, Lift, fourth edition 2010.
- [21] European Aviation Safety Agency, Certification Specifications for Normal, Utility, Aerobatic, and Commuter Category Aeroplanes CS-23, Take-off speeds.
- [22] RH Barnard and DR Philpott, Aircraft Flight, Pearson Education Limited, Wings/Trailing vortex formation, fourth edition 2010.
- [23] David Templemann, Receptivity of crossflow-dominated boundary layers/Transition in three-dimensional boundary layer, Royal Institute of Technology, Technical Reports, Stockholm December 2011.